DISSERTATION | DOCTORAL THESIS

Titel | Title

From the Weak to Ultrastrong - Coupling Regimes in Levitated Cavity Optomechanics

verfasst von | submitted by

Kahan Mcaffer Dare

angestrebter akademischer Grad | in partial fulfilment of the requirements for the degree of

Doktor der Naturwissenschaften (Dr.rer.nat.)

Wien | Vienna, 2024

Studienkennzahl lt. Studienblatt | Degree programme code as it appears on the student record sheet:	UA 796 605 411
Dissertationsgebiet lt. Studienblatt | Field of study as it appears on the student record sheet:	Physik
Betreut von | Supervisor:	Univ.-Prof. Dr. Markus Aspelmeyer

Abstract

Levitated oscillators provide a unique opportunity for quantum sensing due to their potential for high quality factors and macroscopic size. However, preparation of a pure quantum state of motion has been obstructed by technical challenges with active cooling schemes and laser noise with passive cavity schemes. Recently, the field of levitated cavity optomechanics has seen a renaissance due to the adaptation of coherent scattering from atomic physics. This departure from the traditional paradigm of dispersive coupling promises to bypass the technological barriers and allow for ground state cooling. Moreover, the obtainable coupling rates are expected to be an order of magnitude larger than in the dispersive case.

In a first experiment, a levitated dielectric nanoparticle is weakly coupled to the optical cavity via coherent scattering and cooled to the ground state of its motion. This is the first demonstration of such a macroscopic solid cooled to its ground state without the use of cryogenics. In a second experiment, the coupling is increased to the strong coupling regime whereby the modes of the optical resonator and mechanical oscillator are hybridized. The resulting normal mode splitting is observed and used to characterize the coupling rate. In a third experiment, the coupling is increased further such that system is situated deep in the ultrastrong coupling regime where the system is dynamically unstable and exhibits an avoided crossing. This is the first solid-state optomechanical device to operate in the ultrastrong coupling regime. These three results lay a foundation for full quantum control of massive mechanical oscillators.

Zusammenfassung

Levitierte Oszillatoren bieten aufgrund ihres Potenzials für hohe Qualitätsfaktoren und ihrer makroskopischen Größe eine einzigartige Gelegenheit für die Quantensensorik. Die Herstellung eines reinen Quantenbewegungszustands wurde jedoch durch technische Herausforderungen bei aktiven Kühlsystemen und Laserrauschen bei passiven Hohlraumsystemen behindert. In jüngster Zeit hat das Gebiet der Optomechanik mit schwebenden Hohlräumen durch die Adaption der kohärenten Streuung aus der Atomphysik eine Renaissance erlebt. Diese Abkehr vom traditionellen Paradigma der dispersiven Kopplung verspricht, die technologischen Barrieren zu umgehen und eine Kühlung im Grundzustand zu ermöglichen. Außerdem dürften die erzielbaren Kopplungsraten um eine Größenordnung höher sein als im dispersiven Fall.

In einem ersten Experiment wird ein schwebendes dielektrisches Nanopartikel über kohärente Streuung schwach an den optischen Hohlraum gekoppelt und auf den Grundzustand seiner Bewegung abgekühlt. Dies ist die erste Demonstration eines solchen makroskopischen Festkörpers, der ohne den Einsatz von Kryotechnik auf seinen Grundzustand abgekühlt wird. In einem zweiten Experiment wird die Kopplung bis zur starken Kopplung erhöht, wodurch die Moden des optischen Resonators und des mechanischen Oszillators hybridisiert werden. Die daraus resultierende Normalmodenaufspaltung wird beobachtet und zur Charakterisierung der Kopplungsrate verwendet. In einem dritten Experiment wird die Kopplung weiter erhöht, so dass sich das System tief im Bereich der ultrastarken Kopplung befindet, wo das System dynamisch instabil ist und einen vermiedenen Übergang aufweist. Dies ist die erste optomechanische Festkörpervorrichtung, die im Bereich der ultrastarken Kopplung arbeitet. Diese drei Ergebnisse bilden die Grundlage für die vollständige Quantenkontrolle von massiven mechanischen Oszillatoren.

Preface

This dissertation is written in the style of an AMO dissertation in that it progresses from theory to the experimental apparatus to the results. This is because, up until the third year of PhD I worked in ultracold atomic gases. At this point, a catastrophic failure crippled our experiment. During the rebuild I became connected with Prof. Aspelmeyer and we continued to work together after the ultracold atomic gas experiment was rebuilt. While I transitioned to optomechanics as my main field of research, I have always retained the identity of an AMO physicist and this shows in my work.

As a consequence of this and my rapid induction to a new field, this work is written from the perspective of an outsider. The theory may be overly detailed at certain points but this reflects my journey through the material. I hope this proves useful for future members of our community.

Acknowledgments

These acknowledgements come in two parts for my Zeilinger and Aspelmeyer days. Flying out to Vienna, as what I now feel to be a kid, I was won over by Michi and Mateusz' enthusiasm and bright attitude about the experiment and, even more importantly, life. I am grateful for the years of tutelage and friendship Michi gave me. Throughout this, Anton has been an inspiration and someone I respect immensely. Certainly a scientific force to be reckoned with, Anton has formed my perspective on science and research in general. His ability to cut through to the heart of a problem is something I have aspired to over my entire PhD and I hope I can approach his level someday.

Without Markus' crazy zeal, I doubt I would have made it through a change of fields in as good a shape as I did. Being swept up in his whirlwind of energy and scientific fervour, I was given every opportunity to excel. Thanks to the whole group, I think I was able to capitalize on some of them. Without Uros taking me under his wing, I wouldn't be where I am now. Not to mention being a fellow dad surviving the early years of our kids together. Mel made the long nights of ground state measurements bearable with his mellow and easygoing attitude. If I were stuck on a desert island with only one person to do long frustrating measurements with, he would be the one I'd choose, no doubt. As our cavity team grew, so too did my great fortune at being able to work with bright minds like Aisling, Anton, Ayub, Janneck, Livia and of course Yuriy (Iurie, Lurie, Dragomir, Olga? I never know...). The future of the levitation is extremely bright. All of these people of course participated in my education in the way of foosball. While I may not have made the transition from weak to ultrastrong, I hope I at least made it to decent.

Of course as a kid a long way away from home, I couldn't have gotten through everything without my 'genius' brothers Jarda and Krishna. Bouldering and building, these two have become two of my closest friends with their willingness to pursue stupid ideas together.

I don't think Zoya needs me to write down how much she has carried me through this experience. Truly the best partner I could ever imagine. Thankfully we were blessed with the greatest little man in Elio. He surely could have made the last couple of years of my PhD significantly harder if he wanted but alas he takes after his mother and is truly wonderful.

Table of Contents

Chapter 1

Introduction

Purcell discovered that the engineering of the environment can modify the spontaneous emission probabilities of a quantum system [1]. This lay the foundation for what we now call cavity quantum electrodynamics (cavity QED). Researchers have since developed a variety of experimental platforms seeking to increase the coupling between light and matter [2–7]. This has lead to the observation phenomena like vacuum Rabi oscillations [8], single-photon sources [9], and entanglement [10–15].

Recently, this has been introduced to the field of levitated cavity optomechanics [16, 17]. In this case, a dielectric nanoparticle acts as the emitter inside of an optical cavity, coupling its motion to the cavity mode. This interaction was adapted from atomic physics [18]. Prior to this the field of cavity optomechanics was restricted to dispersive coupling schemes where the motion of the oscillator was coupled to the cavity mode through the modification of the round-trip phase. This new coupling benefits from the Purcell enhancement of the scattering probability, allowing for new opportunities to engineer the light-matter coupling. Since its inception, levitated cavity optomechanics has been motivated by its application to quantum sensing [19, 20] due to its promise of high quality factors in room-temperature environments[1]. In addition, contemporary solid state devices used in levitated cavity optomechanics consist of approximately 10^9 atoms existing in a joint motional mode, allowing for a unique opportunity for state engineering through the flexibility of optical technologies. It is therefore critical that the engineering of this interaction be studied.

This dissertation will cover both the theoretical and experimental in-

---

[1] It has been realized by now that photon recoil prevents infinite Q-factors in conventional tweezer traps.[17]

vestigation into engineering the light-matter coupling between a levitated mechanical oscillator and an optical resonator. We will demonstrate both the limits this coupling can reach as well as how it may be employed for quantum control of the system.

1.1 Overview of Thesis

This dissertation is split into three main parts: the theoretical background for the optomechanical behaviour, the overview of the experimental apparatus and detection techniques and the resulting measurements. In Chapters 2, 3, and 4 we discuss the theory of levitated optomechanics, optical cavities and then levitated cavity optomechanics. This structure will allow us to piecewise construct a full model of the system. Chapter 5 will elaborate on all of the experimental details. In chapter 6 we will discuss the operation of our system in the weak coupling regime with a particular focus on its application to ground state cooling of the mechanical oscillator. Lastly, we will extend this to the strong and ultrastrong coupling regimes in Chapter 7 and verify our theoretical model with experimental results.

1.1.1 The Theory of Levitated Cavity Optomechanics

Chapter 2: We disassmble our apparatus into the mechanical and optical subsystems. In Chapter 2 we discuss the mechanical subsystem consisting of a dielectric nanosphere levitated by an optical tweezer through the dipole interaction. We write down the full Hamiltonian for this case including dissipation through the use of the Caldeira-Leggett model of an oscillator coupled to its environment. We compute the dynamics of this subsystem and conclude by computing the associated heating and damping rates for relevant couplings. Chapter 3: In this chapter we consider the optical subsystem consisting of a double-sided optical cavity which is coupled to the environment through the imperfect cavity mirrors. We again compute the dynamics of the system in the quantum regime. Chapter 4: We start by linearly coupling the optical and mechanical subsystems and computing the full dynamics of the system. We outline the implications of the coupling strength on the steady-state behaviour of the system. We then outline physical processes by which this coupling can be realized, namely a dispersive interaction or a coherent-scattering interaction. We finish with the heating and damping rates associated with this coupling.

1.1.2 The Experimental Apparatus

Chapter 5: We detail the experimental apparatus used in this dissertation. This includes the optical tweezer, optical cavity, detection and vacuum chamber.

1.1.3 Coupling Regimes

Chapter 6: Here we discuss the weak coupling regime as realized in our system. We proceed to show how this can be leveraged to do cavity cooling and prepare the mechanical oscillator in its motional ground state. Chapter 7: We demonstrate how modifying some of the system parameters allows access to the ultrastrong coupling regime. We report on measurements demonstrating the hybridization of the optical and mechanical modes as evidence for strong coupling and, using the retrieved coupling rates, we characterize the system both in the strong and ultrastrong regimes. We then provide an outlook on how this can be extended in future work.

Part I

The Theory of Levitated Cavity Optomechanics

Chapter 2

Levitated Optomechanics

This chapter will serve as the foundation for our understanding of optomechanics in our system. The system we will consider here will consist of 3 main elements that will be elaborated upon in Chapter 5; the dielectric particle, the optical tweezer and the vacuum chamber. Our physical picture can be seen in Figure 2.1 in which the dielectric particle is levitated in the optical tweezer inside of a vacuum chamber. We will be mostly concerned with the mechanics of the dielectric particle's center of mass motion as it interacts with the tweezer and its surrounding vacuum environment.

In doing so, we will build up a qualitative and quantitative understanding of the optomechanics in this system which will then be built upon in Chapter 4 when we complete this setup by introducing an optical cavity. This ordering serves to highlight both the historical development but also ascends a hierarchy of complexity.

2.1 Optical Dipole Traps

With the introduction of optical levitation by Arthur Ashkin and his colleagues [21], optical trapping of particles has become a standard technique in fields ranging from physics[22] and chemistry[23] to biology [24]. This revolutionary use of light-matter interaction is critical to our experiment as it acts as the basic potential for our optomechanical oscillator. This has the added benefit of decoupling our system from the environment, eliminating the need for cryogenics that significantly complicated previous optomechanical systems [25].

To understand this technique, we first consider a dielectric placed in an electric field $\vec{E}$. The electric field induces a polarization in the material

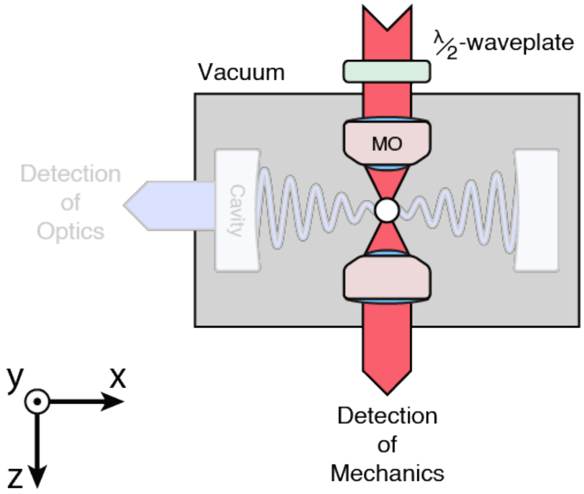

Figure 2.1: **A sketch of a levitated optomechanical system.** A tweezer beam (red) is focused by a microscope objective (MO) and at the focus a dielectric object (white circle) is trapped and acts as a mechanical oscillator. The tweezer light can subsequently be used to detect the motion of the oscillator. Some sort of polarization control (green) can be used to modify the orientation of the trapping potential. In this dissertation, the dielectric is trapped inside of a vacuum chamber to isolate the mechanical oscillator from the environment.

according to

$$\vec{P}(\vec{x}) = \epsilon_0 \chi \vec{E}(\vec{x}) \tag{2.1}$$

where ϵ_0 is the permittivity of free space and $\chi = 3\mathrm{Re}\left\{\frac{\epsilon_s - 1}{\epsilon_s + 2}\right\}$ is the electric susceptibility of the dielectric with ϵ_s denoting the relative electric permittivity of the dielectric. This induced polarization density can then interact with the electric field, giving rise to an optical potential

$$U(\vec{x}) = -\frac{1}{2}\int_V \vec{P}(\vec{x})\vec{E}(\vec{x})d^3x, \tag{2.2}$$

$$= -\frac{1}{2}\epsilon_0 \chi \int_V \left|\vec{E}(\vec{x})\right|^2 d^3x. \tag{2.3}$$

where we are integrating over the volume of the dielectric. If we now consider that this electric field is due to some optical field, and that the dielectric is much smaller than the wavelength of that light, we can approximate the electric field as constant over the volume of the dielectric, in which case we can simplify the potential to

$$U(\vec{x}) = -\frac{1}{2}\alpha_{\mathrm{ind}} \left|\vec{E}(\vec{x})\right|^2 = -\frac{\alpha_{\mathrm{ind}}}{nc\epsilon_0} I(\vec{x}) \tag{2.4}$$

where $\alpha_{\mathrm{ind}} = 3\epsilon_0 \chi V$ is the polarizability of the dielectric and $I(\vec{x})$ is the intensity of the light. We can immediately see then that the spatial profile of the light field creates a conservative force $\vec{F}(\vec{x}) = -\nabla U(\vec{x}) \propto \nabla I(\vec{x})$. For a focused laser beam, this gradient force becomes a potential well which, depending on the power, can be deep enough to trap dielectric objects. This is the mechanism behind an optical dipole trap or so-called optical tweezer.

2.1.1 Harmonic Trapping Potential

A useful way to frame this light-matter interaction is as a harmonic potential, in which case we would approximate Equation 2.4 with a quadratic potential of the form

$$U(\vec{x}) \approx \frac{1}{2}m\Omega_x^2 x^2 + \frac{1}{2}m\Omega_y^2 y^2 + \frac{1}{2}m\Omega_z^2 z^2 \tag{2.5}$$

where Ω_i are called the trap frequencies. In Appendix B, we show that, for a gaussian laser beam propagating along the z-direction, one can show that this is, in many applications, a good approximation and we can identify the trap frequencies as

$$\Omega_x = \Omega_y = \sqrt{\frac{\alpha_{\text{ind}} P_0}{m\pi n c \epsilon_0} \frac{2}{W_0^2}}, \tag{2.6}$$

$$\Omega_z = \frac{1}{\sqrt{2}} \frac{W_0}{z_R} \Omega_{x,y}, \tag{2.7}$$

where the beam is propagating along the $z-$direction, $P_0 = \frac{1}{2}\pi I_0 W_0^2$ is the laser power, W_0 is the beam waist (radius) and $z_R = \pi W_0^2/\lambda$ is the Rayleigh length of the beam. We denote $\Omega_{x,y}$ and Ω_z as the radial and axial frequencies respectively.

Optical dipole traps can incorporate multiple laser beams to increase the depth of the trapping potential or change the trapping frequencies. In atomic physics for instance, a common technique is to create a so-called crossed optical dipole trap consisting of two weakly focused laser beams ($W_0 << z_R$) intersecting at some angle. This cross can greatly increase the axial confinement along one laser beam that would've otherwise been set by the Rayleigh length of the beam.

2.1.2 Optical Tweezers

An optical tweezer takes the extreme case of tightly focusing a laser beam. This serves to increase the axial confinement to be more on par with the radial confinement. When focusing this tightly, the beam is no longer a simple gaussian beam and instead has some asymmetry in the radial direction arising from the polarization. A detailed discussion can be found in

Appendix B in which we find the trap frequencies are modified to

$$\Omega_x = \sqrt{\frac{\alpha_{\text{ind}} P_0}{m\pi n c\epsilon_0}(|e_y|^2 - |e_x|^2) i_0 i_6 - i_0 i_1 - 2|e_x|^2 i_4^2)}\frac{k^2}{f_0 \text{NA}}, \tag{2.8}$$

$$\Omega_y = \sqrt{\frac{\alpha_{\text{ind}} P_0}{m\pi n c\epsilon_0}(|e_x|^2 - |e_y|^2) i_0 i_6 - i_0 i_1 - 2|e_y|^2 i_4^2)}\frac{k^2}{f_0 \text{NA}}, \tag{2.9}$$

$$\Omega_z = \sqrt{\frac{\alpha_{\text{ind}} P_0}{m\pi n c\epsilon_0}\frac{1}{2}(-2 i_0 i_3 - |i_2|^2)}\frac{k^2}{f_0 \text{NA}} \tag{2.10}$$

where i_j are numerical factors, $e_{x,y}$ are the polarization components of the electric field, f_0 is the filling factor of the microscope object with numerical aperture NA. We can see the symmetry of Ω_x and Ω_y is broken depending on the polarization of the light which is critical behaviour not captured by the simple gaussian model.

2.1.3 Radiation Pressure

One effect we have neglected in this is the radiation pressure the dielectric experiences due to the directionality of the tweezer laser. This displaces the particle to a region in which the intensity is lower, decreasing the stability of the trap [26, 27].

If we limit our interest to spherical dielectrics, we can take advantage of the well known Mie solution to Maxwell's equations to model the interplay between the trapping and radiation pressure forces for arbitrary sized particles. For nanoparticles of radius r, we expect the trap frequency to scale as $r^{3/2}$ while the radiation pressure scales as r^2 suggesting as the particle size increases the radiation pressure should start to dominate. This is in agreement with the full model of the trap frequency shown in Figure 2.2. At a certain size it becomes impossible to trap a nanoparticle with a single beam trap. This decrease in trap frequency as size increases is an important observable effect that we will return to in Chapter 7. One could counteract this effect by employing more advanced experimental techniques such as counterpropagating traps.

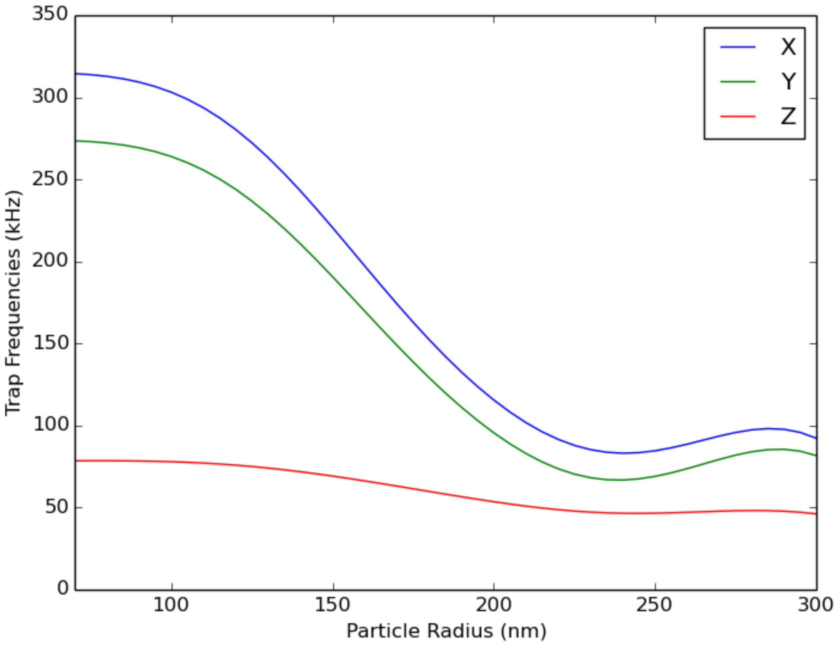

Figure 2.2: **Trap frequencies for varying sized particles according to the full Mie solution.** The model uses parameters from the apparatus given in Table 5.2

2.1.4 Absorption

A consequence of using an attractive laser potential (as opposed to a blue detuned dipole trap in atomic systems [28–33, 22]) is the absorption of photons by the dielectric material. Since the particle naturally occupies the region of largest intensity, it is often times subject to a large amount of impinging laser power. Despite small absorption cross-sections, internal temperatures exceeding 1000K [34] are routinely reached. While still stable at these temperatures, this can pose a problem to quantum experiments as decoherence via blackbody emission can bring the coherence time prohibitively low[35].

As will be discussed later, the presence of air or other gas in the vacuum chamber can help mitigate the temperature increase by providing an alternative cooling channel but at high-vacuum, where one could measure quantum phenomena, this is not the case. Taking the full model provided in [34], we can map out the steady-state internal temperature of the particle as a function of background gas pressure and environment temperature for standard tweezer parameters mentioned in Chapter 5. This is shown in Figure 2.3 and it is clear that for all but cryogenic environments or high gas pressures, the internal temperature of the dielectric is exceedingly high. One can specifically choose dielectric materials and laser wavelengths to decrease the absorption cross-section at the outset of an experiment.

For the experiments discussed in this dissertation, this has not been the limiting factor but it is mentioned as it will quickly play a role as the next steps are taken.

2.1.5 Anhormonicity

We have assumed the particle experiences a predominantly harmonic potential which is increasingly the case as we cool the center-of-mass motion. However, at higher motional amplitudes, the particle can explore more of the potential in which case the harmonic approximation breaks down [36]. This can be the case for higher motional temperatures or for squeezed states as will be discussed in more detail in Chapter 7.

In the experiments in this dissertation, we are mostly focused on the low temperature regime where our approximation holds but it is worth noting that at high vacuum the particle can experience the full potential.

2.1.6 Beyond TEM00

Another strength of optical trapping is the ability to rapidly transform the potential in-situ with the use of devices like spatial light modulators (SLMs) or acousto-optic-modulators (AOMs). In this way, arbitrary potentials can be realized and manipulated, an opportunity that would be impossible in tethered mechanical oscillators like membranes. These methods have given rise to a wealth of interesting techniques [33, 37–40] and at its simplest this allows for free-fall experiments where the optical trap is switched off for sometime to allow for wavepacket expansion.

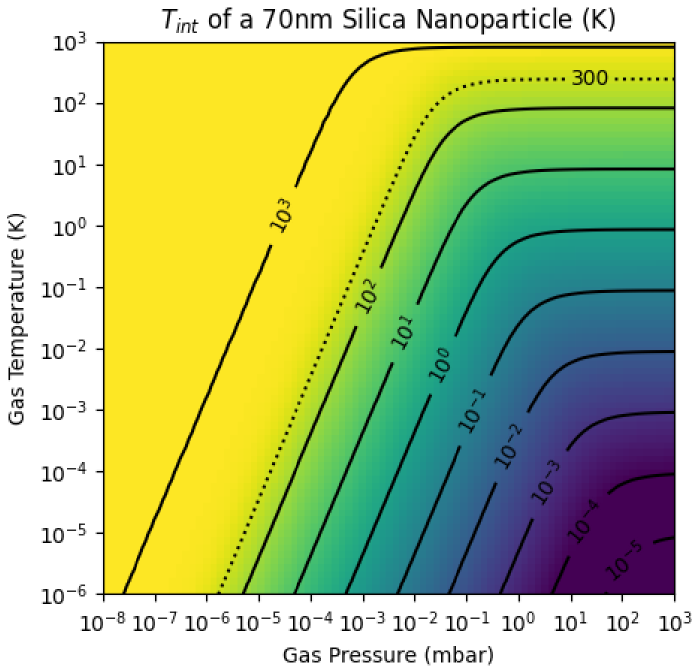

Figure 2.3: **Equilibrium internal temperature of a 70nm silica nanosphere subjected to standard trap conditions detailed in Chapter 5.** For low background gas pressures necessary for quantum experiments, black body radiation is the dominant mechanism for releasing absorbed energy by the particle since there are nearly no gas collisions to take away energy. Even cryogenic gas temperatures alone are insufficient to significantly reduce the internal temperature of the nanoparticle.

2.2 Optomechanics

As we have already seen, the motion of our levitated particle is well described by a harmonic oscillator. This fortuitous behaviour can be analytically modelled for a number of relevant cases. We will hereby set out to model the system to extract various measurable properties. It is instructive to first examine the classical case before transitioning to a quantum mechanical picture.

2.2.1 The Thermal Mechanical Oscillator in Classical Mechanics

A homogeneous, linear equation of motion for a harmonic oscillator in 1D can be written as

$$\ddot{x}(t) + \gamma\dot{x}(t) + \Omega_x^2 x(t) = 0 \tag{2.11}$$

where γ is a damping term, Ω_x is the frequency of the oscillator and m the mass. Figure 2.4 shows the solution to this homogeneous equation $x(t)$ which can be written as

$$x(t) = e^{-\frac{1}{2}\frac{\Omega_0 t}{Q}} \begin{cases} x_0 \cos\left(\sqrt{1 - \frac{1}{(2Q)^2}}\Omega_0 t\right) + \frac{2Q\frac{\dot{x}_0}{\Omega_0} + x_0}{\sqrt{(2Q)^2 - 1}} \sin\left(\sqrt{1 - \frac{1}{(2Q)^2}}\Omega_0 t\right) & , Q > \frac{1}{2}, \text{ underdamped} \\ x_0 + \left(\dot{x}_0 + \frac{1}{2Q}\Omega_0 x_0\right) t & , Q = \frac{1}{2}, \text{ critically damped} \\ x_0 \cosh\left(\sqrt{\frac{1}{(2Q)^2} - 1}\Omega_0 t\right) + \frac{2Q\frac{\dot{x}_0}{\Omega_0} + x_0}{\sqrt{1 - (2Q)^2}} \sinh\left(\sqrt{\frac{1}{(2Q)^2} - 1}\Omega_0 t\right) & , Q < \frac{1}{2}, \text{ overdamped} \end{cases} \tag{2.12}$$

where $Q = \Omega_x/\gamma$ is called the mechanical quality factor and quantifies how many oscillations occur before the energy decays by a factor of 2. Higher Q means that the oscillator has a longer coherence time. This simple case already gives us some intuition for mechanical oscillators and why γ and Ω_x are called as such. We can expand on this simple homogeneous model by adding some arbitrary forces $F_i(t)$ such that our equation of motion becomes

$$\ddot{x}(t) + \gamma\dot{x}(t) + \Omega_x^2 x(t) = \frac{1}{m}\sum_i F_i(t). \tag{2.13}$$

We can solve this second order ordinary differential equation by working in Fourier space in which case we can compactly write it as

$$\tilde{x}(\omega) = \frac{\chi_m(\omega)}{m}\sum_i \tilde{F}_i(\omega). \tag{2.14}$$

where we introduced the mechanical susceptibility

$$\chi_m(\omega) = \frac{1}{\Omega_x^2 - \omega^2 - i\gamma\omega}. \tag{2.15}$$

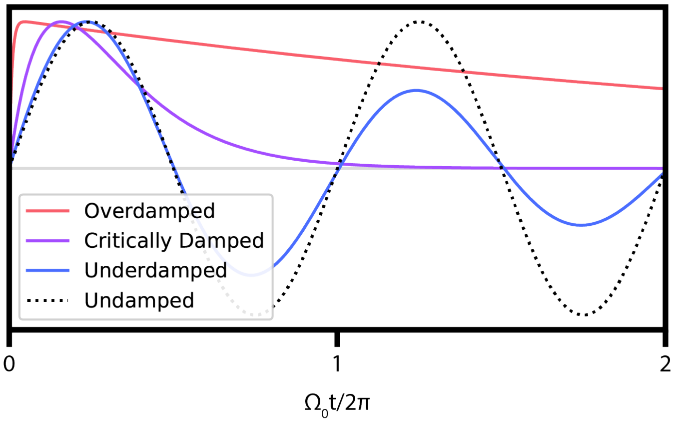

Figure 2.4: **Example solutions $x(t)$ to Equation 2.11 for varying values of the quality factor Q.** We can immediately see that for coherent oscillations to persist, we want to operate well into the underdamped regime where $Q > \frac{1}{2}$ and the solution approaches undamped oscillations.

We are oftentimes interested in the spectral makeup of the motion of the harmonic oscillator. To quantify this, we use the displacement power spectral density (PSD)

$$S_{xx}(\omega) = \lim_{\tau\to\infty} \frac{1}{\tau} \left\langle \left| \int_{-\tau/2}^{\tau/2} x(t) e^{i\omega t} dt \right|^2 \right\rangle. \tag{2.16}$$

A relevant situation is to consider the applied force to be white noise $N_i(t)$. In our system that could be random collisions due to gas molecules which perturb the motion of the particle. In this case we know that

$$\langle N_i(t) N_j(t') \rangle = S_{N_i} \delta_{ij} \delta(t - t') \tag{2.17}$$

where S_{N_i} is the Noise PSD. We can then show that the displacement PSD simplifies to

$$S_{xx} = \frac{|\chi_m(\omega)|^2}{m^2} \sum_i S_{N_i}. \tag{2.18}$$

We can then consider the total power in the spectrum due to these noise terms. In this case we can relate the total power to a temperature of the

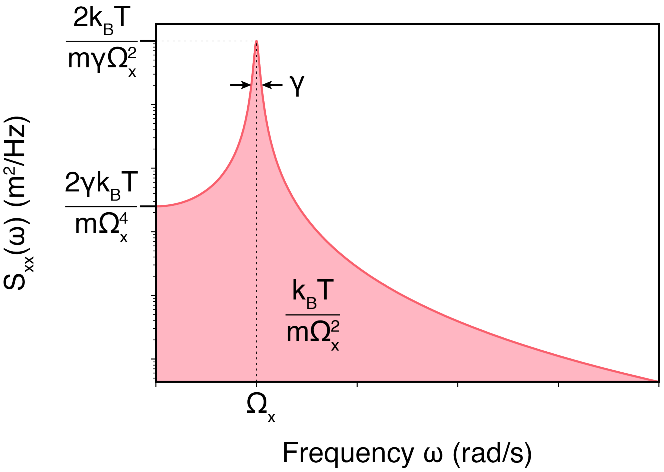

Figure 2.5: **The displacement power spectral density from Equation 2.18.** The curve takes the form of a Breit-Wigner distribution.

motion due to the noise as

$$\int_{-\infty}^{\infty} S_{xx}(\omega)d\omega = \frac{\sum_i S_{N_i}}{m^2}\frac{\pi}{\gamma\Omega_x^2} = 2\pi\frac{k_BT}{m\Omega_x^2}. \tag{2.19}$$

In other words

$$\sum_i S_{N_i} = 2\gamma m k_B T \tag{2.20}$$

which makes clear the connection between the driving strength of the white noise and the damping as follows from the Fluctuation Dissipation theorem.

With this we can model the shape of the PSD for our typical regimes which is shown in Figure 2.5. In the experiment, we can measure the position of the oscillator as a function of time and use that to compute the PSD and retrieve the damping rate instead of calculating it from first principles.

2.2.2 The Thermal Mechanical Oscillator in Quantum Mechanics

The Langevin equations we built previously were done without respecting the commutation relation between x and p. To create a quantum model, we will take the Caldeira-Leggett model of dissipation [41]. This model describes the environment as a bath composed of an infinite number of harmonic oscillators. We can then write our Hamiltonian as

$$\hat{H}_{\text{mech}} = \frac{\hat{p}^2}{2m} + \frac{1}{2}m\Omega_x^2\hat{x}^2 + \sum_i \frac{\hat{p}_i^2}{2m_i} + \sum_i \frac{1}{2}\frac{C_i^2}{m_i\Omega_i^2}\left(\hat{x} - \frac{m_i\Omega_i^2}{C_i}\hat{x}_i\right)^2 \tag{2.21}$$

where $\hat{x}_i$, $\hat{p}_i$, C_i, m_i, and Ω_i, are the position, momenta, coupling constants, masses and oscillator frequencies of the bath operators. We can then derive the equations of motion for our operators

$$\frac{d\hat{x}}{dt} = \frac{\hat{p}}{m}, \tag{2.22}$$

$$\frac{d\hat{p}}{dt} = -m\Omega_x^2\hat{x} - \sum_i \frac{C_i^2}{m_i\Omega_i^2}\left(\hat{x} - \frac{m_i\Omega_i^2}{C_i}\hat{x}_i\right), \tag{2.23}$$

$$\frac{d\hat{x}_i}{dt} = \frac{\hat{p}_i}{m_i}, \tag{2.24}$$

$$\frac{d\hat{p}_i}{dt} = C_i\left(\hat{x} - \frac{m_i\Omega_i^2}{C_i}\hat{x}_i\right). \tag{2.25}$$

We can put these together to get

$$0 = m\ddot{\hat{x}} + m\Omega_x^2\hat{x} + \sum_i \frac{C_i^2}{m_i\Omega_i^2}\hat{x} - C_i\hat{x}_i, \tag{2.26}$$

$$0 = m_i\ddot{\hat{x}}_i + m_i\Omega_i^2\hat{x}_i - C_i\hat{x}. \tag{2.27}$$

We can solve Equation 2.27 to get

$$\hat{x}_i(t) = \hat{x}_i^{(0)}(t) + \frac{C_i}{m_i\Omega_i^2}\left[\hat{x}(t) - \frac{d}{dt}\int_{-\infty}^{t}\cos(\Omega_i(t-t'))\hat{x}(t')dt'\right], \tag{2.28}$$

where we have introduced

$$\hat{x}_i^{(0)}(t) = \hat{x}_i(0)\cos(\Omega_i t) + \frac{\hat{p}_i(0)}{m_i\Omega_i}\sin(\Omega_i t) \tag{2.29}$$

for ease of use. This allows us to more succinctly write our equation of motion for $x(t)$ as

$$F(t) = m\ddot{\hat{x}} + m{\Omega'_x}^2\hat{x} + k_{\text{bath}}\hat{x} + \int_{-\infty}^{t}\gamma(t-t')\dot{\hat{x}}(t')dt', \tag{2.30}$$

where we have defined $F(t) = \sum_i C_i\hat{x}_i^{(0)}(t)$, ${\Omega'_x}^2 = \Omega_x^2 + k_{\text{bath}}/m$, k_{bath} is the average of k_i, and $\gamma(t)$ is our now time dependent damping term. If we make the first Markov approximation [42] $\gamma(t) = \gamma\delta(t)$, then we recover the classical form for the oscillator

$$F(t) = m\ddot{\hat{x}} + m{\Omega'_x}^2\hat{x} + \gamma\dot{\hat{x}}, \tag{2.31}$$

albeit with a modified frequency. This approximation removes any memory in the bath which results in our white-noise process as expected. We can also look at correlations in the force term which have been shown [43, 44] to be

$$\frac{1}{2}\left\langle F(t)F(t') + F(t')F(t)\right\rangle = \frac{m\gamma}{\pi}\int_0^{\infty} d\omega\hbar\omega\coth\left(\frac{\hbar\omega}{2k_BT_{\text{bath}}}\right)\cos(\omega(t-t')), \tag{2.32}$$

$$= m\gamma k_BT\frac{d}{dt}\coth\left(\frac{\pi k_BT_{\text{bath}}(t-t')}{\hbar}\right) \tag{2.33}$$

which in the classical limit of $\hbar \to 0$ simplifies to

$$\frac{1}{2}\left\langle F(t)F(t') + F(t')F(t)\right\rangle = 2m\gamma k_BT_{\text{bath}}\delta(t-t'), \tag{2.34}$$

which is inline with the classical case.

We can analogously calculate $S_{xx}(\omega)$ in the quantum regime, however we will look at the more general PSD $S_{x^Nx^N}(\omega)$ for arbitrary powers of x. This has been calculated [45] to be

$$S_{x^Nx^N}(\omega) = \gamma x_{\text{zpf}}^{2N}\sum_{i=0}^{\lfloor N/2\rfloor}\sum_{j=0}^{N-2i}\frac{N\alpha_{ij}^{(N)}(2\langle n\rangle+1)^{2i}(\langle n\rangle+1)^{N-2i-j}\langle n\rangle^{j}}{[\omega-(N-2i-2j)\Omega'_x]^2+\left(N\frac{\gamma}{2}\right)^2} \tag{2.35}$$

where $x_{\mathrm{zpf}} = \sqrt{\hbar/2m\Omega'_x}$ is the zero point fluctuation of this oscillator, $\langle n\rangle = \frac{1}{e^{\hbar\Omega'_x/k_BT}-1}$ is the coherent amplitude of the motional state, and

$$\alpha_{ij}^{(N)} = \frac{1}{2^{2i}j!(N-2i-j)!}\frac{(N!)^2}{(i!)^2}. \tag{2.36}$$

These higher order motions can appear in detection and we can recover $S_{xx}(\omega)$, which takes the simple form of

$$S_{xx}(\omega) = \gamma x_{\mathrm{zpf}}^2\left[\frac{\langle n\rangle + 1}{(\omega-\Omega'_x)^2 + \left(\frac{\gamma}{2}\right)^2} + \frac{\langle n\rangle}{(\omega+\Omega'_x)^2 + \left(\frac{\gamma}{2}\right)^2}\right]. \tag{2.37}$$

Note that in the high temperature limit we recover the spectrum of the classical thermal mechanical oscillator in Equation 2.18.

2.2.3 Phononic Representation

It is often more favourable to work in the phononic basis of a harmonic oscillator, especially when looking at quantum behaviour. To that end, we will introduce the creation and annihilation operators $\hat{b}^\dagger$ and $\hat{b}$ of phonons of the particle's motion with

$$\hat{x} = x_{\mathrm{zpf}}\left(\hat{b}^\dagger + \hat{b}\right), \tag{2.38}$$

$$\hat{p} = \frac{i\hbar}{2x_{\mathrm{zpf}}}\left(\hat{b}^\dagger - \hat{b}\right), \tag{2.39}$$

$$[\hat{b}, \hat{b}^\dagger] = 1. \tag{2.40}$$

It is then natural to work in the basis of Fock states with

$$\hat{b}\left|n\right\rangle = \sqrt{n}\left|n-1\right\rangle, \tag{2.41}$$

$$\hat{b}^\dagger\left|n\right\rangle = \sqrt{n+1}\left|n+1\right\rangle, \tag{2.42}$$

$$\implies \hat{n} = \hat{b}^\dagger\hat{b}\left|n\right\rangle = n\left|n\right\rangle. \tag{2.43}$$

Given that these phonons are bosons, we know that in thermal equilibrium they follow Bose-Einstein statistics which means

$$\bar{n} = \langle \hat{n} \rangle = \frac{1}{e^{-\hbar\Omega'_x/k_B T} - 1}. \tag{2.44}$$

This allows us to better understand the phononic occupation in Equations 2.35 and 2.37.

The connection between the displacement PSD and the phononic occupation provides an opportunity to do so-called Raman sideband asymmetry thermometry[46]. From Equation 2.37 we can see that the ratio of sideband heights gives us a measure of the phononic occupation. More robust to noise would be to integrate $S_{xx}(\omega)$ around $\pm\Omega'_x$ instead of just the peak heights but the logic remains the same. This will be explored more in Chapter 6.

Working in this basis, one can show [47] that the transition rates between phonon occupations due to a linear force can be written as

$$\gamma_{n\to n+1} = (n+1)\gamma_\uparrow = (n+1)\frac{x_{\mathrm{zpf}}^2}{\hbar^2} S_{FF}(-\Omega'_x), \tag{2.45}$$

$$\gamma_{n\to n-1} = n\gamma_\downarrow = n\frac{x_{\mathrm{zpf}}^2}{\hbar^2} S_{FF}(\Omega'_x). \tag{2.46}$$

and then the dissipation rate is $\gamma = \gamma_\downarrow - \gamma_\uparrow$. That is, the increase and decrease of the particle's motion is linked spectroscopically with the noise. Following [48], for some out of equilibrium state with occupation $\bar{n}$, the corresponding equation of motion for the occupation is

$$\dot{\bar{n}} = \Gamma - \gamma\bar{n} \tag{2.47}$$

where we identify Γ as our heating rate.

2.3 Heating Rates and Dissipation

One of the advantages a levitated optomechanical system has over a tethered system is its isolation from environmental noise and the absence of dissipation due to intrinsic losses in the material. However, there are still some channels by which noise can couple to the oscillator. We will outline a number of relevant noise sources and how they impact the phononic occupation of the oscillator.

2.3.1 Background Gas Collisions

A common realisation of the aforementioned damping or white noise force would be the random collisions of gas molecules with the oscillator. These collisions give rise to the well known Brownian motion we previously analyzed. To proceed, let us again assume our oscillator is a spherical particle of radius r. We can assume the collisions are isotropic in a standard vacuum chamber environment. For low pressures, ($P < 10$mbar), it has been shown [19] that the gas damping can be approximated by

$$\gamma_{\mathrm{bath}} = \frac{16}{\pi}\frac{P}{\bar{v}_{\mathrm{gas}}\rho r} \tag{2.48}$$

where $\bar{v}_{\mathrm{gas}}$ is the average speed of the background gas, and ρ is the density of the oscillator. Following [49], the velocity distribution of a gas is well described by the Maxwell-Boltzmann distribution

$$\frac{dn}{dv} = \frac{1}{\sqrt{2\pi}}\left(\frac{m_{\mathrm{gas}}}{kT_{\mathrm{gas}}}\right)^{\frac{3}{2}} v^2 e^{-\frac{m_{\mathrm{gas}}v^2}{2k_B T_{\mathrm{gas}}}} \tag{2.49}$$

where dn/dv is the relative number of particles with velocities between v and $v + dv$, m is the mass of the gas particles, and T is their temperature. The mean velocity of this distribution is $\bar{v}_{\mathrm{gas}} = \sqrt{8k_B T_{\mathrm{gas}}/\pi m_{\mathrm{gas}}}$. Note the dependence on the molecular mass in which case our background gas composition can significantly change our damping. In particular if the gas is predominantly hydrogen, as is often the case in high-vacuum systems, we would have a gas damping rate of $\gamma_{\mathrm{bath}}/2\pi \sim 10^2$Hz while if the makeup is air the damping would be $\gamma_{\mathrm{bath}}/2\pi \sim 10^3$Hz, both at nominal pressure of 1mbar and room temperature.

Following the calculation of Equation 2.47, for this white noise force we get

$$\dot{\bar{n}} = \gamma_{\mathrm{bath}}\left(\bar{n}_{\mathrm{bath}} - \bar{n}\right) \tag{2.50}$$

where $\bar{n}_{\text{bath}}$ is the occupation of the bath. For a room temperature environment this is simply $\bar{n}_{\text{bath}} = \frac{k_B T_{\text{room}}}{\hbar \Omega_x'}$. This describes the heating of the oscillator until it is in thermal equilibrium with the bath. We can then identify our heating rate due to the bath as $\Gamma_{\text{bath}} = \gamma_{\text{bath}} \bar{n}_{\text{bath}}$. At the base pressure of our system, substituting in Equation 2.48 for γ_{bath}, we find that $\Gamma_{\text{bath}}/2\pi \sim 10^3$Hz at standard operating parameters [50]. More sophisticated models of gas damping have been investigated in the context of levitated optomechanics [34] and provide some corrections to this estimate which take into account the internal temperature of the levitated nanoparticle.

2.3.2 Intensity Noise

Additional heating effects come from fluctuations in the trapping potential. Until now, we have considered a static harmonic potential which has removed many physical mechanisms. Variations in the harmonic potential strength can cause heating.

The effect of classical intensity noise on the trapping potential can be modeled as a time dependent shift in the mechanical frequency $\Omega_x^2 \to \Omega_x^2(1+\epsilon(t))$ which gives rise to a forcing term in our equation of motion proportional to x. It has then been shown [51] that this would give rise to an equation of motion for the occupation as

$$\dot{\bar{n}} = \frac{\gamma_{\text{RIN}}}{2} + \gamma_{\text{RIN}} \bar{n} \tag{2.51}$$

where

$$\gamma_{\text{RIN}} = \frac{\pi}{2} \Omega_x^2 S_{\text{RIN}}(2\Omega_x) \tag{2.52}$$

where S_{RIN} is the PSD of the residual intensity noise (RIN). Note then in this case, γ_{RIN} acts to amplify motion while γ_{bath} dampens the motion. Also, the fact that we are interested in the spectrum of the noise at twice the mechanical frequency is because this is equivalent to a parametric drive. We identify $\Gamma_{\text{RIN}} = \gamma_{\text{RIN}}/2$ as the heating contribution and for standard operation parameters and $S_{\text{RIN}}(2\Omega_x) \approx -130$dB/Hz, this comes out to be $\Gamma_{\text{RIN}}/2\pi \sim 10^{-4}$Hz. While the heating may be small for most cases, the amplification effect can be strong.

2.3.3 Trap Shaking

Alternative to intensity noise is the center of the harmonic potential moving. This could be due to beam stearing or other vibrations in the environment coupling into our system. For positioning noise, we take $x(t) \rightarrow x(t) - \epsilon(t)$, in which case $\dot{\bar{n}} = \Gamma_{\text{pos}}$ where

$$\Gamma_{\text{pos}} = \frac{\pi}{2} \frac{m\Omega_x^3}{\hbar} S_{\text{pos}}(\Omega_x). \tag{2.53}$$

Note that there is no damping associated with the movement of the potential center. Accurately measuring our S_{pos} is difficult in our experimental setup but given our results in Chapter 6, we can estimate it to be $< 10^{-15}$dB/Hz based on [52].

2.3.4 Photon Recoil

The generation of the optical potential is done, in our case, through the use of an optical tweezer discussed in Chapter 5. Taking a more detailed look, beyond modeling it as just a harmonic potential, we see that the scatter of photons off of the particle can also heat the particle motion due to shot noise. To a good approximation, this coupling is independent of position (since the particle is localized in the optical field) but provides a momentum impulse and thus is a contribution to $F(t)$. The PSD of the force due to the recoil of scattered photons is

$$S_{FF}^{(\text{rec})} = \frac{\hbar\omega_{\text{light}}}{c^2} P_{\text{scatt}}(\theta, \phi) \tag{2.54}$$

where $P_{\text{scatt}}(\theta, \phi)$ is the component of the total power scattered along some direction $\hat{r}_{\theta,\phi} = (\cos\theta, \sin\theta\cos\phi, \sin\theta\sin\phi)$ with the dipole aligned to $(1, 0, 0)$.

In this case, for a radiating dipole,

$$P_{\text{scatt}}(\theta,\phi) = \int_0^{2\pi}\int_0^{\pi} \frac{3}{8\pi} P_{\text{scatt}}^{\text{total}} \sin^2\theta' (\hat{r}_{\theta',\phi'}\cdot\hat{r}_{\theta,\phi})^2 \sin\theta' d\theta' d\phi' \tag{2.55}$$

$$= \frac{P_{\text{scatt}}^{\text{total}}}{5}\left|\left(1,\sqrt{2},\sqrt{2}\right)\cdot\hat{r}_{\theta,\phi}\right|^2. \tag{2.56}$$

where $P_{\text{scatt}}^{\text{total}} = \sigma_{\text{scatt}} I$ with I and σ_{scatt} is the scattering cross-section. The scattering cross-section is given by

$$\sigma_{\text{scatt}}^{\text{total}} = \frac{1}{6\pi}\frac{|\alpha|^2 k^4}{\epsilon_0^2} \tag{2.57}$$

where $\alpha = 4\pi\epsilon_0 r^3 \frac{n^2-1}{n^2+1}$, and k is the wavevector of the impinging light, r is the particle radius and n is its index of refraction. If we take the dipole to be oriented along the y-direction then $P_{\text{scatt}}^{(y)} = \frac{1}{5}P_{\text{scatt}}^{\text{total}}$, and $P_{\text{scatt}}^{(x)} = P_{\text{scatt}}^{(z)} = \frac{2}{5}P_{\text{scatt}}^{\text{total}}$. From [47], we know that

$$\dot{\bar{n}} = \frac{1}{2m\hbar\Omega_x}\bar{S}_{FF}(\Omega_x) = \frac{1}{5}\frac{\sigma_{\text{scatt}} I}{mc^2}\frac{\omega_{\text{light}}}{\Omega_x} = \Gamma_{\text{scatt}}. \tag{2.58}$$

where $\bar{S}_{FF}(\Omega_x) = \frac{S_{FF}(\Omega_x)+S_{FF}(-\Omega_x)}{2}$. Note that for heating along the axes perpindicular to the dipole axis, the heating rate is twice this value. Typically, we operate with $I \sim 10^{11}\text{W/m}^2$, which gives a heating rate of $\Gamma_{\text{scatt}}/2\pi \sim 10^3\text{Hz}$.

2.3.5 Black Body Radiation

Besides scattering, the particle can also absorb light, both from the tweezer and from the environment. The former can heat up the particle causing substantial blackbody emission which will also cause heating of the motion while the latter can act just like the scattering force and cause heating. These blackbody terms are not well known for our system. For bulk systems

[53], the blackbody localization parameters are

$$\Lambda_{\text{bb, scatt}} = \frac{8!8\zeta(9)\pi^{1/3}}{9}\text{Re}\left\{\frac{\epsilon_{bb}-1}{\epsilon_{bb}+2}\right\}^2 cr^6\left(\frac{k_B T_e}{\hbar c}\right)^9, \tag{2.59}$$

$$\Lambda_{\text{bb, abs(em)}} = \frac{16\pi^6\pi^{1/3}}{189}\text{Im}\left\{\frac{\epsilon_{bb}-1}{\epsilon_{bb}+2}\right\} cr^3\left(\frac{k_B T_{e(i)}}{\hbar c}\right)^6, \tag{2.60}$$

where λ_{th} is the wavelength of the thermal photons which is roughly ~ 1mm for our operating temperatures, $\epsilon_{bb} = 2.1{+}i0.57$ and $T_{e(i)}$ are the environment (internal) temperatures. We can relate these localization parameters to the heating rate through $\Gamma = \Lambda x_{\text{zpf}}^2$. Its been shown that particles can heat up to ~ 10^3K [34] which gives $\Gamma_{\text{bb, scatt}}/2\pi \sim 10^{-9}$,$\Gamma_{\text{bb, abs}}/2\pi \sim 10^{-6}$, and $\Gamma_{\text{bb, em}}/2\pi \sim 10^{-3}$ in a room temperature environment. These are negligible then compared to other heating rates in our system except under freefall conditions in UHV. This will be discussed in more detail later.

One should note however that the usage of bulk expressions has been shown to poorly model the behaviour of some microscopic systems [54]. In our current pressure regimes, our heating is well described by the dominant gas and recoil terms. In the future when the system can reach UHV we will be able to investigate the true impact of black-body radiation on the system.

Chapter 3

Optical Cavities

We will now give a short overview of the relevant physics of optical cavities. We will start with building our intuition and understanding through a classical picture before considering our cavity in a quantum formalism. The apparatus we will consider is shown in Figure 3.1.

3.1 Classical Optical Modes

There are many forms of optical cavity which can broadly be classified into travelling and standing wave resonators. We will focus exclusively on the latter but many of the same insights can be applied to travelling wave resonators. In the case of standing wave resonators, the round trip accumulated phase inside the resonator sets a condition on the allowed frequency of light through interference. This leads to the definition of the Free Spectral Range (FSR)

$$\omega_{\mathrm{FSR}} = \frac{2\pi c}{2nL} \tag{3.1}$$

where c is the speed of light vacuum, n is the refractive index of the medium in which the light travels and L is the path length of the resonator. We can then define the Finesse as

$$\mathcal{F} = \frac{\pi\sqrt{|r|}}{1-|r|} \tag{3.2}$$

where $|r| = \sqrt{\mathcal{R}_1\mathcal{R}_2}e^{-\alpha_s L}$ is the complex round-trip attenuation factor with $\mathcal{R}_{1,2}$ the mirror reflectances and α_s is the coefficient of loss associated with absorption and scattering within the cavity and not transmission through the mirrors. The finesse effectively quantifies the losses in the system in which case a lossless system would take $\mathcal{F} \to \infty$ as $|\mathcal{R}_{1,2}| \to 1$. This can then

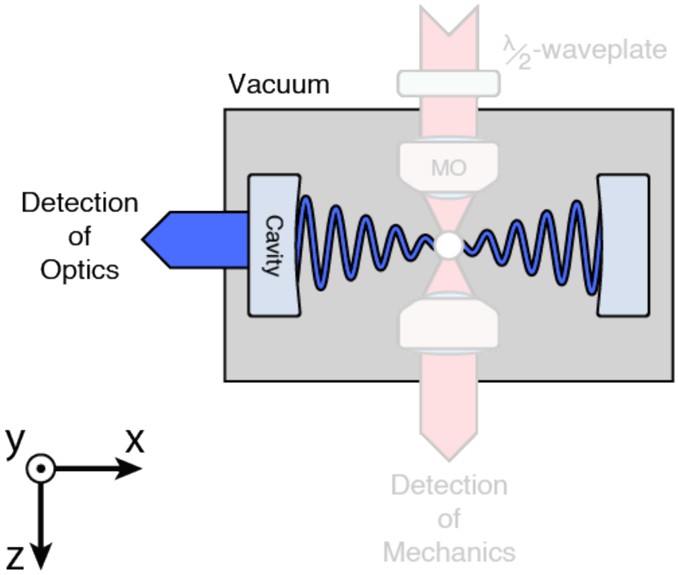

Figure 3.1: **A sketch of a cavity system.** A cavity mode (blue) exists within an optical cavity. The light can transmit through one of the cavity mirrors and subsequently be used to detect the cavity mode. In this dissertation, the cavity is placed inside of a vacuum chamber.

be related to the spectral linewidth on the resonator $\kappa \approx \omega_{\text{FSR}}/\mathcal{F}$. This is oftentimes referred to as the energy decay rate as it quantifies the exponential decay of the energy of the light accumulated inside of the resonator.

If we then consider the resonator in 3D space, the spatial modes of the cavity can be decomposed into Hermite-Gaussian modes. In this case, we have to modify the frequency spacing to account for the spatial variation in the phase. For a frequency or longitudinal mode q and Hermite-Gauss mode (l, m) we have a frequency of

$$\omega_{q,l,m} = \omega_{\text{FSR}} q + (l + m + 1)\frac{\Delta\zeta}{\pi}\omega_{\text{FSR}} \tag{3.3}$$

where $\Delta\zeta = \zeta(z_2) - \zeta(z_1)$ is the difference in Guoy phase at the two mirror surfaces. Alternatively, we can make the connection to the geometry of the cavity more evident by writing this as $\Delta\zeta = \cos^{-1}(g_1 g_2)$ where the so-called g-parameters are defined as $g_i = 1 + L/R_i$ where R_i is the radius of curvature of the mirror. For reference, a near-confocal cavity has $g_i \approx 0$ in which case

$$\omega_{q,l,m}^{(Near-Confocal)} \approx \omega_{\text{FSR}}\left(q + \frac{l + m + 1}{2}\right) \tag{3.4}$$

with a mode structure depicted in Figure 3.2. We have assumed here that the cavity is cylindrically symmetric and therefore $\omega_{q,l,m} = \omega_{q,m,l}$ but this is not in general true. In that case, one would need to use different radii of curvature for the different axes to compute the resonance conditions. It's also possible that the mirrors are not symmetric in size along the different axes which can also have an effect.

Furthermore, if the cavity mirrors have some birerefringence, the degenaracy of polarization modes can in-principle be lifted. A phase difference can be thought of as a path difference length difference, leading to different frequency modes. These shifts are usually small compared to ω_{FSR} but can be large relative to the cavity linewidth in which case they are resolvable.

As the name implies, these standing wave resonators have a standing

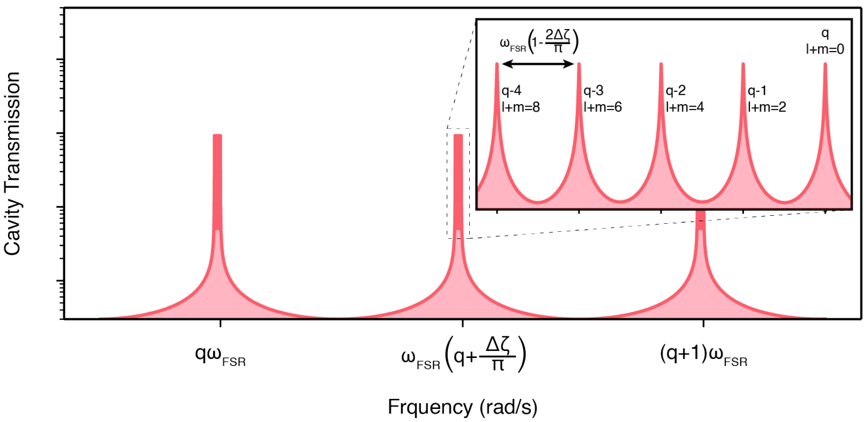

Figure 3.2: **The cavity mode structure of a near-confocal cavity.** The Hermite-Gauss modes split into group where $l+m$ is even and odd with the spacin between these groups being $\sim \omega_{\mathrm{FSR}}/2$. Within the groups, the different values of $l+m$ again split with a finer mode spacing.

wave intensity profile. For a symmetric cavity this simplifies to

$$\begin{aligned} I(x,y,z) = 2|E_0|^2 \frac{W_0^2}{W(z)^2} e^{-2\frac{x^2+y^2}{W(z)^2}} \left| H_l\left[\frac{\sqrt{2}x}{W(z)}\right] H_m\left[\frac{\sqrt{2}y}{W(z)}\right] \right|^2 \\ \times \left[1+\cos\left(2kz + k\frac{x^2+y^2}{R(z)} - 2(l+m+m)\zeta(z)\right)\right] \end{aligned} \tag{3.5}$$

$$\tag{3.6}$$

where W_0 is the beam waist, $W(z)$ is the beam size as a function of position along the cavity axis, H_i is the i^{th} Hermite polynomial and $R(z)$ is the radius of curvature of the wavefront. One can in-principle determine the power of the intracavity field stemming from some external drive based off of the specifications of the cavity reflectances and the mode matching between the drive field and the cavity mode.

A final set of useful quantities are the cavity mode volume V_{cav} and the cavity quality factor Q_{cav}. These can be thought of as quantifying the spatial and temporal confinement of the light in the cavity respectively. The mode volume was introduced by Purcell [1] and we define it as

$$V_{\text{cav}} = \int_V \frac{I(\vec{x})}{I_{\text{max}}} d^3x, \tag{3.7}$$

where I_{max} is the maximum intensity in the cavity. One can show that with a gaussian mode, we find that $V_{\text{cav}} \approx \frac{\pi}{4} L w_0^2$. The quality factor relates the energy stored inside the resonator to the energy dissipated per oscillatory cycle. This can be quantified as

$$Q_{\text{cav}}(\omega) = \frac{\omega}{\kappa} \approx \frac{\omega}{\omega_{\text{FSR}}} \mathcal{F}. \tag{3.8}$$

This is inline with our definition of the quality factor for a mechanical oscillator in Chapter 2.

3.2 Quantum Optical Modes

In second quantization, the complex electric field amplitude $\vec{E}_{\text{cav}}$ for a cavity oriented along the $x-$direction is given by

$$\vec{E}_{\text{cav}}(\vec{x}) = E_0^{(cav)} \hat{\epsilon}_{\text{cav}} \frac{1}{q_{cav}(x)} \cos(k_{\text{cav}} x) e^{-ik_{\text{cav}} \frac{y^2+z^2}{2q_{cav}(x)}} \hat{a} \tag{3.9}$$

where $E_0^{(cav)} = \sqrt{\frac{\hbar\omega_{cav}}{2\epsilon_0 V_{cav}}}$, $\hat{\epsilon}_{cav}$ is the unit vector defining the field polarization, $q_{cav}(x)$ is the complex gaussian beam parameter, and $k_{\text{cav}} = \frac{\omega_{\text{cav}}}{c}$ is the wavenumber for the specific cavity mode with field creation and annihilation operators $\hat{a}$ and $\hat{a}^\dagger$ with the relation $[\hat{a}, \hat{a}^\dagger] = 1$. We will then consider external mode operators $\hat{c}(\omega)$ and $\hat{c}^\dagger(\omega)$ (with $[\hat{c}(\omega), \hat{c}^\dagger(\omega')] = \delta(\omega - \omega')$) that couple to this cavity. Following [55] we can describe such a system by the Hamiltonian

$$\hat{H}_{\text{cav}} = \hbar\omega_{\text{cav}} \hat{a}^\dagger \hat{a} + \int_{-\infty}^{\infty} d\omega \hbar\omega \hat{c}^\dagger(\omega)\hat{c}(\omega) + i\hbar \int_{-\infty}^{\infty} d\omega g(\omega) \left(\hat{c}^\dagger(\omega)\hat{a} - \hat{a}^\dagger \hat{c}(\omega)\right) \tag{3.10}$$

where $g(\omega)$ describes the coupling of the cavity to the environment. One can show that the Heisenberg equation of motion for the external operators are

$$\dot{\hat{c}}(\omega) = -i\omega\hat{c}(\omega) + \hat{a}g(\omega). \tag{3.11}$$

the solution to which is

$$\hat{c}(\omega) = e^{-i\omega(t-t_0)}\hat{c}_0(\omega) + g(\omega)\int_{t_0}^{t} e^{-i\omega(t-t')}\hat{a}(t')dt' \tag{3.12}$$

where $\hat{c}_0(\omega) = \hat{c}(\omega)|_{t=t_0}$ where t_0 is some initial time before t. Alternatively, we can write a time reversed solution

$$\hat{c}(\omega) = e^{-i\omega(t-t_f)}\hat{c}_f(\omega) - g(\omega)\int_{t}^{t_f} e^{-i\omega(t-t')}\hat{a}(t')dt' \tag{3.13}$$

where $\hat{c}_f(\omega) = \hat{c}(\omega)|_{t=t_f}$ where t_f is some time later than t. To maintain normal ordering with respect to creation and annihilation operators, we can rewrite our Hamiltonian in terms of these forwards and backwards propagating solutions. It will help to make the first Markov approximation by assuming $g(\omega) = \sqrt{\kappa/2\pi}$ for all frequencies of interest. Focusing on the interaction term, we get that

$$\begin{aligned}\hat{H}_{\text{Int}} &= i\hbar\int_{-\infty}^{\infty} d\omega g(\omega)\left(\hat{c}^\dagger(\omega)\hat{a} - \hat{a}^\dagger\hat{c}(\omega)\right) && (3.14)\\ &= i\hbar\left[\sqrt{\kappa}\left(\hat{a}^\dagger_{\text{Out}}\hat{a} + \hat{a}^\dagger\hat{a}_{\text{In}}\right) - \kappa\hat{n}\right] && (3.15)\end{aligned}$$

where we have defined

$$\begin{aligned}\hat{a}_{\text{In}}(t) &= -\frac{1}{\sqrt{2\pi}}\int_{-\infty}^{\infty} d\omega e^{-i\omega(t-t_0)}\hat{c}_0(\omega), && (3.16)\\ \hat{a}_{\text{Out}}(t) &= +\frac{1}{\sqrt{2\pi}}\int_{-\infty}^{\infty} d\omega e^{-i\omega(t-t_f)}\hat{c}_f(\omega). && (3.17)\end{aligned}$$

We can relate the definitions of $\hat{a}_{\text{In}}(t)$ and $\hat{a}_{\text{Out}}(t)$ through

$$\begin{aligned}\frac{1}{\sqrt{2\pi}}\int_{-\infty}^{\infty}\hat{c}(\omega)d\omega = -\hat{a}_{\text{In}}(t) + \frac{\sqrt{\kappa}}{2}\hat{a}(t) &= \hat{a}_{\text{Out}}(t) - \frac{\sqrt{\kappa}}{2}\hat{a}(t), && (3.18)\\ \implies \sqrt{\kappa}\hat{a}(t) &= \hat{a}_{\text{Out}}(t) + \hat{a}_{\text{In}}(t). && (3.19)\end{aligned}$$

Next, using this relation we can construct the commutators between some system observable $\hat{X}(t)$ and $\hat{a}_{\mathrm{In}}(t)$ and $\hat{a}_{\mathrm{Out}}(t)$. Observe that

$$\left[X(t), \hat{a}_{\mathrm{In}}(t')\right] = u(t-t')\sqrt{\kappa}\left[X(t), \hat{a}(t')\right] \tag{3.20}$$

$$\left[X(t), \hat{a}_{\mathrm{Out}}(t')\right] = u(t'-t)\sqrt{\kappa}\left[X(t), \hat{a}(t')\right] \tag{3.21}$$

where

$$u(t) = \begin{cases} 0 & t < 0 \\ \frac{1}{2} & t = 0 \\ 1 & t > 0 \end{cases} \tag{3.22}$$

We are now equipped to look at the equation of motion for our system operators. We will start by looking at the equation of motion of the cavity occupation $\hat{n} = \hat{a}^\dagger \hat{a}$. Observe that

$$\dot{\hat{n}} = -\frac{i}{\hbar}\left[\hat{n}, \hat{H}_{\mathrm{cav}}\right] = -\frac{i}{\hbar}\left[\hat{n}, i\hbar\sqrt{\kappa}\left(\hat{a}^\dagger_{\mathrm{Out}}\hat{a} + \hat{a}^\dagger\hat{a}_{\mathrm{In}}\right)\right] \tag{3.23}$$

$$= \sqrt{\kappa}\left(\hat{a}^\dagger\hat{a}_{\mathrm{In}} - \hat{a}^\dagger_{\mathrm{Out}}\hat{a}\right). \tag{3.24}$$

We can now ascribe physical meaning to the different terms in our conveniently labelled Hamiltonian. We can intuitively read the first term as annihilating a photon from the external modes before time t and then creating a photon inside the cavity while the second term means to annihilate a photon from inside the cavity at time t and creating one outside at some later time. We see that $\hat{a}_{\mathrm{In}}(t)$ and $\hat{a}_{\mathrm{Out}}(t)$ represent the incoming and outgoing fields from the cavity and κ is the classical energy decay rate mentioned previously. If the driving term $\hat{a}_{\mathrm{In}}(t)$ is dropped then we recover the exponential decay of the cavity occupation $\hat{n} = n_0 es^{-\kappa t}$ which matches the classical case as our intuition would suggest.

For completeness, we note that for a double-sided cavity we can't just substitute $\kappa = \kappa_1 + \kappa_2$ but rather introduce an additional environment term for each output leading to a multiplication of all coupling terms.

From this physical connection, we can think about restructuring our Hamiltonian into something that more clearly represents our experiment of interest. In particular, we want to consider a situation where we are driving the cavity with some coherent field at frequency ω_d. This is equivalent to applying the displacement operator $\hat{D}(\alpha(t))$ to our Hamiltonian. Specifically,

$$\hat{D}(\alpha(t)) = e^{\alpha_{\text{In}}(t)\hat{c}^\dagger(\omega_d) - \alpha^*_{\text{In}}(t)\hat{c}(\omega_d)} \tag{3.25}$$

where $\alpha_{\text{In}}(t) = |\alpha_{\text{In}}|e^{-i(\omega_d t+\phi)}$. This results in a Hamiltonian

$$\hat{H}_{\text{cav}} \to \hbar\omega_{\text{cav}}\hat{a}^\dagger\hat{a} + \int_{-\infty}^{\infty} d\omega\hbar\omega\hat{c}^\dagger(\omega)\hat{c}(\omega) + i\hbar\sqrt{\kappa}(\hat{a}^\dagger\hat{a}_{\text{In}} - \hat{a}^\dagger_{\text{In}}\hat{a}) + i\hbar E_d(e^{-i(\omega_d t+\phi)}\hat{a}^\dagger - e^{i(\omega_d t+\phi)}\hat{a}) \tag{3.26}$$

where $E_d = \sqrt{\frac{\kappa}{2\pi}}|\alpha_{\text{In}}|$. From our classical understanding of cavities, we can identify that $|\alpha_{\text{In}}| = \sqrt{P_{\text{in}}/\hbar\omega_d}$ with units of $\sqrt{\text{photons/s}}$. Switching to the interaction picture by rotating at the drive frequency through the unitary

$$\hat{U}(t) = e^{i\omega_d t\left[\hat{a}^\dagger\hat{a} + \int_{-\infty}^{\infty} d\omega\hat{c}^\dagger(\omega)\hat{c}(\omega)\right]} \tag{3.27}$$

puts our Hamiltonian in the final form

$$\hat{H}^{(\text{rot.})}_{\text{cav}} = \hbar\Delta\hat{a}^\dagger\hat{a} + \int_{-\infty}^{\infty} d\omega\hbar(\omega-\omega_d)\hat{c}^\dagger(\omega)\hat{c}(\omega) + i\hbar\sqrt{\kappa}(\hat{a}^\dagger\hat{a}_{\text{In}} - \hat{a}^\dagger_{\text{In}}\hat{a}) + i\hbar E_d(e^{-i\phi}\hat{a}^\dagger - e^{i\phi}\hat{a}) \tag{3.28}$$

where $\Delta = \omega_{\text{cav}} - \omega_d$. In this picture, we can clearly identify the different effects. The last term is for the classical cavity drive component while the second last term is the coupling of fluctuations.

We can now return to our internal mode operators and we can quickly see that

$$\dot{\hat{a}} = -\frac{i}{\hbar}\left[\hat{a}, \hat{H}^{(\text{rot.})}_{\text{cav}}\right] = -i\Delta\left[\hat{a}, \hat{a}^\dagger\hat{a}\right] + E_d e^{-i\phi}\left[\hat{a}, \hat{a}^\dagger\right] + \sqrt{\kappa}\left(\left[\hat{a}, \hat{a}^\dagger\right]\hat{a}_{\text{In}} - \left[\hat{a}, \hat{a}^\dagger_{\text{In}}\right]\hat{a}\right) \tag{3.29}$$

$$= -i\Delta\hat{a} + E_d e^{-i\phi} + \sqrt{\kappa}\hat{a}_{\text{In}} - \frac{\kappa}{2}\hat{a}, \tag{3.30}$$

$$\implies \alpha_0 \equiv \langle\hat{a}\rangle = \frac{E_d e^{-i\phi}}{\frac{\kappa}{2} + i\Delta}. \tag{3.31}$$

In steady-state, one can then show that the cavity occupation is

$$\langle \hat{n} \rangle = |\alpha_0|^2 = \frac{E_d^2}{\Delta^2 + \left(\frac{\kappa}{2}\right)^2} \tag{3.32}$$

which relates the number of photons inside of the cavity to the amplitude of the drive. We can then choose the phase of the drive ϕ such that α_0 is real.

Let us now displace the cavity field by the amplitude found in Equation 3.31 which results in

$$\begin{aligned}\hat{H}_{\text{cav}} \to \hbar\Delta\hat{a}^\dagger\hat{a} + \int_{-\infty}^{\infty} d\omega\hbar(\omega-\omega_d)\hat{c}^\dagger(\omega)\hat{c}(\omega) + i\hbar\sqrt{\kappa}(\hat{a}^\dagger\hat{a}_{\text{In}} - \hat{a}_{\text{In}}^\dagger\hat{a}) + i\hbar E_d(e^{-i\phi}\hat{a}^\dagger - e^{i\phi}\hat{a}) \\ - i\hbar\sqrt{\kappa}\alpha_0\left(\hat{a}_{\text{In}}^\dagger - \hat{a}_{\text{In}}\right) + \hbar\Delta\left(|\alpha_0|^2 + \alpha_0\hat{a} + \alpha_0\hat{a}^\dagger\right).\end{aligned} \tag{3.33}$$

from which we can get the Langevin equation for our cavity operator

$$\dot{\hat{a}} = \left(\frac{\kappa}{2} - i\Delta\right)\hat{a} + \sqrt{\kappa}\hat{a}_{\text{in}}. \tag{3.34}$$

3.2.1 Relation to Caldeira-Legget

It is worth noting that the above relation is equivalent to that of the mechanical oscillator discussed in Chapter 2. Despite approaching the problem of dissipative systems from two different perspectives we have arrived at the same governing dynamics and Hamiltonian structure. This symmetry between the mechanical and optical subsystems will be exploited in Chapter 4 to simplify computations. This is a unique aspect of cavity optomechanics when compared with other quantum devices that rely on internal degrees of freedom with non-linearities.

Chapter 4

Levitated Cavity Optomechanics

We proceed by exploring the dynamics of a mechanical oscillator coupled to an optical cavity as illustrated in Figure 4.1. To do so, we will start with a simple generic linear coupling before demonstrating two mechanisms through which we realize this coupling in our experiment. Specifically, we will discuss a dispersive coupling mechanism which plays a small but critical role in our experiment before examining coupling via coherent scattering which is how we typically couple the particle to the cavity. As before, we will end with an outline of which noise sources need to be additionally considered in each case and how they impact our mechanical oscillator.

4.1 Linear Coupling

A simple model for a linear coupling between our mechanical oscillator and optical cavity can take the general form

$$\hat{H}_{\text{linear}} = g(\hat{b} + \hat{b}^\dagger)(\hat{a} + \hat{a}^\dagger). \tag{4.1}$$

Adding this coupling to our previous mechanical and optical Hamiltonians leads to the following Langevin equations

$$\dot{\hat{a}} \approx -\left(\frac{\kappa}{2} + i\Delta'\right)\hat{a} + \sqrt{\kappa}\hat{a}_{\text{In}} - ig\left(\hat{b} + \hat{b}^\dagger\right) \tag{4.2}$$

$$\dot{\hat{b}} \approx -\left(\frac{\gamma}{2} + i\Omega_x'\right)\hat{b} + \sqrt{\gamma}\hat{b}_{\text{In}} - ig\left(\hat{a} + \hat{a}^\dagger\right) \tag{4.3}$$

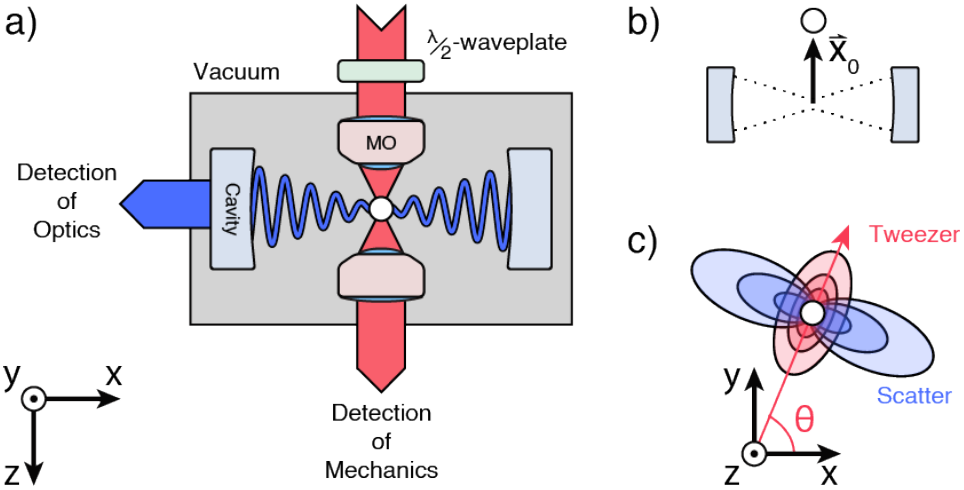

Figure 4.1: **A diagram of a general levitated cavity optomechanics setup.** (a) The combination of the levitated optomechanics and cavity setups we discussed in the previous chapters. The particle experiences both the tweezer (red) and cavity fields (blue). (b) Because the particle is generally positioned at the tweezer focus, its mean position $\vec{x}_0$ can be tuned relative to the cavity mode (dashed). (c) As previously discussed, the tweezer polarization can be tuned which modifies both the trap geometry as well as the dipole scattering orientation. The scatter happens orthogonal to the tweezer polarization and we set the overlap of the polarization of the cavity and the tweezer fields to be $|\hat{\epsilon}_{\mathrm{tw}} \cdot \hat{\epsilon}^*_{\mathrm{cav}}| \approx \cos\theta$.

where we have switched to an input-output formalism for the mechanics after we showed this gives rise to an analogous description of the dynamics.

We can easily solve these coupled Langevin equations in the Fourier domain whereby we can encode this system of equations into the matrix form

$$\begin{pmatrix} \sqrt{\kappa}\chi_l(\omega)\tilde{a}_{\text{In}}(\omega) \\ \sqrt{\kappa}\chi_l^*(-\omega)\tilde{a}_{\text{In}}^\dagger(\omega) \\ \sqrt{\gamma}\chi_m(\omega)\tilde{b}_{\text{In}}(\omega) \\ \sqrt{\gamma}\chi_m^*(-\omega)\tilde{b}_{\text{In}}^\dagger(\omega) \end{pmatrix} = \underbrace{\begin{pmatrix} 1 & 0 & ig\chi_l(\omega) & ig\chi_l(\omega) \\ 0 & 1 & -ig\chi_l^*(\omega) & -ig\chi_l^*(-\omega) \\ ig\chi_m(\omega) & ig\chi_m(\omega) & 1 & 0 \\ -ig\chi_m^*(-\omega) & -ig\chi_m^*(-\omega) & 0 & 1 \end{pmatrix}}_{M(\omega)} \begin{pmatrix} \tilde{a}(\omega) \\ \tilde{a}^\dagger(\omega) \\ \tilde{b}(\omega) \\ \tilde{b}^\dagger(\omega) \end{pmatrix}. \tag{4.4}$$

where

$$\chi_l(\omega) = \frac{1}{\frac{\kappa}{2} - i(\omega - \Delta)} \tag{4.5}$$

$$\chi_m(\omega) = \frac{1}{\frac{\gamma}{2} - i(\omega - \Omega)} \tag{4.6}$$

are the optical and mechanical susceptibilities respectively[2]. We can solve this set of equations by inverting this matrix[3]. Using the solutions, we can calculate the PSD of the mechanical motion

$$S_{xx}(\omega) = x_{zpf}^2|\nu(\omega)|^2\left[\gamma|\chi_m(\omega)|^2(\bar{N}+1) + \gamma|\chi_m(-\omega)|^2\bar{N} + g^2\kappa|\chi_l(\omega)|^2|\chi_m(\omega) - \chi_m^*(-\omega)|^2\right] \tag{4.7}$$

where

$$\nu(\omega) = \frac{1}{1 + g^2(\chi_l(\omega) - \chi_l^*(-\omega))(\chi_m(\omega) - \chi_m^*(-\omega))}. \tag{4.8}$$

An analogous result can be found for the intra-cavity field since the system

---

[2] This redefinition of the mechanical susceptibility is more convenient when working with $\hat{b}$ and $\hat{b}^\dagger$ and one could work with $\hat{x}$ and the old definition of mechanical susceptibility. The additional benefit here is the symmetry of the problem and solution which is rather elegant.

[3] The full calculation can be found in Appendix C.

is symmetric. Note that the first two terms in Equation 4.7 correspond to the uncoupled mechanical oscillator solution in Equation 2.37 and it is only the final term and the modulation $\nu(\omega)$ which modify the spectra. We will explore how the spectra looks for the different coupling regimes in later chapters. We simply note here that at high temperatures, the g^2 term can be neglected since N is large and $\nu(\omega)$ governs all of the coupling behaviour.

4.1.1 Optomechanical Cooperativity

We can then define the optomechanical cooperativity as the ratio between the heating rate associated with the cavity mode fluctuations and the heating rate from all other sources. This can then be written as

$$C = \frac{\Gamma_{\text{shot}}}{\sum_i \Gamma_i} \approx \frac{\frac{4g^2}{\kappa}}{\sum_i \Gamma_i}. \tag{4.9}$$

This quantifies the ability of the system to demonstrate quantum features. One example we will see in Chapter 6 is that the minimum phonon number depends on the cooperativity and in fact our oscillator requires $C > 1$ to reach ground state.

4.2 Dispersive Coupling

A common way of coupling a mechanical oscillator to an optical cavity is dispersively[4]. In this case, the particle motion causes position dependent phase modulation to the cavity field, imprinting the motion on the optical mode. The mechanical oscillator is, in the context of this dissertation, a nanoparticle trapped in an optical tweezer, positioned near the waist of a given cavity mode which is driven externally. In this case, due to the difference in the index of refraction of the particle and the medium inside the optical cavity, usually air, light propagating through the nanoparticle

---

[4] Historically, this started with tethered oscillators which cannot reasonably be coupled via coherent scattering as we will see later.

can experience a phase delay. It has been shown [19, 56] that this is

$$\frac{\delta\omega}{\omega} = -\frac{1}{2\epsilon_0}\frac{\int d^3r'\delta\vec{P}(\vec{r'})\cdot\vec{E}(\vec{r'})}{\int d^3r'\left|\vec{E}(\vec{r'})\right|^2}, \tag{4.10}$$

$$\approx -\frac{U_0}{\omega}f(y,z)\cos^2 k\hat{x} \tag{4.11}$$

where $\delta\vec{P}(\vec{r'})$ is the change in permittivity due to the polarizability of the dielectric object α_{ind}, $U_0 = \alpha_{\text{ind}}/2\epsilon_0 V_{\text{cav}}$ is the bare shift in the cavity frequency and $f(y,z)$ quantifies the relative change in intensity away from the central intensity, i.e. at the position of the cavity waist for a gaussian mode, $f(\vec{r}) = 1$. Note that we have chosen to use a longitudinal mode with an intensity maximum at the beam waist where $\langle\hat{x}\rangle = 0$. One can alternatively switch to a mode with an intensity minimum at the beam waist in which case we take $\cos^2(kx) \to \sin^2(kx)$ in the above expression.

Given this, we can write the dispersive term for our coupled Hamiltonian as

$$\hat{H}_{\text{disp}} = \hbar\delta\omega(\vec{r})\hat{a}^\dagger\hat{a} \to -\hbar U_0 f(y_0,z_0)\cos^2(k(x_0+\hat{x}))\left(\hat{a}^\dagger\hat{a} + \alpha_0\hat{a} + \alpha_0\hat{a}^\dagger + |\alpha_0|^2\right) \tag{4.12}$$

where we have applied the same displacement and rotation operators as in the cavity system as well as the analogous displacement of the position of the oscillator $\hat{x} \to x_0 + \hat{x}$. We can linearize this interaction by expanding in powers of $\hat{x}$. Then

$$\begin{aligned}\hat{H}_{\text{disp}} \approx &-\hbar U_0 f(y_0,z_0)\cos^2(kx_0)\left(\hat{a}^\dagger + \alpha_0\right)\left(\hat{a} + \alpha_0\right)\\ &+ \hbar g\left(\hat{b} + \hat{b}^\dagger\right)\\ &+ \hbar g_0\left(\hat{b} + \hat{b}^\dagger\right)\hat{a}^\dagger\hat{a}\\ &+ \hbar g\left(\hat{b} + \hat{b}^\dagger\right)\left(\hat{a} + \hat{a}^\dagger\right)\end{aligned} \tag{4.13}$$

where

$$g = g_0\alpha_0 = \frac{1}{2}\frac{\alpha_{\text{ind}}}{\epsilon_0 V_{\text{cav}}}kx_{zpf}f(y_0,z_0)\sin(2kx_0)\alpha_0 \tag{4.14}$$

is the total coupling rate while g_0 is the single photon coupling rate. The first term in Equation 4.13 is a shift in the cavity frequency due to the presence of the particle, the second term is a shift in the mean position of the particle, the third term is a single photon interaction term which is usually too weak to be of much consequence and the final term is our linear coupling. The shift of the cavity frequency and oscillator position can be compensated and therefore will not be of importance to us as proceed. Additionally, we will assume the coherent amplitude of the cavity is large enough that we can neglect the $\hat{a}^\dagger\hat{a}$. Then our dispersive coupling takes the same linear form we discussed previously

$$\hat{H}_{\text{disp}} \approx \hbar g \left(\hat{b} + \hat{b}^\dagger\right) \left(\hat{a} + \hat{a}^\dagger\right). \tag{4.15}$$

Although this can be compensated for, our g has implicitly become detuning dependent since $|\alpha_0|^2 = \frac{E_d^2}{\Delta^2 + (\kappa/2)^2}$. In other words, if we keep the drive amplitude fixed, changing the detuning changes the amount of light coupled into the cavity which changes the coupling rate to the particle. One can modify E_d to account for this so our limits are still the same but this may not always be feasible.

4.3 Coherent Scattering

An alternative scheme to dispersively coupling the particle to the cavity, by driving the cavity through one of its mirrors, is to drive the cavity through the scatter off of the nanoparticle itself. This so-called coherent scattering scheme has been explored in the context of ultracold atomic systems [57, 58] and more recently in levitated optomechanics [16, 17]. It serves a fundamental role in our experiment as it offers some key improvements when compared with dispersive coupling as we will see.

To start, let us consider the Hamiltonian for such a case. We can write down such an interaction through a dipole interaction as

$$\hat{H}_{\text{dip}} = -\frac{1}{2}\alpha_{\text{ind}}|\vec{E}(\vec{x})|^2 = -\frac{1}{2}\alpha_{\text{ind}}|\vec{E}_{\text{tw}}(\vec{x}) + \vec{E}_{\text{cav}}(\vec{x})|^2 \tag{4.16}$$

$$= -\frac{1}{2}\alpha_{\text{ind}}\left(|\vec{E}_{\text{tw}}(\vec{x})|^2 + |\vec{E}_{\text{cav}}(\vec{x})|^2\right) - \frac{1}{2}\alpha_{\text{ind}}\vec{E}_{\text{tw}}(\vec{x}) \cdot \vec{E}^{\dagger}_{\text{cav}}(\vec{x}) + \text{c.c.} \tag{4.17}$$

where the first and second terms give rise to the harmonic potential and dispersive coupling respectively. We will call the final terms $\hat{H}_{\text{CS}}$ as we will see they give rise to our coherent scattering interaction as the particle couples the fields of the tweezer and the cavity together. This Hamiltonian has been described in our system previously [16] but here we will take a slightly different approach to keep with the consistent input-output formalism we have thus far maintained.

Focusing on the interaction terms, we will make the simplifying assumption that the tweezer is a classical field, which amounts to the same approximations we have made before by taking the coherent amplitude to be large and thus dominate the interaction over the vacuum term. This is an especially good assumption in this case as the tweezer generally operates well above the single photon regime. Since the tweezer is generally not cylindrically symmetric, one can use the elliptical form of a gaussian beam [59]

$$\vec{E}_{\text{tw}}(\vec{x}) = E_0^{(tw)}\hat{\epsilon}_{\text{tw}}\frac{1}{\sqrt{q_{tw,x}(z)q_{tw,y}(z)}}e^{-ik_{\text{tw}}z - i\omega_{\text{tw}}t - ik_{\text{tw}}\left(\frac{x^2}{2q_{tw,x}(z)} + \frac{y^2}{2q_{tw,y}(z)}\right)} \tag{4.18}$$

$$\vec{E}_{\text{cav}}(\vec{x}) = E_0^{(cav)}\hat{\epsilon}_{\text{cav}}\frac{1}{q_{cav}(x)}\cos(k_{\text{cav}}x)e^{-ik_{\text{cav}}\frac{y^2+z^2}{2q_{cav}(x)}}\hat{a} \tag{4.19}$$

where $q_{i,j}$ is the complex beam parameter for beam i along axis j and ϵ_i is the polarization vector. We should note that the frames of reference for the standard form of the tweezer and cavity mode may not agree[5]. Let us assume that the nanoparticle is trapped close to the tweezer beam waist

---

[5] As is the case in our experiment where the polarization and alignment of the tweezer to the cavity is not perfect.

and set the displacement from this position to 0. We can then relate the coordinate system of the tweezer $\vec{x}_{\text{tw}}$ to that of the cavity $\vec{x}_{\text{cav}}$ through a rotation matrix $R(\theta, \phi)$ and some displacement $\vec{x}_{\text{tw,cav}}$. We can then write

$$
\begin{aligned}
\vec{x}_{\text{cav}} &= R(\theta,\phi)\vec{x}_{\text{tw}} + \vec{x}_{\text{tw,cav}} && (4.20)\\
&= \begin{pmatrix} \cos\theta & \sin\theta & 0 \\ -\sin\theta & \cos\theta & 0 \\ 0 & 0 & 1 \end{pmatrix} \begin{pmatrix} \cos\phi & 0 & \sin\phi \\ 0 & 1 & 0 \\ -\sin\phi & 0 & \cos\phi \end{pmatrix} \begin{pmatrix} \hat{x} \\ \hat{y} \\ \hat{z} \end{pmatrix} + \begin{pmatrix} x_0 \\ y_0 \\ z_0 \end{pmatrix} && (4.21)\\
&= \begin{pmatrix} \cos\theta\cos\phi\hat{x} + \sin\theta\hat{y} + \cos\theta\sin\phi\hat{z} + x_0 \\ -\sin\theta\cos\phi\hat{x} + \cos\theta\hat{y} - \sin\theta\sin\phi\hat{z} + y_0 \\ -\sin\phi\hat{x} + \cos\phi\hat{z} + z_0. \end{pmatrix} && (4.22)
\end{aligned}
$$

Usually, the tweezer potential is sufficiently strong to overcome any potential generated inside of our optical cavity. In this case, we are free to manipulate $\vec{x}_{\text{tw,cav}}$ and will almost always set $y_0 = z_0 = 0$ and change the particle's position along the standing wave x_0 to modify the coupling.[6] Returning to the coupling terms of our Hamiltonian, we will drop the terms oscillating at

---

[6] As will later be described, we will occasionally pull the particle away from the cavity axis, effectively setting $z_0 \neq 0$ which reduces the overall coupling strength as will be apparent as we follow through with the calculations.

the sum frequency $\omega_{\text{tw}} + \omega_{\text{cav}}$ and find that

$$\vec{E}_{\text{tw}}(\vec{x}) \cdot \vec{E}^{\dagger}_{\text{cav}}(\vec{x}) \approx E_0^{(tw)} E_0^{(cav)} \frac{1}{\sqrt{q_x^{(tw)}(\hat{z}) q_y^{(tw)}(\hat{z})} q^{(cav)}(\hat{x}_{\text{cav}})^*} \hat{\epsilon}_{\text{tw}} \cdot \hat{\epsilon}^*_{\text{cav}} \cos(k_{\text{cav}} \hat{x}_{\text{cav}})$$
$$\times e^{-ik_{\text{tw}}\hat{z} - i\omega_{\text{tw}}t - ik_{\text{tw}}\left(\frac{\hat{x}^2}{2q_x^{(tw)}(\hat{z})} + \frac{\hat{y}^2}{2q_y^{(tw)}(\hat{z})}\right) + ik_{\text{cav}}\frac{\hat{y}^2+\hat{z}^2}{2q^{(cav)}(\hat{x}_{\text{cav}})^*}} \hat{a}^{\dagger} \tag{4.23}$$

$$= E_0^{(tw)} E_0^{(cav)} \sqrt{z_{R,x}^{(tw)} z_{R,y}^{(tw)}} z_R^{(cav)} \hat{\epsilon}_{\text{tw}} \cdot \hat{\epsilon}^*_{\text{cav}}$$
$$\times \Bigg[\cos(k_{\text{cav}} x_0)$$
$$+ \left[\sin(k_{\text{cav}} x_0) k_{\text{cav}} - i \cos(k_{\text{cav}} x_0) \frac{1}{z_R^{(cav)}}\right] \cos\theta \cos\phi \hat{x}$$
$$+ \left[\sin(k_{\text{cav}} x_0) k_{\text{cav}} - i \cos(k_{\text{cav}} x_0) \frac{1}{z_R^{(cav)}}\right] \sin\theta \hat{y}$$
$$+ \left[\sin(k_{\text{cav}} x_0) k_{\text{cav}} - i \cos(k_{\text{cav}} x_0) \frac{1}{z_R^{(cav)}}\right] \cos\theta \sin\phi \hat{z}$$
$$+ i \cos(k_{\text{cav}} x_0) \left(\frac{1}{2z_{R,x}^{(tw)}} + \frac{1}{2z_{R,x}^{(tw)}} - k_{\text{tw}}\right) \hat{z}\Bigg] e^{-i\omega_{\text{tw}}t} \hat{a}^{\dagger} + \mathcal{O}(|\vec{x}|^2) \tag{4.24}$$

where z_R is the Rayleigh range of the gaussian mode. Generally, the chosen cavity geometries result in $k_{\text{cav}} >> \frac{1}{w_{\text{cav}}}$, where w_{cav} is the cavity waist. We can therefore safely ignore most of the terms proportional to $\frac{1}{z_R^{(cav)}}$. Additionally, the polarization of the tweezer field rotates the $x-$ and $y-$axes and therefore we can identify that $|\hat{\epsilon}_{\text{tw}} \cdot \hat{\epsilon}^*_{\text{cav}}| \approx \cos\theta$. We can switch to the rotating frame at the tweezer frequency to coincide with our previous work in which case the interaction Hamiltonian takes the form

$$\hat{H}_{CS} = -\hbar g_x(\hat{a} + \hat{a}^{\dagger}) \frac{\hat{x}}{x_{zpf}} - \hbar g_y(\hat{a} + \hat{a}^{\dagger}) \frac{\hat{y}}{y_{zpf}} - \hbar g_{z,1}(\hat{a} + \hat{a}^{\dagger}) \frac{\hat{z}}{z_{zpf}} - i\hbar g_{z,2}(\hat{a} - \hat{a}^{\dagger}) \frac{\hat{z}}{z_{zpf}} \tag{4.25}$$

where

$$g_x = E_d k_{\text{cav}} x_{zpf} \sin k_{\text{cav}} x_0 \cos\theta \cos\phi \tag{4.26}$$

$$g_y = E_d k_{\text{cav}} y_{zpf} \sin k_{\text{cav}} x_0 \sin\theta \tag{4.27}$$

$$g_{z,1} = E_d k_{\text{cav}} z_{zpf} \sin k_{\text{cav}} x_0 \cos\theta \sin\phi \tag{4.28}$$

$$g_{z,2} = E_d \left(\frac{1}{2z_{R,x}^{(tw)}} + \frac{1}{2z_{R,x}^{(tw)}} - k_{\text{tw}} \right) z_{zpf} \cos k_{\text{cav}} x_0 \tag{4.29}$$

$$E_d = \frac{1}{\sqrt{2\pi}\hbar} \frac{\alpha_{\text{ind}}}{\epsilon_0} \sqrt{\frac{P}{cW_xW_y} \frac{\hbar\omega_{\text{cav}}}{V_{\text{cav}}}} |\hat{\epsilon}_{\text{tw}} \cdot \hat{\epsilon}^*_{\text{cav}}| \tag{4.30}$$

and we note that there is an additional cavity drive term which is written in Equation 4.24 but dropped here as we want to focus on the optomechanical coupling. It acts the same as the cavity drive discussed in Chapter 3. Note that each of these coupling terms is of the form of our linear coupling in Section 4.1. One should note the differences in the coupling as a function of position and polarization relative to the dispersive case as explored in more detail in [36]. Additionally, when we discussed the dispersive coupling, we only considered the position along the cavity axis which, as we've seen here, can include some amount of all 3 of our mechanical oscillator's linear motions. Interestingly the $z-$motion is coupled to the amplitude quadrature of the optical mode. We will explore this in more detail in Chapter 7.

4.4 Heating Rates and Dissipation

We discussed heating rates in the context of the mechanical oscillator, trapped by an optical tweezer inside of a vacuum chamber. Now that the mechanical oscillator is coupled to an optical cavity, we have introduced another path for noise to couple to the oscillator.

4.4.1 Intensity Noise

Since the particle is now coupled to the cavity field, it can experience an additional intensity noise term. Previously, we had only considered if the trapping potential was fluctuating in which case the mechanical frequency is directly effected. In the case of the cavity, there are three different regimes of interest. The first is the low intracavity population limit in which case the perturbation to the trapping potential is minimal and can safely be ignored. The second is when the standing wave along the cavity constitutes the majority of the harmonic potential along that direction. In this case, the intensity noise of the laser couples exactly as it did before, just now for the cavity potential.

The third case is the intermediate regime whereby the tweezer and cavity potentials are comparable. In this case, it is important to distinguish between intensity noise contributing to the modulation of the trap frequency and intensity noise modulating the trap position. As we saw in Section 4.1, the coupling of the oscillator to the cavity can give rise to both a harmonic potential and a linear gradient term, depending on the position of the particle along the standing wave. Intensity noise at the harmonic potential modulates the trap frequency and we can then add the intensity noise of the cavity field to that of the tweezer.

At the intensity slope however, the particle experiences a force proportional to the gradient of the field, giving rise to a shift in the trap center proportional to the intensity of the cavity field. Intensity fluctuations at this point shake the trap in which case we get the heating rate from Subsection 2.3.3.

When operating in the dispersive regime, as we increase the coupling by increasing the intracavity field, the effects of the intensity noise in the cavity field can become comparable to that of the tweezer. In this dissertation however, all our dispersive coupling is weak and purely for diagnostics in which case we can safely ignore the impacts through this channel.

For coherent scattering, we must remember that the intracavity photon number scales like

$$|\alpha_0|^2 = \frac{E_d^2}{\left(\frac{\kappa}{2}\right)^2 + \Delta^2} \cos^2 k_{\text{cav}} x_0 \tag{4.31}$$

while $g_x^2 \propto \sin^2 k_{\mathrm{cav}} x_0$. Therefore, when we maximize the coupling we are minimizing the intracavity intensity and therefore we can again safely ignore this effect in most cases.

4.4.2 Finite Laser Linewidth and Laser Phase Noise

Laser phase and frequency noise can be thought of as two representations of the same fluctuations. We therefore consider only frequency noise and one can make an analogous argument for phase noise. Due to the cavity transfer function, frequency noise can couple to the mechanical oscillator through the transfer function of the optical cavity, transducing frequency noise to intensity noise.

This effect has been discussed at length [60] and we will proceed by examining how it plays a role in both dispersive and coherent scattering[7].

$$S_{FF}(\omega) \approx g^2 |\alpha_0|^2 |\chi_l(\omega) - \chi_l^*(-\omega)|^2 S_{\dot{\phi}\dot{\phi}}(\omega). \tag{4.32}$$

Note that it depends on the number of photons in the cavity and the detuning. Intuitively, if there are no photons then the fluctuations are purely quantum and the classical phase noise does not contribute to the motion of the particle. Similarly with the detuning, we expect the two systems to become uncoupled at resonance, again removing a channel for the phase noise to interact with the particle. This intensity noise then can modulate the trap frequency or the trap position as discussed before. As before, this effect is greatly suppressed when we maximize the coupling via coherent scattering and the intracavity field is approximately vacuum. Furthermore, the effect of it for our dispersively coupled diagnostics will also be suppressed as we use a resonant mode as will be discussed in Chapter 5. This has been a significant barrier to ground state cooling in previous iterations since the

---

[7] Note that the convention of the paper gives intensity noise in units of Hz compared with the RIN discussed earlier which has units of Hz^{-1}. We can unify the two by dividing by the appropriate frequency scale Ω_x^2.

expected bath occupation is

$$\bar{n}_{\dot{\phi}\dot{\phi}} = |\alpha_0|^2 \frac{|\Delta|}{\Omega_x} \frac{S_{\dot{\phi}\dot{\phi}}(\omega)}{\kappa} \tag{4.33}$$

which for the dispersive case is well above the groundstate for typical laser linewidths. Fortunately, for coherent scattering, we can minimize $|\alpha_0|^2$ and therefore the phase noise becomes irrelevant.

Part II

The Experimental Apparatus

Chapter 5

The Experimental Apparatus

The experimental apparatus has been the product of many generations of students work and has evolved into the iteration shown in Figure 5.1. The iteration described in this dissertation is composed of 5 main subsystems: laser preparation, the vacuum chamber, particle loading and the tweezer, the optical cavity, and detection. To understand the purpose of these subsystems we conside our general scientific procedure; we detect the motion of an nanoparticle position inside of an optical cavity while trapped in an optical tweezer.

5.1 Overview of the Apparatus

A system diagram can be found in Figure 5.2 which outlines the relationship between the different sections. The role then of the laser preparation is to generate enough optical power to trap the particle in the optical tweezer as well as optical modes for reference to the optical cavity and detection. The vacuum chamber is the environment in which the entire experiment takes place and needs to enable the loading procedure at near atmospheric pressure as well as our scientific goals in the ultra-high vacuum (UHV) regime. The particle loading is how we introduce the nanoparticle into the vacuum chamber in a targeted way to trap single nanoparticles in the optical tweezer. We need some way of referencing the optical tweezer to the optical cavity in position, polarization and frequency. Finally, we have many different types of detections which we use to observe the optical and mechanical components of our optomechanical system.

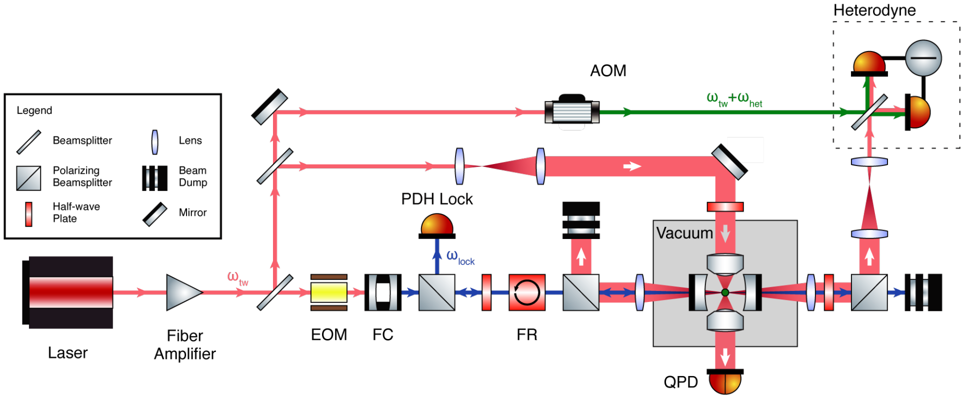

Figure 5.1: **The optical layout of the apparatus.** The laser source is split into three main paths: one for locking the laser to the optical cavity and two for detection. The locking, as described in more detail in Section 5.3.2 utilizes an electro-optic modulator (EOM) and filtering cavity (FC) to generate a single sideband. This is then referenced to the optical cavity and the reflection is redirected to an photodiode using a Faraday rotator (FR) and polarizing beamsplitter. These elements are used in conjunction with the locking electronics to create a Pound-Drever-Hall lock (PDH Lock). Most of the source laser is used to generate the optical tweezer which and this same tweezer light is detected by an optical setup equivalent to a quadrant photodiode (QPD). This is discussed in more deteail in Section 5.6.1. Finally, light exiting the cavity is mixed with a local oscillator to perform either a homodyne or, as shown here using an acouso-optic modulator (AOM) to shift the local oscillator frequency, heterodyne measurement. This cavity detection is discussed in Section 5.6.2

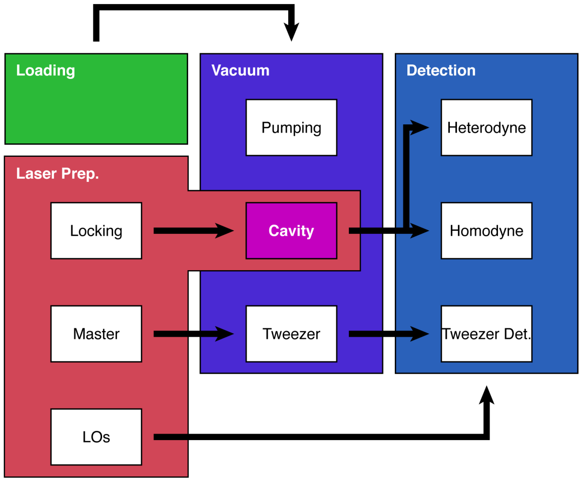

Figure 5.2: **A block diagram of the components of the apparatus.** The relationships between the different sections of the apparatus are outlined.

5.2 Particle Loading

In some sense the starting point of the experiment, the particle loading has seen great technological improvement in recent years. Particles have been loaded via an aerosol [61], piezoelectric vibrational platforms [62], and laser induced acoustic desorption (LIAD) [63–65]. Arguably the most technologically simple, we utilize the aerosol method for historical reasons.

This method entails keeping the nanoparticles in a liquid suspension and using a device, in our case a so-called nebulizer, to aerosolize this suspension which is sprayed into the vacuum chamber. The droplets, containing the nanoparticles, disperse and explore the vacuum chamber, eventually passing through the optical tweezer and probabilistically being trapped. This is akin to loading via an atomic dispenser [66] except the number of particles interacting with the trap cross-section is significantly lower leading to individual trapping events instead of a trapped gas buildup in a magneto-optical trap for instance.

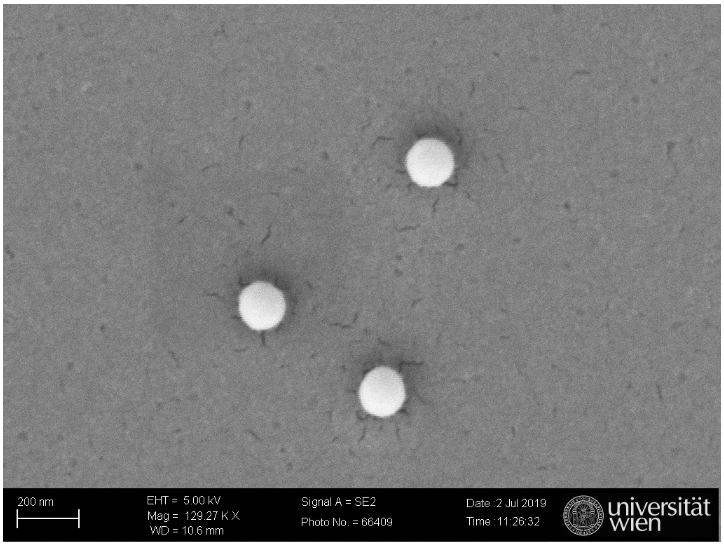

Figure 5.3: **Scanning electron microscope image of three 70nm radius silica nanospheres.**

5.2.1 The Nanoparticle

We use silica nanospheres purchased from Microparticles GmbH for all of the experiments described in this dissertation. We use silica as the material due to its technological background allowing for consistent particles to be manufactured, as well as the thorough study of its optical characteristics in, for instance, optical fibers [67]. It has been shown to have a small optical absorption coefficient at telecom wavelengths, allowing the use of another mature industry.

The properties of these nanospheres are summarized in Table 5.1. The

Property	Value
Density[8]	1850kg/m^3
Radius[9]	71.5 ± 2nm
Index of Refraction (at 1064nm)[68]	~ 1.5
Absorption Index (at 1064nm)[68]	~ 10^{-7}

Table 5.1: **Properties of typical silica nanoparticles.**

nanospheres come in a water suspension with a concentration of 1.8×10^{10} particles per microliter[10]. We can directly verify the radii of the nanosphers by letting a droplet dry on a glass slide and imaging the resulting cluster in an scanning electron microscope (SEM) as can be seen in Figure 5.3. Due to the size of the particles relative to the necessary conductive gold coating, measuring the radius using individual nanosphere images leads to a large uncertainty. Instead, we use fact that the attractive Van der Waals forces between the nanoparticles tends to lead them into a tight-packing structure. In this structure, the distance between neighbouring nanoparticles should be twice the radius even with the additional gold coating, allowing a more precise and accurate verification of the manufacturer's parameters.

The mass of a given particle can be characterized in situ as detailed in [36]. Using the relative amplitudes of the linear and quadratic couplings, one can deduce the mass of the particle in a calibration-free measurement. This has been used, in conjunction with the radius measurement, to verify the manufacturer's specified density.

5.2.2 Aerosolization and the Nebulizer

The aforementioned clustering behaviour of the nanospheres is undesired when it comes to loading. We want to avoid loading a cluster of particles and the aerosolization is therefore designed to maximize the probability of having at most a single nanoparticle in each drop. We use the Omron MicroAIR U22 nebulizer[11] which has a droplet size of 2.1μm. We will typically further dilute the particle suspension with isopropanol at a ratio of 1:1000 by volume which results in the average aerosol droplet containing 0.7 nanoparticles. This results in the occasional trapping of an empty isopropanol droplet which

---

[8] The density is significantly lower than that of other silica materials ranging from 2000–2600kg/m^3. This is due to a vesicular texture believed to be a result of the manufacturing process. This density has been experimentally confirmed.

[9] Occasionally we will use a larger particles with a radius of 104 ± 2nm as measured during our work "Dry launching of silica nanoparticles in vacuum"[62]. In this case, it will be noted in the text.

[10] This is quoted as 5% of the weight is nanoparticles

[11] Some of the later work was done with the Omron MicroAIR U100 which has a droplet size of 2.25μm due to damage and subsequent inability to repurchase the U22.

can be detected[12] and removed from the trap.

In an attempt to further reduce the probability of clusters, we use a vortex mixer to agitate the water suspension before we take our sample for dilution. Once the sample has been added to the isopropanol we again use the vortex mixer to thoroughly incorporate the two liquids. The efficacy these steps is still unknown but the entire procedure produces the desired results.

The nebulization rate is stated to be ~ 5μl/s giving off approximately 10^8 droplets every second. We have observed a decrease in the nebulization rate indicating that this may be a gross overestimate for nominal use. It is unknown for how long the droplets stay aerosolized nor if the presence of the nanoparticles impacts the aerosolization.

5.2.3 Loading

Loading is primarily done via differential pumping. The nebulizer is kept in a small air-tight enclosure as it produces the aerosol. It is then connected to the vacuum chamber, which is held below atmospheric pressure, via a plastic tube. When the valve between the two sections is opened, the pressure differential causes the aerosol to be transported, along with the gas inside the nebulizer chamber, into the vacuum chamber. An additional tube connects the nebulizer chamber to either a nitrogen tank or filtered air to provide a constant flow into the chamber when the valve is open. The location of this inlet tube inside the nebulizer chamber relative to the outlet tube impacts the efficiency of the procedure as the flow of the aerosol can be manipulated. The current apparatus is shown in Figure 5.4. Opening and closing the valve between the two chambers is done manually and therefore introduces a large amount of variability.

We know that some portion of the aerosol sticks to the walls of the nebulizer, tubing or vacuum chamber because we can continue loading particles of a given size even after we switch the particle size in the nebulizer solution.

---

[12] When a particle is trapped inside of the optical tweezer, we evacuate the chamber until 10^{-2}mbar. Isopropanol or water will evaporate rapidly at these pressures, leaving a clean particle if there is one.

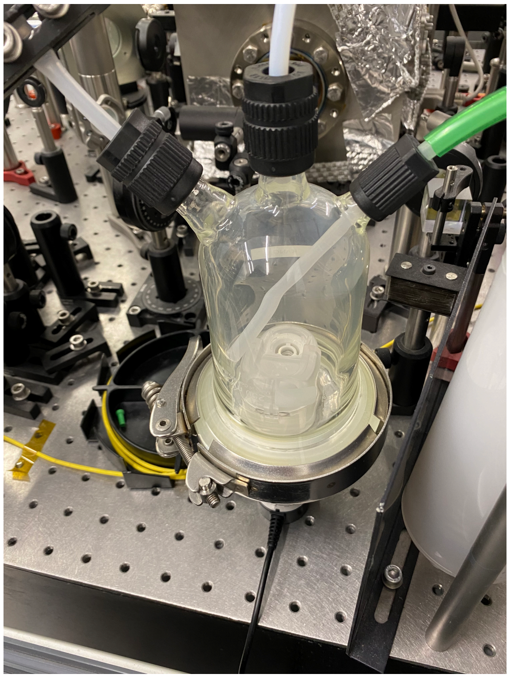

Figure 5.4: **The loading section of the experiment.** The nebulizer produces an aerosol from the nanoparticle suspension. This fills the preparatory chamber before the gate valve to the science chamber is opened and the pressure differential pulls the aerosol into the main chamber. A second tube allows filtered air or nitrogen to be sucked into the preparatory chamber to maintain the crossflow.

This effect diminishes after a subsequent spraying events as the droplets that were likely to have been pulled from the surfaces are depleted.

The aerosol quickly disperses throughout the vacuum chamber and droplets can be seen passing in the vicinity of the tweezer for tens of minutes. If a particle has not been trapped after this time we usually evacuate the vacuum chamber and create a new aerosol.

5.2.4 Limitations and Future Considerations

This apparatus is extremely cheap and simple to operate which allows for fast prototyping of new experimental setups. This comes at the cost of reliability and cleanliness of the vacuum chamber. As discussed before, this scheme is a probabilistic loading process in which the individual events are visible on a human timescale as opposed to atomic loading via a dispenser or effusive source. This means that the timescale for loading a particle can be short, oftentimes after a single spraying event (~ 30min), or it can be inconveniently long. Occasionally, multiple days have gone by without being able to trap a particle. During this time, diagnostics are difficult to perform as all visual indicators are constant.

Additionally, this loading introduces water, isopropanol and gas into the vacuum chamber, none of which would ideally be there if we want to work in UHV. This ”wet” loading slowly degrades the cleanliness of the vacuum chamber, increasing the outgassing rate and limiting the base pressure of the system. Furthermore, the aerosol droplets can stick to surfaces inside the chamber which impact the performance of optics. It is unknown how this effects the optical tweezer microscope objective but if the cavity is inside the vacuum chamber during a spraying event, it can increase the scattering losses from the mirrors. This necessitates the removal of the cavity from the vacuum chamber during loading as will be discussed in Section 5.5.1.

As such, a ”dry” loading scheme would certainly be a desired upgrade, especially if it can be performed at low pressures. This would increase the repetition rate of high cooperativity experiments as it currently takes many hours to pump from atmospheric pressure down below 10^{-6}mbar. At the moment, the base pressure of the vacuum chamber is such that we are always limited by collisions with gas molecules instead of radiation pressure and an improvement in the cleanliness of the environment would allow us to reach this regime.

An additional consideration for future experiments is the option to switch either laser frequency or material. At the time of inception for this experiment, fabrication of silicon nanospheres was a developing technology. However, now commercial manufacturers can reliably produce usable nanospheres. The improved optical properties that coincide with switching to 1550nm along with the decrease in absorption index (down to $< 10^{-12}$ for silicon at 1550nm[69]) suggest the technological benefits may outweigh the setbacks associated with adopting a new infrastructure.

5.3 Laser Preparation

Since we are not probing atomic transitions, the restrictions on the laser setup are greatly reduced when compared with a typical AMO experiment. The only frequency reference we need to compare to is that of the optical cavity since the nanoparticles have no strong absorption lines. The absence of internal transitions simplifies the number of frequencies we need to tune. Nonetheless, we need to generate enough light for trapping, locking and detection and properly interface this with the experiment. The entire laser preparation and distribution is outlined in Figure 5.1.

5.3.1 Master Laser

The laser system starts with the light out of a Coherent 1064nm 2W Mephisto laser[13]. While our experiment can operate using the output of the Mephisto as the sole source, we have opted to use it as a master laser for a fiber amplifier. We have used both the Keopsys 1064nm 10W CW Ytterbium Fiber Amplifier and the Azurlight Systems 1064nm 10W Fiber Amplifier to increase the amount of available power. The master and amplifiers were chosen to minimize the intensity and phase noise while providing adequate power for the entire experiment. The Mephisto demonstrates its best noise performance when run at full current so we couple the excess light into a fiber which can be used for diagnostics. Conversely, the degradation of our optical components is highest at full amplifier power so we typically run it at ~ 4W instead of the full 10W.

We characterized the residual intensity noise (RIN) of the master laser system which can be seen in Figure 5.5. These values of the (RIN) were used to compute the estimate for the intensity noise heating in Subsection 2.3.2.

---

[13] This laser has degraded over time and has a maximum output power of only 1.6W now.

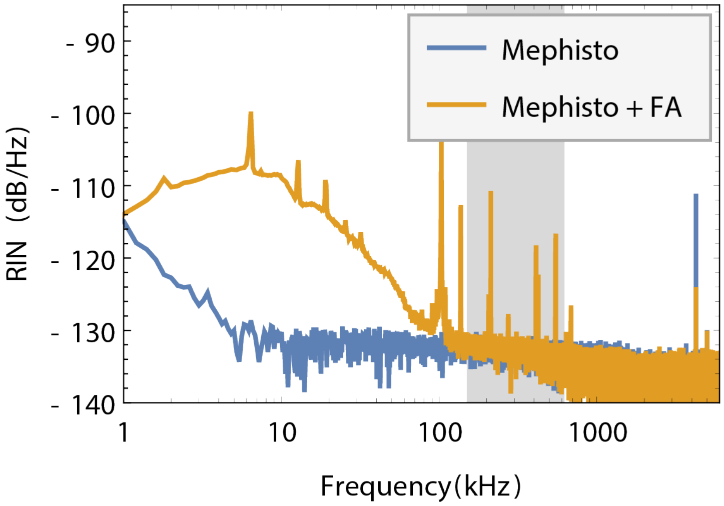

Figure 5.5: **The measured residual intensity noise (RIN) of the master laser setup.** As discussed in Subsection 2.3.2, laser intensity noise gives rise to parametric heating. To characterize this process we measure the RIN of the Mephisto (blue) and the light after the fiber amplifier (Keopsys) used for trapping (orange). We are interested in the shaded gray region in which case both spectra largely overlap. However, the additional noise outside of this region is still technically problematic which, in part, lead to the switch to the Azurlight fiber amplifier towards the end of this research.

A thorough characterization of the laser system has been performed[36] but one additional property to note is the mode-hop free range of the laser. As outlined in Figure 5.6, the laser cavity itself has multiple longitudinal modes which interact with the gain medium to lase. Depending on the position of the gain profile relative to these modes, the laser can run in a single mode or mode-hopping configuration whereby neighbouring cavity modes compete for gain. Due to the locking scheme discussed in the subsequent subsection, the lifetime of the lock is limited by the mode-hop free range of the laser as a mode-hop will change the laser frequency by ~ 5GHz which is clearly outside of the lock bandwidth. Figure 5.7 shows the tuning performance of the Mephisto that we have independently verified. Additionally, operating near a mode hop can degrade the noise performance of the laser and is therefore undesirable.

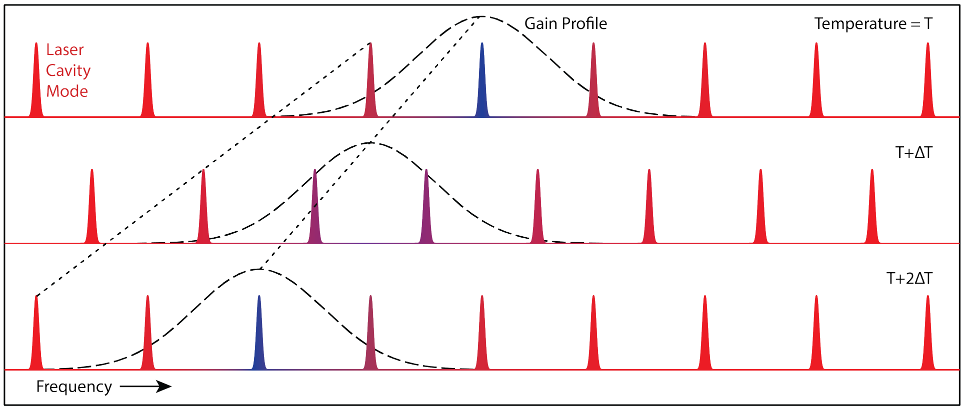

Figure 5.6: **Diagram of the mode hopping mechanism.** As the temperature increases, the cavity modes and the gain profile shift at different rates. This means that by tuning the temperature, one can change which cavity mode is supported by the gain medium. However, when the gain profile amplifies multiple modes then the laser cycles between stimulated emission from each mode, hopping back and forth. These cavity modes can be far apart in frequency space causing large jumps in the lasing frequency.

5.3.2 Cavity Lock

The first beam to be derived from the master is the cavity lock beam. Since our cavity is not stabilized, drifts in the cavity length due to thermal effects cause the free-spectral range to change and therefore the detuning of the master relative to the cavity. To compensate for these changes, we lock the laser to the cavity instead of the cavity to some other reference. This comes with the advantage of a significantly more simple cavity holder and alignment at the cost of decreased lock lifetime due to the finite tuning range. More specifically, the mode hop free range corresponds to ~ 7.5GHz[14] of tunable range. If the laser is locked to the cavity at the time of a mode hop, this will result in the loss of lock.

We use series of cascaded locks to bypass the limited bandwidth of our individual feedback servos. To maximize the range, we use the laser temperature to apply near-DC feedback for slow drifts which, as previously

---

[14] This laser has the standard tuning range but an extended tuning range model exists that would increase the mode-hope-free range from ~ 2.5°C to 4 – 5°C.

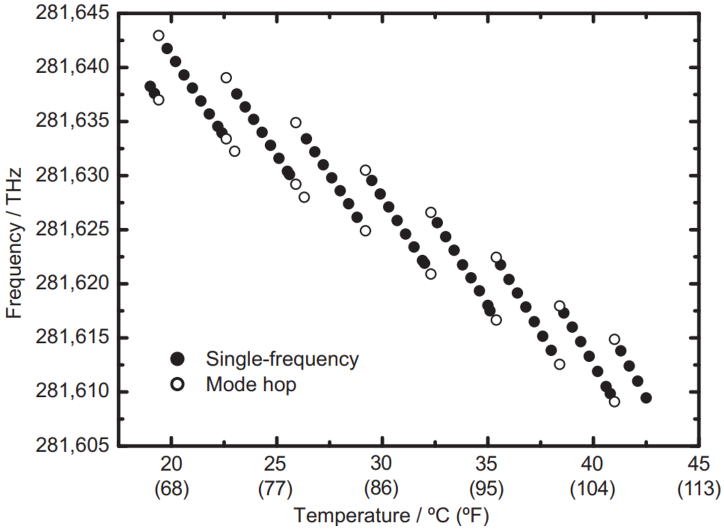

Figure 5.7: **The tuning performance of the 1064nm 2W Mephisto used as the master laser in our system.** The mode-hop-free range is roughly 2.5°C. This figure is taken from the Mephisto data sheet.

mentioned, can then compensate many gigahertz which would be outside the range of all but a few electro-optical modulators (EOMs)[15]. For faster feedback, we utilize the piezoelectric transducer inside of the laser which stresses the Nd:YAG crystal, modifying the gain structure and therefore lasing frequency. The piezo element has a bandwidth on the order of 1kHz. One can additionally use an AOM or EOM for a final fast feedback stage but this is unnecessary for the work discussed in this dissertation.

To lock to the cavity we must interrogate it with the laser field. Since the mechanical oscillator will couple to the intracavity field it is important that we forgo any unnecessary coupling of noise. The locking light would be dispersively coupled to the particle and we can use the results of Section 4.4. As we've seen, one way to do so is to use a resonant drive as our locking mode. Additionally, we want the drive to be weak so as to be a negligible perturbation to the trapping field. Lastly, for detection purposes, it is useful to use a different cavity mode than our coherent scattering mode so that we

---

[15] An additional drawback to using an EOM is the insertion loss. One could potentially increase the tuning range with specific EOMs beyond the mode-hop-free range though.

can frequency filter the two different components.

These criteria result in the locking scheme is shown in Figure 5.1. We use a fiber EOM[16] to shift part of the master laser by $\omega_{\mathrm{Lock}} \sim \omega_{\mathrm{FSR}} \approx 14$GHz. To eliminate the carrier and unwanted second sideband, this light is passed through a homebuilt filtering cavity[17]. This filtering cavity is side-of-fringe locked to the desired sideband. The transmitted light is then locked to the optical cavity via a Pound-Drever-Hall (PDH) lock which applies feedback through the Mephisto's piezo element. For the PDH lock, a 6MHz dither is applied by the aforementioned EOM and the frequency is chosen such that it is also transmitted by the filtering cavity. The feedback signal for this lock is used as the error signal of a slow lock using the laser temperature to correct for slow drifts. Both the filtering cavity's side-of-fringe lock and the PDH lock are controlled by a Toptica PID 110 while the slow thermal lock is controlled by the in-built PID on a Zurich Instruments HF2LI Lock-in Amplifier[18].

When everything is locked, the light, which was split before the EOM, is detuned from the locking mode of the cavity by ω_{lock}. By setting $\omega_{\mathrm{lock}} = \omega_{\mathrm{FSR}}$ this light would be resonant with the next cavity mode and by tuning ω_{lock} we can therefore tune the detuning of the laser relative to this mode. The consequence of this scheme is the timescale on which the detuning can be changed. Changing ω_{lock} detunes the locking laser from the locking mode, in which case the various locks react to compensate with the laser frequency. Changing this too fast would result in losing one of the locks. In principle, the detuning can be changed by up to 10MHz in a single step but we usually divide this into multiple steps, changing roughly 100kHz per second. This way we can monitor the lock for any instability as we modify the detuning and make the necessary adjustments to compensate.

---

[16] The PM-0K5-20-PFA-PFA-106-LV-UL model from EOSPACE.

[17] The filtering cavity is a simple Fabry-Perot cavity with a piezo element placed between the cavity mirrors to modify the cavity length for locking. The cavity has a linewidth of $\kappa_{\mathrm{FC}} \approx 2\pi \times 80$MHz.

[18] We use the HF2LI over the PID 110 to additionally tune the offset of the output signal. This is because we can finely tune the laser temperature when looking for an initial locking signal as the manual temperature control of the Mephisto is sensitive and difficult to set accurately. It can also be used to record the error signal through the provided software.

An additional limitation is the locking paradigm which was chosen for its simplicity. As previously mentioned, since the laser is locked to the cavity and the laser has a finite mode hop free range, this sets a limit on how far the laser can follow the cavity once locked. If the laser comes unlocked when the vacuum chamber is at low pressures the optical damping is removed and the particle will heat out of the trap. It is therefore of the utmost importance that the laser remains locked to the cavity for pressures below 10^{-2}mbar. To quantify the amount of expansion this would allow for, we first have to recall that the cavity mode we are locked to $\nu_q = q\nu_{\mathrm{FSR}} = q\frac{c}{2L}$ corresponds roughly to our laser frequency of 282THz. Changes in the cavity length will then impact the FSR and this effect is amplified by the mode number. As we will see, the cavity length is $L = 1.07$cm which has an associated free spectral range of $\nu_{\mathrm{FSR}} = \frac{c}{2L} = 14.0192$GHz. This means that $q \approx 20000$. The mode-hop-free range sets a maximum change in the cavity length of ~ 265nm. The cavity is made out of aluminum which means it has a thermal expansion of roughly 20μm/°C which means we can tolerate roughly 1°C of change in the holder temperature in optimal conditions. Given variability in room temperature and other heating mechanisms, this can set a finite locking duration which has consequences for experiments we want to perform as we will see in Chapter 6. The pressure also changes the effective cavity length, just to a much smaller degree. This discussion will be continued in Subsection 5.4.1 when we consider vacuum pumpdowns.

5.3.3 Optical Tweezer

The laser light derived from the master laser is focused by our microscope objective[19] which is placed inside of the vacuum chamber, as shown in Figure 5.1. Typical trap parameters are shown in Table 5.2. The microscope

---

[19] The microscope objective is an Olympus LMPL 100x IR which has a numerical aperture NA = 0.8, a focal length of $f = 1.8$mm and a working distance of $WD = 3.4$mm. One should note that although we overfill the objective, the effective numerical aperture is significantly smaller than the specified NA.

[20] As mentioned previously, radiation pressure will displace the particle from the beam waist, reducing the experienced trapping potential.

Property	Value
Impinging Power	400mW
$(\Omega_x, \quad \Omega_y, \quad \Omega_z)$	$(305, 275, 80)$ kHz
$(W_x, \quad W_y, \quad z_R)$	$(0.67, 0.77, 1.7)\mu$m
Effective NA	0.56
Filling Factor	0.7

Table 5.2: **Typical optical tweezer parameters for a silica nanoparticle with a radius of 73nm[20].** Tweezer beam parameters are calculated using Appendix B and the measured mechanical frequencies.

objective is mounted on a triaxial nanopositioner[21] to align the tweezer waist relative to the optical cavity as will be discussed shortly.

In principle, the laser for the optical tweezer can be directly taken from the master however we have chosen to pass it through a double-pass AOM[22] running at 80MHz to enable us to quickly switch the detuning, bypassing the earlier discussed limited tuning speed. This was driven by an arbitrary wave generator[23] to enable fast frequency changes. Since we use a 10W amplifier as the main laser source, we have additional headroom to increase the trapping frequencies further.

To increase the usability and day-to-day stability of the setup, the tweezer comes from a single-mode optical fiber. Unfortunately, this fiber was not polarization maintaining and the polarization of the tweezer slowly drifted on the timescale of weeks. This was sufficient for our purposes as a set of waveplates before the beam enters the vacuum chamber ensured we could generate any polarization. For future experiments this would be a simple improvement to make.

---

[21] We use a Mechonics MX35 positioner with a piezo electric inertial drive in conjunction with a Mechonics CF.030.0003 driver to reach a step size of approximately 8nm. This stage has a slip-stick motion with ”jumps” in the motion every 64 steps at which point the stage moves by an uncalibrated amount.

[22] IntraAction ATM-804DA6M

[23] Tektronix AFG3152C

5.3.4 Local Oscillators

The final component of the laser preparation is that of the local oscillators for detection. As we will see, we need to derive local oscillators for both heterodyne and homodyne detections.

For the locking-mode homodyne, a beamsplitter after the filtering cavity splits off some light. Since the signal beam then follows an alternative path which transmits through the optical cavity, we need to compensate for any differential phase drifts between the two arms. This is done by modulating the path length of the local oscillator. To realize this, one of the mirrors in the local oscillator beam path is mounted on a piezo. The phase of the local oscillator is then locked to that of the signal using the DC voltage of the detector and the previously mentioned Toptica PID.

Heterodyne detection does not require this differential phase stability and instead the technical requirement is generating the frequency difference between the local oscillator and signal. Restrictions on this frequency difference come from the intensity noise spectra, detector bandwidth and sampling frequency.

Intensity noise impacts both the physics we are interested in measuring and the way in which we measure it. We can suppress it with clever detection schemes but it is useful to additionally choose a frequency range in which the intensity noise is minimal and ideally flat. Given the intensity noise spectra for our laser shown in Figure 5.5, our heterodyne frequency would ideally be at least 2MHz.

Our detector bandwidth is 70MHz and the maximum sampling frequency of our DAQ[24] is 60MHz. To then sit well below these limits, the heterodyne frequency has been set to ~ 10MHz.

We achieve this frequency difference using two AOMs[25] in series, one that shifts the frequency up and the other that shifts it down. We have chosen low phase-noise frequency generators[26] to limit the impact of the

---

[24] Picoscope 5442D

[25] AA Opto-Electronic MT200-B100A0,5-1064

[26] We used a Keysight E8257D with an Agilent Technologies E8257D since they each had one channel and later switched to a four channel AnaPico APMS06G-4.

classical noise of the local oscillator on the detection.

5.4 The Vacuum System

The optomechanical aspect of the experiment is housed inside of a vacuum chamber to allow us to control the interaction between the nanoparticle and its surrounding atmosphere. This has additional benefits of providing a clean environment for the optical cavity to reduce the slow deterioration of the cavity linewidth as the losses from scatter on the mirror surfaces increases.

Therefore, the constraints on the vacuum system are that it must reach pressures where the quantum behaviour of the particle is dominant ($P \sim 10^{-6}$mbar) and allow us to do so from room pressure due to the spray of the particle aerosol for loading. A further constraint is that we must be able to insert and remove the optical cavity from the vacuum chamber to protect it during loading as the deposition of the aerosol on the cavity mirrors will cause additional losses. This is discussed in more detail in [62, 36].

The vacuum setup to accommodate these requirements is shown in Figure 5.8. The included quick-access flange is large enough that one can manually insert and remove the cavity. All of the windows are standard flat windows except for the one window on the detection side to avoid back reflections coupling to the cavity. Most of the vacuum system remains unchanged from previous iterations [36]. The main science chamber is a homebuilt cube with ports on all main faces. The quick access window sits on the opposite port from the tweezer entry port. A CF63 cross on top of the chamber connects it to the combined Pirani-Cathode pressure gauge as well as all of the pumping. Additionally, the connection to the nebulizer for loading is done through a gate valve.

5.4.1 Pumping

Since the vacuum system needs to load at pressures near ambient conditions and subsequently pump down to pressures of 10^{-6}mbar, the pumping system consists of three main parts: a leakage port for venting the chamber, a high

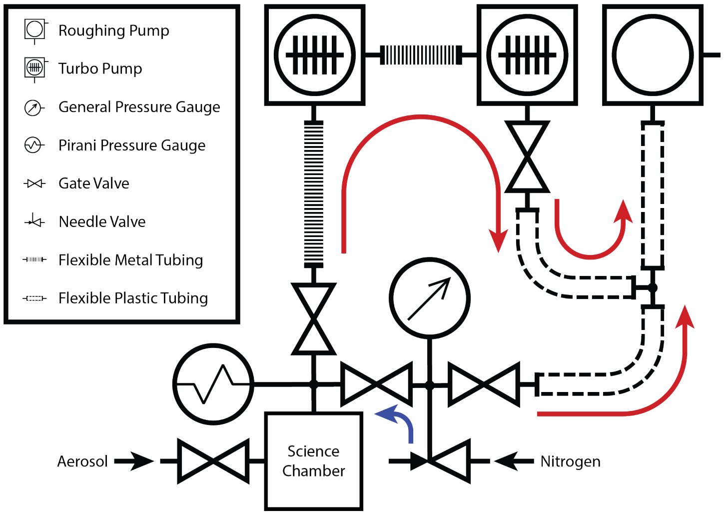

Figure 5.8: **A schematic of the vacuum system used in this work.**

pressure pump and a low pressure pump.

Since we need to equilibriate the internal pressure of the chamber with the lab conditions in order to safely open the quick access door for adding or removing the optical cavity, a connection is included, by way of a needle valve, to leak in filtered air or nitrogen to maintain the cleanliness of the chamber. A pressure gauge is kept at this point to provide high pressure data outside of the range of the Pirani-Cathode. The gate valve from the main chamber to this pumping section allows us to be less stringent on the vacuum level of this connection. Another gate valve seals off the scroll pump from this leakage connection so we don't pump in our venting gas.

The scroll pump (Edwards nXDS6i) acts both as a backing pump for the low pressure pumping stage and as a high pressure pump of the science chamber. The combination of gate valves allows for all pressure requirements to be satisfied. With this pump we can quickly reach ~ 10^{-2}mbar although its performance does not reach its specified value despite multiple rounds of maintenance.

For the low pressure pumping section we have chained turbo pumps to achieve the best pumpdown performance. The scroll pump acts as the backing pump for a small turbo pump which then acts as the backing pump for a larger turbo pump (Edwards nEXT300D). This was done because of the insufficient performance of the scroll pump which decreases the pumping speed of the large turbo pump. As we will see, the pumping speed is important for the success of this experiment. The turbo pump is then connected to a large CF63 metal bellows to act as a damping of vibrations however spin up of the turbo pump is still detrimental to the cavity lock. As such, we keep the pump running at full speed and seal off the bellows with a gate valve and open the valve when we want to pump. Additionally, the gate valve has an audible acoustic response when initially opening which can cause an undesirable impulse in our lock. We therefore keep the gate valve open just past this point but still closed enough that the pumping rate is negligible when compared to outgassing processes.

The pressure of the science chamber was recorded during a typical pumpdown and is shown in Figure 5.9. To reach pressures where the cooperativity $C > 1$ takes approximately 10 hours. The quick access door and improperly clean vibration absorbing viton inside of the chamber likely contribute to the duration of this procedure. More dominant however is the ”dirty” loading technique as spraying of a liquid, especially one containing water, is terrible for vacuum cleanliness. We have observed that the pumpdown is slower by up to ~ 1.5 times right after spraying the nanoparticle aeorosol into the chamber. Altogether, this can cause competition between the reachable pressures in the chamber and lock lifetime as the cavity length drifts during the pumpdown. Due to the evacuation of the chamber, it is hypothesized that the cooling rate of the cavity holder is decreased and as it continuously absorbs scattered light from the tweezer, it is not in thermal equilibrium during the pumpdown. It almost always causes the laser temperature to increase as the locks try to follow it. The mode-hop free range then sets a time limit on the lock lifetime. The resulting timescale was dependent on what time of day the measurement was performed as the ambient lab conditions also fluctuated due to the insufficient stability set by the air-conditioning system. We found starting the measurement in the evening and measuring in the early morning meant the temperature would stabilize and even start decreasing towards the end of the pumpdown as is the case in Figure 5.9.

For cases where the lock would near the end of its range before the desired pressure was reached, we could slowly close the gate valve to the turbo pumping stage and allow the outgassing to raise the pressure inside the science chamber. Once the pressure increase levelled off we could open the needle valve and vent the chamber to our nominal pressure where we could reset the lock and start the pumpdown again. Subsequent pumpdowns would be faster by up to ~ 1.5 times.

5.4.2 Future Considerations

The competition between pumping speed and lock lifetime limits the pressures reachable by the apparatus. Additionally, the probability of measurement success decreases as the required pressure decreases as other factors in the environment can cause the lock to decrease. As such, for future quantum experiments it is imperative that such an apparatus switches to a ”clean” loading technique where the sanctity of the chamber remains uncontaminated. Previous success in the group has come in the form of piezo [62] and hollow-core loading in UHV [70, 71] and recent advances in light induced acoustic desorption (LIAD) [65] are also promising.

5.5 The Optical Cavity

The optical cavity consists of two identical mirrors with a high reflection coating[27] in a near-confocal configuration $R \approx L$. All of the cavity parameters can be found in Table 5.3. Note that our optical cavity is double sided since we operate with identical mirrors. Additionally, to fit the mirrors with the microscope objective, they were cut from their circular shape to that of a strip as shown in Figure 5.10. This asymmetry breaks the degeneracy of the polarization modes leaving a separation of 160kHz between the horizon-

---

[27] Layertec

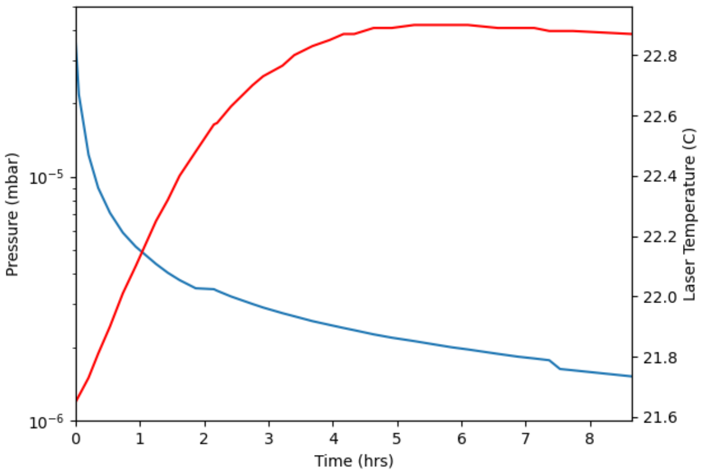

Figure 5.9: **A record of the science chamber pressure and laser temperature during a pumpdown from a nominal pressure of 4mbar to 10^{-6}mbar.** Note that, during the entire duration of the graph, the low pressure pumping stage is pumping at full capacity. The chamber pressure (blue) takes up to 10 hours to reach base pressures between $10^{-7} - 10^{-6}$mbar. The low pumping speed and high base pressure is likely due to high outgassing of the chamber. The frequent spraying of a liquid into the chamber is a dominant contribution and we have correlated the time between a loading event with pump speed. Additionally, over this time, the temperature of the laser can change by multiple degrees Celsius as it follows the expansion of the optical cavity. Varying ambient temperatures as well as reducing heat dissipation through background gas collisions can play a role in this heating process. It was therefore important to operate at night when the cooling of the room was highest to ensure the laser stayed locked as long as possible.

tal and vertical polarization modes[28]. A thorough description of the cavity construction has been previously given [72, 36].

---

[28] Since the mirrors are cut and positioned such that the mirror asymmetry aligns with the vertical and horizontal planes of the lab frame, polarization of the cavity modes naturally aligned to that of the lab frame. For cylindrically symmetry mirrors that may have induced birefringence due to stresses from clamping or gluing, this may not be the case and extra care needs to be take to align the cavity modes with the lab frame for simple use.

Property	Value
Mirror Radius of Curvature (RoC)	10mm
Mirror Dimensions	6.35mm×4mm
Mirror Transmission ($\mathcal{T}$)	20ppm
Mirror Losses	30ppm
Cavity Length (L)	10.7mm
Cavity Linewidth (κ)	$2\pi \times (193 \pm 1)$kHz
Cavity Finesse ($\mathcal{F}$)	73000
Free Spectral Range (ω_{FSR})	$\sim 2\pi \times 14$GHz
Cavity Waist ($W_0^{(\text{cav})}$)	$\sim 41\mu$m
Cavity Rayleigh Range ($z_R^{(\text{cav})}$)	~ 5mm

Table 5.3: **Properties of the optical cavity used in this experiment.**

5.5.1 Cavity Insertion

As previously mentioned, the cleanliness of the mirrors would decrease if it was left in the vacuum chamber during our "dirty" nanoparticle loading process. To overcome this problem, the cavity and vacuum chamber were designed for manual removal of the cavity during the loading process and subsequent reintroduction of the cavity into the chamber after a particle has been trapped. This is done by venting the chamber with a clean gas[29] and opening the quick access door. The cavity is clamped to its holder by an aluminum plate which is then screwed to the base. This process is surprisingly exceptionally stable with no discernible change to the cavity mode coupling over time. To reduce the likelyhood of a trapped particle being lost during the insertion of the cavity, the tweezer focus is moved away from the cavity by roughly $5W_0^{(\text{cav})}$ such that any coupling of scattered light is negligible and the gas damping at STP dominates[30].

---

[29] This was historically done with a filtered air system but for this work we largely used a nitrogen tank so that the chamber could be overpressurized to reduce further contamination.

[30] This becomes increasingly important as the particle size increases as both the coupling increases and the mechanical frequency decreases. We have been able to trap up to 127nm radius particles however they have always been lost when the cavity has been put in. This is another reason to move to a different loading setup.

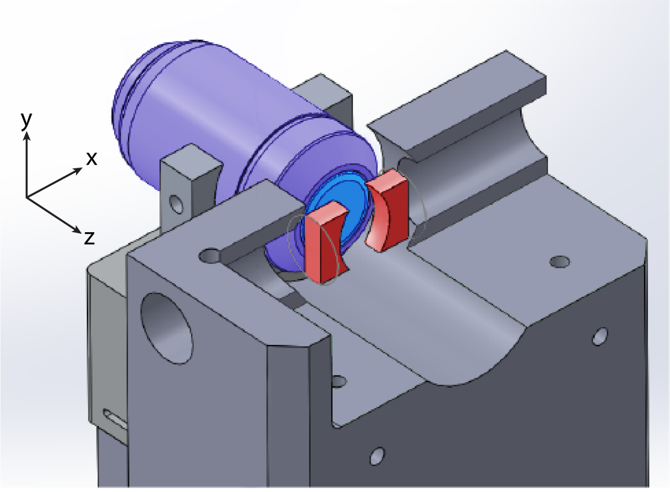

Figure 5.10: **An overview of the cavity (red) in relation to the microscope objective of the tweezer (blue).** The mounting of the cavity is omitted to not obstruct the view. Light is coupled into and out of the cavity along the $x-$axis through the holes drilled into the base. The tweezer light propagating along the $z-$axis is collected by a lens (NA= 0.2) that is not shown here.

5.5.2 Noise and Drifts

Since a simple design approach was taken, the cavity is subject to long term drifts and acoustic frequency noise. The long term drifts due to thermal and atmospheric changes were already discussed in Subsections 5.3.2 and 5.4.1. An important complication is relative positional instability of the tweezer relative to the optical cavity. Since they are not housed in a monolithic mount, they are susceptible to low-frequency vibrations which can slowly vary the position of the particle along the cavity standing wave. Indeed we have seen motion in the range of 50Hz couple to the particle motion resulting in movement on the order of $\lambda/10$. The long metal bellows running to the turbo pumps exacerbated the vibrations. To counteract this, we applied clay and foam to the bellows at specific locations to damp its vibrations shown in Figure 5.11. This lead to a reduction in the positional drift to $\lambda/1000$ shown in Figure 5.12.

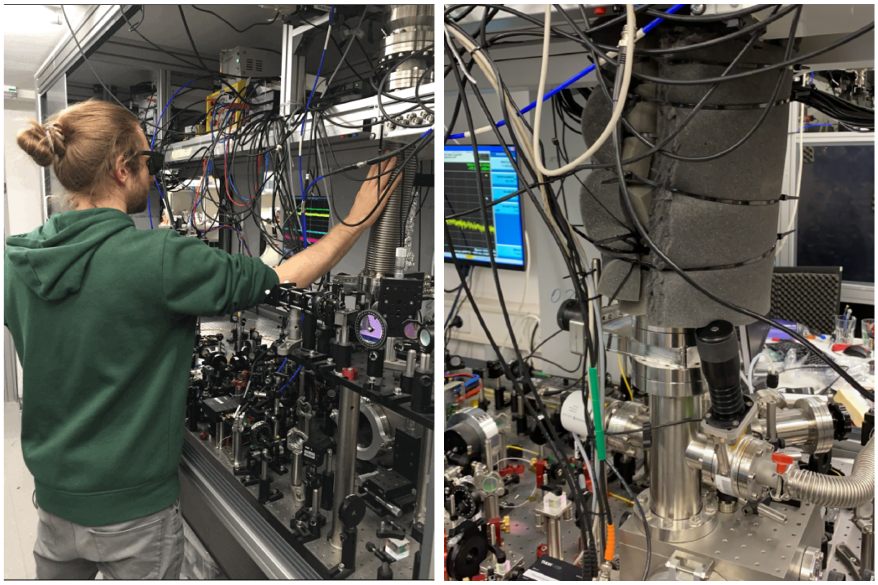
(a) (b)

Figure 5.11: **Acoustic damping of the turbo pump bellows.** Vibrations coupled into the particle position relative to the cavity standing wave resulting in changes to the optomechanical coupling. It was determined that the long metal bellows connecting the science chamber and the turbo pumps was amplifying this noise. (a) A researcher provides pressure to the metal bellows and monitors the oscillations in the particle position to determine locations for optimal damping. (b) The final acoustic damping configuration used in the measurements of Chapter 6. Precise buildup of layers of clay and foam secured by zip ties significantly damped vibrations resonant with bellows.

5.5.3 Tweezer Referencing

Referencing of the tweezer position, polarization and detuning relative to the cavity is critical for successful operations of the experiment. To initially align the position we use cameras to image the optical cavity along the $x-$axis and the $y-$axis. To roughly set the y position of the nanoparticle relative to the center of the cavity, we pull the particle away from the cavity along the $z-$axis until we can see its scattered light beside the cavity mirror using the triaxial stage of the microscope objective. The x and z positions can be

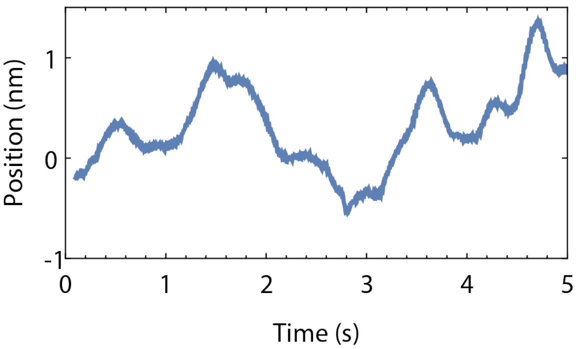

Figure 5.12: **Particle position stability along the cavity standing wave.** We measure the light exiting one of the cavity mirrors which is correlated with the coupling of the particle to the cavity mode. We position the particle at the cavity node where the scattered light is minimal and monitor the change in scattered light. We can then calibrate this by referencing the scattered light of the particle placed at the cavity antinode to extract the particle position. We position the nanoparticle in the vicinity of the mode for maximum sensitivity and record the position during a standard measurement. The standard deviation of such drifts is ~ $\lambda/1000$ demonstrating a high degree of stability. This is critical for suppressing phase noise heating.

done by looking at the orthogonal image. To fine tune the position, we sweep the tweezer frequency using the piezo inside of the Mephisto which provides ~ 100MHz of range. We then slowly tune the laser temperature to search for light coupled out of some cavity mode on the $x-$axis camera as shown in Figure 5.13. Then we can iterate this process to increase the coupling of the particle to lower order cavity modes until we reach the TEM00 mode.

To further optimize the coupling we can lock the laser to the cavity and take heterodyne or homodyne measurements of the cavity output. As the particle coupling increases the signature of the mechanical motion in the cavity signal will also increase allowing for a quantitative reference of the coupling. We can subsequently measure the magnitude of the coupling as outlined in Chapter 6. We can additionally use the DC value of the light exiting the cavity to position the particle along the standing wave.

In order for the positioning referencing to work we need to set the polarization of the tweezer to be along the $y-$axis to orient the dipole radiation

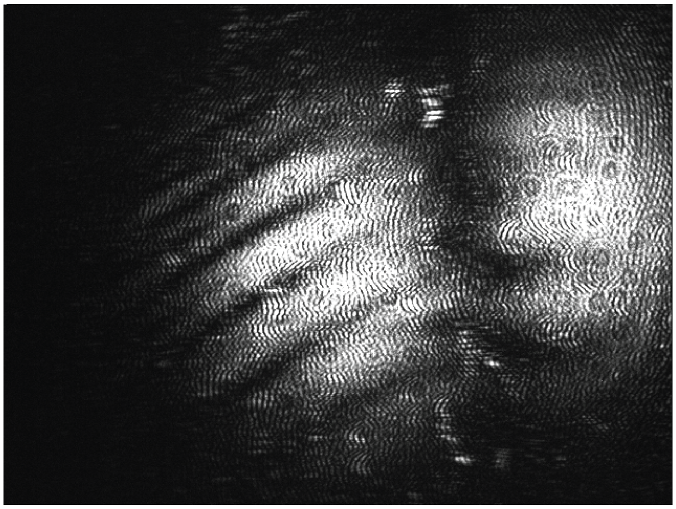

Figure 5.13: **An image of the cavity output showing the particle coupled to a TEM10 mode during the tweezer alignment.**

pattern along the cavity axis. Again, due to the geometry this can roughly be done according to the reference frame of the lab but for optimization we use the mechanical signal in the cavity measurement. From Equation 4.30, we know that the x and y motion maximally couple to the cavity with orthogonal polarizations. In this dissertation we're primarily concerned with the x motion so we rotate the tweezer polarization to maximize the x signal in the cavity output and minimize the y. This is depicted in Figure 5.14. This ensures any slight mismatches between the lab frame and the cavity frame are accounted for.

Lastly, due to the locking scheme, the detuning can drift as the cavity expands and contracts. This is because we are locking the laser to a cavity mode one free spectral range away from the coupling mode. Changes in the cavity length directly impact the free spectral range. While the laser is still locked to the cavity, ω_{FSR} can change by at maximum ~ $2\pi \times 350\mathrm{kHz}$. This is on the order of our mechanical frequency and therefore a very relevant change. Therefore during an experimental run we repeatedly perform a weak measurement of the detuning. We derive a weak probe beam from the tweezer light and use this to drive the cavity and detect the light reflected

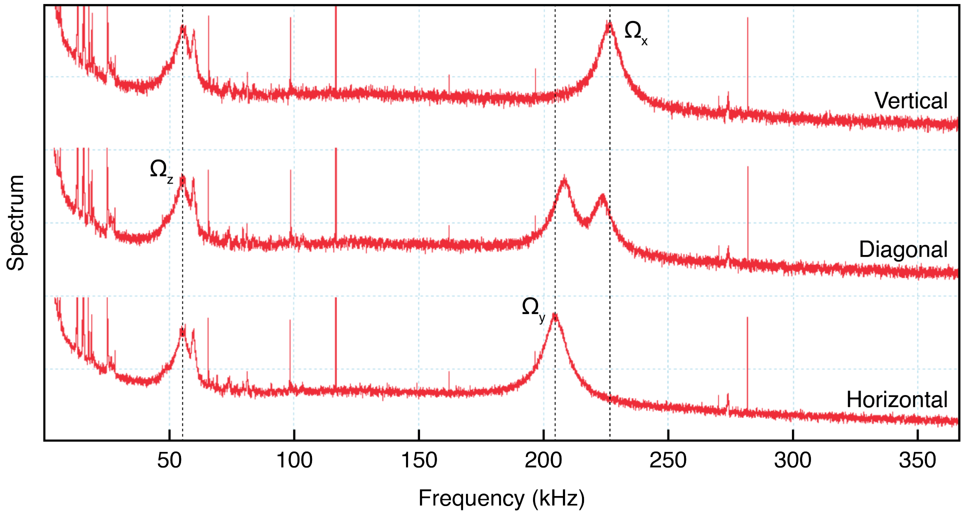

Figure 5.14: **Spectra of the cavity output for varying polarization.** For vertical polarization the x motion is coupled to the cavity and the y is coupled for horizontal polarization. In between the two modes can couple in any mixture. Note the frequencies change slightly as the diagonal polarization is not perfectly linear and therefore modifies the tweezer geometry slightly according to Appendix B.

from the cavity on a photodiode.[31]. We can sweep this light independently from the tweezer light by way of an EOM to measure the exact detuning and recalibrate our measurements.

For all the measurements presented in later sections of this dissertation we reference the position and polarization at least once before an experimental run and the detuning is measured with almost every measurement. This ensures we keep a minimal amount of uncertainty for all of our system parameters.

---

[31] We actually perform the same procedure for an optomechanically induced transparency (OMIT) measurement [36] but we set the expected detuning to be much larger than the mechanical frequency so we don't actually see the particle signal. This effectively performs a very fast transmission measurement using the same OMIT hardware.

5.5.4 Future Considerations

Many of the problems outlined in this section could be solved by switching to a setup whereby the cavity is locked to a stable laser source through the use of piezo built into the cavity holder to maintain the cavity length. One effect not mentioned previously is the fact that during pumpdown the evacuation of atmosphere in the chamber effectively changes the cavity length and therefore cavity mode frequency. If the nanoparticle is not positioned at the exact center of the cavity this causes the particle to experience a slow moving optical lattice which modulates the coupling. This can cause problems, especially for larger particles[32]. If both of the cavity mirrors were placed on piezos it would be possible to lock the DC particle position to a single period of the standing wave thereby eliminating this problem. It would further give another method of modulating the coupling as the piezos are generally faster than the stable speed of the tweezer trap. This would of course also solve the problem of lock lifetime assuming a suitable cavity mount material, like Zerodur, with low thermal expansion is chosen.

It would also be favourable to use a single sided cavity configuration for future iterations as it is challenging to recombine the cavity outputs to regain the full signal to noise ratio as will be detailed in the subsequent section.

5.6 Detection

The final section of the apparatus to discuss is the detection. For detection of the optical and mechanical modes, we perform interferometric measurements. In particular, we use light that has interacted with the optical and mechanical modes to reconstruct the state of our optomechanical system.

We start by recalling Glauber's model of a photodetector [73]. In this

---

[32] As the particle size increases, so too does the coupling and scattered power assuming all other parameters stay fixed. If a large enough particle is positioned away from a cavity node, it can scatter a substantial amount of power into the cavity and create its own standing wave trap. This trap minima may not be situated at the tweezer minima and can destabilize the overall optical potential resulting in the loss of a particle.

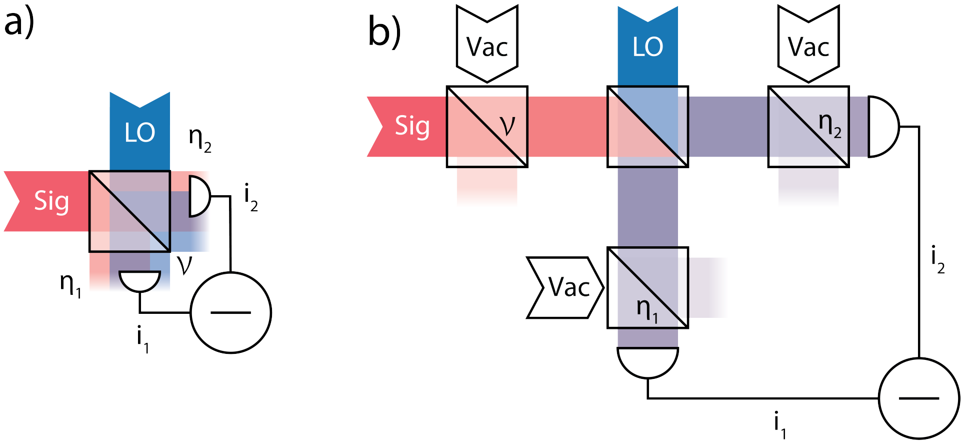

Figure 5.15: **Representations of the general detection scheme used in this work.** a) The interferometric detection in the lab frame. A signal and local oscillator are mixed on a beamsplitter and subsequently detected by photodiodes. Due to the phase shift from reflections, interference between the signal and local oscillator in each of the beamsplitter outputs is perfectly out of phase with each other. Therefore, a balanced detection scheme is employed whereby the photocurrents of each detector is subtracted from the other to cancel out DC noise. Mode matching of the signal relative to the local oscillator, quantified by the visibility $\mathcal{V}$, and the detection mode relative to the local oscillator, quantified by the detection efficiencies η_i, are also illustrated. b) The beamsplitter model of the information loss. The system in a) is expanded and each mode matching is mapped to a beamsplitter.

seminal work, it was shown that the current of a photodetector $\hat{\imath}(t)$[33] is proportional to the number of incident photons. In particular we will write

$$\hat{\imath}(t) = \mathcal{G} \int_A \hat{f}(\vec{r}, t) dA \tag{5.1}$$

where $\mathcal{G}$ is the gain of the detector, A is the active area and $\hat{f}(\vec{r}, t)$ is the photon flux. Usually the signal flux is weak resulting in a poor signal to noise

---

[33] Here we write that the current is a quantum observable which is then made classical through a later decoherence channel. One can move this decoherence channel before the point of measuring this current and rewrite it as a classical observable with no significant changes to the results discussed here.

ratio when comparing to realistic detection noise processes. To overcome such a technical limitation, we amplify the signal through the use of a local oscillator. A diagram for such a setup is shown in Figure 5.15. The field operator at the detector is then given by

$$\hat{a}_{\text{det}}(t) = \mathcal{R}\hat{a}_{\text{sig}} + \mathcal{T}\hat{a}_{\text{LO}}(t) \tag{5.2}$$

where $\mathcal{R}$ and $\mathcal{T}$ are the reflectivity and transmittivity respectively. This has the normal conditions that $|\mathcal{R}|^2 + |\mathcal{T}|^2 = 1$ and $\mathcal{R}\mathcal{T}^* + \mathcal{R}^*\mathcal{T} = 0$. To align with the real world, we note that the signal and local oscillator may not occupy the same spatial mode. It is then useful to extend Equation 5.2 and, as will be justified in a moment, we will only consider the mode parallel to that of the local oscillator in which case we find

$$\hat{a}_{\text{det},\parallel}(t) = \mathcal{T}_{\text{eff}}\left(\mathcal{R}\mathcal{V}\hat{a}_{\text{sig}} + \mathcal{R}\sqrt{1-\mathcal{V}^2}\hat{a}_{\text{vac},\mathcal{V}} + \mathcal{T}\hat{a}_{\text{LO}}(t)\right) + \mathcal{R}_{\text{eff}}\hat{a}_{\text{vac,eff}}(t) \tag{5.3}$$

where $\|\mathcal{T}_{\text{eff}}\|^2$ is the detection efficiency and $\mathcal{V}$ is the visibility of the interference quantifying the overlap of the signal with the local oscillator. All mismatches or losses of information are modelled as beamsplitters with their associated vacuum modes $\hat{a}_{\text{vac},i}$ to preserve the total amount of fluctuations.

Then the detected current would be

$$\begin{aligned} i(t) \approx \mathcal{G}\Big[&|\mathcal{T}_{\text{eff}}|^2|\mathcal{R}|^2 F_{\text{sig}}(t) + |\mathcal{T}_{\text{eff}}|^2|\mathcal{T}|^2 F_{\text{LO}}(t) \\ &+ |\mathcal{T}_{\text{eff}}|^2\mathcal{V}\mathcal{R}^*\mathcal{T}\hat{a}^\dagger_{\text{sig}}(t)\hat{a}_{\text{LO}}(t) \\ &+ |\mathcal{T}_{\text{eff}}|^2\sqrt{1-\mathcal{V}^2}\mathcal{R}^*\mathcal{T}\hat{a}^\dagger_{\text{vac},\mathcal{V}}(t)\hat{a}_{\text{LO}}(t) + \mathcal{R}^*_{\text{eff}}\mathcal{T}_{\text{eff}}\mathcal{T}\hat{a}^\dagger_{\text{vac,eff}}(t)\hat{a}_{\text{LO}}(t) + \text{c.c.}\Big] \end{aligned} \tag{5.4}$$

where F_i is the classical detectable flux of a given mode. I have dropped all of terms fluctuation terms not proportional to the local oscillator. The first two terms describe the DC current associated with the coherent amplitude of the signal and local oscillators, the third term is the term we are interested in and the last two terms are noise terms coming from improper mode-matching and detection efficiency respectively.

In the experimental realization of this detection, classical intensity noise will couple to the current through the DC terms. To suppress this, we use the so-called balanced detection scheme shown in Figure 5.15. In this case, we take the other port associated with Equation 5.2 and carry out an analogous calculation for the current of the second detector.

Let us now assume that $|\mathcal{R}|^2 = |\mathcal{T}|^2 = \frac{1}{2}$ and the detection efficiency for each detector is the same. Then, taking the difference of the currents from these two detectors yields

$$\begin{aligned}\Delta i(t) = i|\mathcal{T}_{\text{eff}}|^2\mathcal{V}\mathcal{G}\hat{a}^\dagger_{\text{sig}}(t)\hat{a}_{\text{LO}}(t) + i|\mathcal{T}_{\text{eff}}|^2\sqrt{1-\mathcal{V}^2}\mathcal{G}\hat{a}^\dagger_{\text{vac},\mathcal{V}}(t)\hat{a}_{\text{LO}}(t)\\ + \mathcal{R}^*_{\text{eff}}\mathcal{T}_{\text{eff}}\left[\mathcal{T}\hat{a}^\dagger_{\text{vac,eff}}(t) - \mathcal{R}\hat{a}'^\dagger_{\text{vac,eff}}(t)\right]\hat{a}_{\text{LO}}(t) + \text{c.c.}\end{aligned} \tag{5.5}$$

where we have to note that the quantum noise introduced by the detection efficiency is not common mode, hence we distinguish between $\hat{a}^\dagger_{\text{vac,eff}}(t)$ and $\hat{a}'^\dagger_{\text{vac,eff}}(t)$.

To calculate the spectrum we need to first compute the autocorrelation of our signal. For clarity, we will ignore all of the noise terms as they will a constant noise floor to the signal which is important when considering signal to noise but not the specifics of the mechanics. We then see that

$$\begin{aligned}\left\langle\Delta i(t)\Delta i(t')\right\rangle = \eta^2\mathcal{G}^2\Big[\left\langle\hat{a}_{\text{out}}(t)\hat{a}^\dagger_{\text{out}}(t')\right\rangle\left\langle\hat{a}^\dagger_{\text{LO}}(t)\hat{a}_{\text{LO}}(t')\right\rangle + \left\langle\hat{a}^\dagger_{\text{out}}(t)\hat{a}_{\text{out}}(t')\right\rangle\left\langle\hat{a}_{\text{LO}}(t)\hat{a}^\dagger_{\text{LO}}(t')\right\rangle\\ - \left\langle\hat{a}_{\text{sig}}(t)\hat{a}_{\text{sig}}(t')\right\rangle\left\langle\hat{a}^\dagger_{\text{LO}}(t)\hat{a}^\dagger_{\text{LO}}(t')\right\rangle - \left\langle\hat{a}^\dagger_{\text{sig}}(t)\hat{a}^\dagger_{\text{sig}}(t')\right\rangle\left\langle\hat{a}_{\text{LO}}(t)\hat{a}_{\text{LO}}(t')\right\rangle\Big]\end{aligned} \tag{5.6}$$

where $\eta = |\mathcal{T}_{\text{eff}}|^2\mathcal{V}^2$ is the detection efficiency, and I have assumed $\hat{a}_{\text{LO}}(t)$ and $\hat{a}_{\text{out}}(t)$ are uncorrelated. Next, we will assume the local oscillator is some coherent drive with an amplitude $\alpha_{\text{LO}} = \sqrt{F_{\text{LO}}}e^{-i\omega_{\text{LO}}t - i\theta_{\text{LO}}}$. Then we can simplify the above expression by assuming that the mean flux of the local oscillator is significantly stronger than that of the signal such that we can ignore the fluctuation terms of the local oscillator. We will also switch to the rotating frame as before in which case we found we can identify

$\hat{a}_{\rm out}(t) \to \hat{a}_{\rm out}(t)e^{-i\omega_d t}$ and write

$$\begin{aligned}\left\langle \Delta i(t)\Delta i(t')\right\rangle \to \eta^2\mathcal{V}^2\mathcal{G}^2F_{\rm LO}\Big[&\left\langle \hat{a}_{\rm out}(t)\hat{a}^\dagger_{\rm out}(t')\right\rangle e^{i\omega_{\rm het}(t-t')} + \left\langle \hat{a}^\dagger_{\rm out}(t)\hat{a}_{\rm out}(t')\right\rangle e^{-i\omega_{\rm het}(t-t')} \\ &- \left\langle \hat{a}_{\rm out}(t)\hat{a}_{\rm out}(t')\right\rangle e^{i\omega_{\rm het}(t+t')}e^{2i\theta_{\rm LO}} - \left\langle \hat{a}^\dagger_{\rm out}(t)\hat{a}^\dagger_{\rm out}(t')\right\rangle e^{-i\omega_{\rm het}(t+t')}e^{-2i\theta_{\rm LO}}\Big] \end{aligned} \tag{5.7}$$

$$= \eta^2\mathcal{V}^2\mathcal{G}^2F_{\rm LO}\left\langle \hat{Y}_{\theta(t)}(t)\hat{Y}_{\theta(t')}(t')\right\rangle \tag{5.8}$$

where $\omega_{\rm het} = \omega_{\rm LO} - \omega_d$ is the so-called heterodyne frequency, $\hat{Y}_{\theta(t)}(t) = i\left(\hat{a}_{\rm out}(t)e^{i\theta(t)} - \hat{a}^\dagger_{\rm out}(t)e^{-i\theta(t)}\right)$ is an arbitrary quadrature set by $\theta(t) = \omega_{\rm het}t + \theta_{\rm LO}$. We can then see that if $\omega_{\rm het} = 0$ we can set one quadrature by the phase of the local oscillator while when $\omega_{\rm het} \neq 0$ the quadrature is constantly scanned. These two cases correspond to homodyne and heterodyne measurement schemes respectively.

In the case of heterodyne when the quadrature is rapidly scanned our intuition suggests the resulting spectrum should be an average of the phase and amplitude quadratures of the signal. We then need to consider the timescale of the measurement τ relative to the heterodyne frequency $\omega_{\rm het}$. We will consider heterodynes such that $\omega_{\rm het}\tau >> 1$.

$$\begin{aligned}S^{(\tau)}_{\Delta i\Delta i}(\omega) \propto \frac{1}{\tau}\int_{-\frac{\tau}{2}}^{\frac{\tau}{2}}\int_{-\frac{\tau}{2}}^{\frac{\tau}{2}} dtdt'\Big[&\left\langle \hat{a}_{\rm out}(t)\hat{a}^\dagger_{\rm out}(t')\right\rangle e^{i(\omega+\omega_{\rm het})(t-t')} + \left\langle \hat{a}^\dagger_{\rm out}(t)\hat{a}_{\rm out}(t')\right\rangle e^{i(\omega-\omega_{\rm het})(t-t')} \\ &- \left\langle \hat{a}_{\rm out}(t)\hat{a}_{\rm out}(t')\right\rangle e^{i(\omega+\omega_{\rm het})t}e^{-i(\omega-\omega_{\rm het})t'}e^{2i\theta} - \left\langle \hat{a}^\dagger_{\rm out}(t)\hat{a}^\dagger_{\rm out}(t')\right\rangle e^{i(\omega-\omega_{\rm het})t}e^{-i(\omega+\omega_{\rm het})t'}e^{-2i\theta}\Big]\end{aligned} \tag{5.9}$$

$$\approx \int d\omega' \left\langle \hat{a}_{\rm out}(\omega+\omega_{\rm het})\hat{a}^\dagger_{\rm out}(\omega')\right\rangle + \left\langle \hat{a}^\dagger_{\rm out}(\omega-\omega_{\rm het})\hat{a}_{\rm out}(\omega')\right\rangle. \tag{5.10}$$

In contrast to a homodyne measurement, where the positive and negative frequency components of the signal are added together, a heterodyne can recover these signals which can for instance be used to measure the Stokes and Anti-Stokes photons from a Raman scattering process. These differences are illustrated in Figure 5.16.

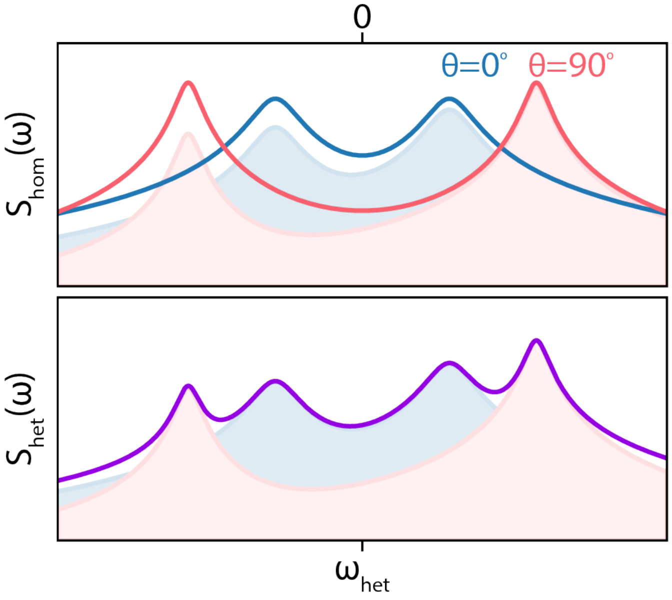

Figure 5.16: **Illustrations of homodyne and heterodyne spectra.** For the same signal composed of information in orthogonal quadratures (red and blue, filled), homodyne and heterodyne detection recover significantly different pieces of information. Homodyning the signal symmetrizes the positive and negative frequency components of the signal but retains the ability to measure in various quadratures (red and blue). Heterodyne instead shifts the signal up to ω_{het} and mixes the quadratures but instead gives information about the positive and negative frequency components of the combined signal.

5.6.1 Tweezer Detection

To directly measure the particle motion, we take advantage of the fact that the particle acts as a position dependent phase modulation on not only the cavity field but also the tweezer field. Due to its size however, the particle only modulates the phase of part of the beam, leaving the rest to transmit unaffected. A homodyne measurement of this tweezer field can be performed by collecting the transmitted light[34] since it includes both

---

[34] We use a lens with NA= 0.2 to collect and recollimate the tweezer light. A higher NA objective can be used but then one must be careful of back-reflections modulating the trapping potential.

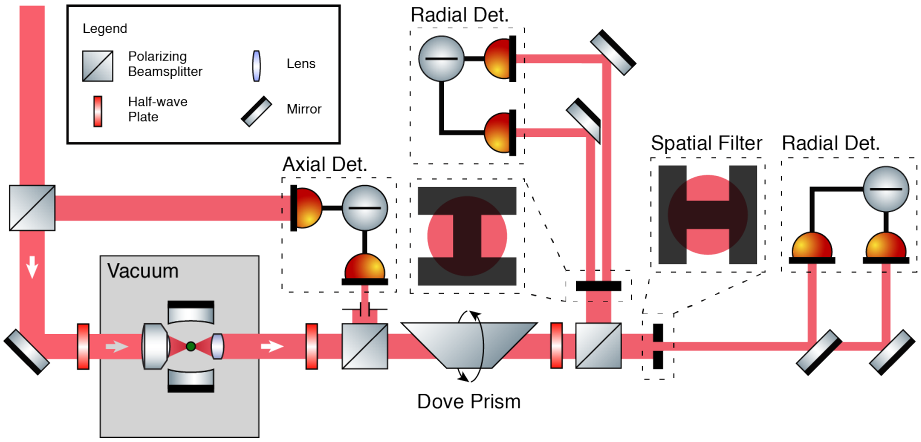

Figure 5.17: **Detection of the particle motion via the transmitted tweezer light.** The transmitted light from the tweezer is captured and recollominated by a small lens (NA= 0.2) before being split between the axial and radial detections. The axial detection utilizes a portion of the trapping light to cancel DC noise through the balanced detection. The signal is spatially filtered with an iris to increase the SNR. For the radial detections, a Dove prism is used to rotate the tweezer beam along its propagation axis to vary the projection angle of the particle motion onto the two detectors. Spatial filtering is then employed to select the regions with the relevant high informational density before the beam is split with D-shaped mirrors and detected.

the modulated and unmodulated fields which act as the signal and local oscillators respectively. Fortunately, it is has been shown[74] that in addition to the position dependent phase modulation there is also a constant $\pi/2$ phase delay between the two beams which maximizes the sensitivity of this scheme.

The specific setup for tweezer detection is shown in Figure 5.17. It is a modification of the setup detailed in the dissertation of Uroš Delić[36]. It is split into detection of axial and radial motions. Both detection schemes cannot directly employ the balanced scheme discussed in Section 5.6 without modifications. For the axial motion, defined according to the tweezer axis, common mode noise is rejected by splitting a small portion of the tweezer light before it enters the optical chamber and using this as the balancing light on the second port of a balanced detector[35]. For the radial motions, the beam is split by a D-shaped mirror instead of a beamsplitter since the latter would again lead to the rejection of the signal. Depending on the orientation of the D-shaped mirror, different projections of the radial motion can be detected. For full flexibility, we have two radial detections oriented such that they detect orthogonal projections of the radial motion[36]. A Dove prism is then used to rotated the beam before it interacts with the detection system to change in which frame of reference the measurements are performed.

It has been shown that information about the axial and radial motions are not uniformly distributed and in fact have some spatially varying information density across the transmitted tweezer beam profile[75]. Spatial filtering can be employed to increase the signal to noise ratio (SNR). We utilize an iris in the axial beam path and custom filters[37] in the radial beam paths to take advantage of this mechanism. Since we are predominantly interested in measuring the motion of the particle along the cavity axis, this is the tweezer detection we optimize and we have achieved a maximum SNR of ~ 30dB with a 104nm radius particle, an example of which is shown in Figure 5.18.

5.6.2 Cavity Detection

To measure the optical mode inside the cavity, we return to the input output relations from Chapter 3 where we found that the mode leaking out of the cavity is given by

$$\hat{a}_{\mathrm{out}}(t) = \sqrt{\kappa}\hat{a}(t) + \hat{a}_{\mathrm{in}}(t). \tag{5.11}$$

We can then identify $\hat{a}_{\mathrm{sig}} = \hat{a}_{\mathrm{out}}$ and use the models of detection we have just discussed. The optical setup, including the detection of the cavity

---

[35] Thorlabs PDB-425C-AC

[36] A quadrant photodiode would give the same result except the increased sensor area gives a reduced detection bandwidth. For the particle frequencies in this work it is necessary to use the more complicated scheme but the principle is the same.

[37] We built custom spatial filters out of anodized aluminum parts. They are ”H” shaped and effectively act as two irises, the axis between which sets the angle of the radial motion projection.

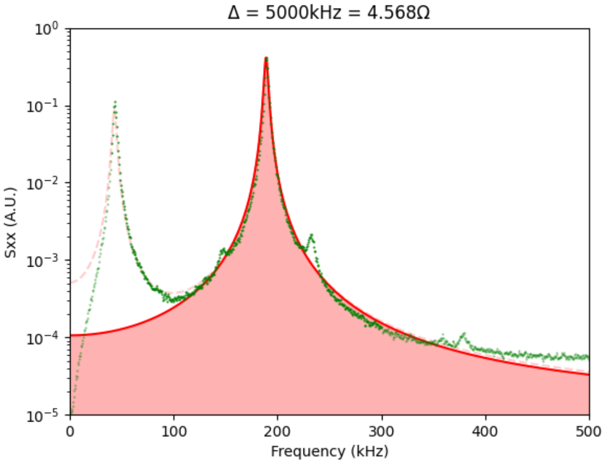

Figure 5.18: **An example of the PSD $S_{xx}(\omega)$ reconstructed from the tweezer detection.** The computed PSD (green points) clearly shown the $x-$motion at ~ 200kHz and the $z-$motion at ~ 50kHz. The latter is a byproduct of imperfect alignment and suppression of the axial mode with the balanced detection scheme. A DC block is added to reduce impacts of drifts on the photocurrent resulting in the cutoff just below the $z-$motion. A full fit (red dashed) can be done and the relevant $x-$motion (red shaded) can be extracted demonstrating near perfect agreement with theory.

mode, is shown in Figure 5.1. The cavity mode is generally detected via heterodyne but we can easily replaced the AOM generating the heterodyne local oscillator with a mirror mounted to a piezo for locking a homodyne. It is important to note that all of the windows on the vacuum chamber are standard flat windows except for the one window on the side of the cavity detection. This is to reduce parasitic standing waves from forming between the back-reflections off of the photodiodes and the vacuum window.

Since our tweezer detection has a relatively low SNR[38] it is oftentimes useful to use the cavity to reconstruct the motional state of the particle.

For the double sided cavity configuration shown in Figure 5.1 we show

---

[38] The SNR of the tweezer detection in our system is insufficient for cooling the particle motion close to the ground state via feedback cooling as has recently been demonstrated[76, 77]. Since this is not the goal for the detection, it has so far been unimportant to pursue improvement.

in Appendix C that the heterodyne spectrum is given by

$$\begin{aligned} S_{\Delta i \Delta i}(\omega) \propto\ & |\kappa_1 \chi_l(\omega+\omega_{\mathrm{het}})\nu(\omega+\omega_{\mathrm{het}}) - 1|^2 + \kappa_1\kappa_2 |\chi_l(\omega+\omega_{\mathrm{het}})|^2 |\nu(\omega+\omega_{\mathrm{het}})|^2 \\ & - 2(\kappa_1+\kappa_2)|\nu(\omega+\omega_{\mathrm{het}})|^2 |\chi_l(\omega+\omega_{\mathrm{het}})|^2 \mathrm{Re}\left\{\chi_l^*(-(\omega+\omega_{\mathrm{het}}))\left[\chi_m(\omega+\omega_{\mathrm{het}}) - \chi_m^*(-(\omega+\omega_{\mathrm{het}}))\right]\right\} \\ & + 2g^2\kappa_1 \mathrm{Re}\left\{\nu(\omega+\omega_{\mathrm{het}})\chi_l(\omega+\omega_{\mathrm{het}})\chi_l^*(-(\omega+\omega_{\mathrm{het}}))\left(\chi_m(\omega+\omega_{\mathrm{het}}) - \chi_m^*(-(\omega+\omega_{\mathrm{het}}))\right)\right\} \\ & + g^2\kappa_1\gamma |\nu(\omega+\omega_{\mathrm{het}})|^2 |\chi_l(\omega+\omega_{\mathrm{het}})|^2 \left[|\chi_m(\omega+\omega_{\mathrm{het}})|^2(\bar{N}+1) + |\chi_m(-(\omega+\omega_{\mathrm{het}}))|^2 \bar{N}\right] \\ & + g^2\kappa_1\gamma |\nu(\omega-\omega_{\mathrm{het}})|^2 |\chi_l(-(\omega-\omega_{\mathrm{het}}))|^2 \left[|\chi_m(\omega-\omega_{\mathrm{het}})|^2(\bar{N}+1) + |\chi_m(-(\omega-\omega_{\mathrm{het}}))|^2 \bar{N}\right] \\ & + g^4\kappa_1(\kappa_1+\kappa_2)|\nu(\omega+\omega_{\mathrm{het}})|^2 |\chi_l(\omega+\omega_{\mathrm{het}})|^2 |\chi_l(-(\omega+\omega_{\mathrm{het}}))|^2 \left|\chi_m(\omega+\omega_{\mathrm{het}}) - \chi_m^*(-(\omega+\omega_{\mathrm{het}}))\right|^2 \\ & + g^4\kappa_1(\kappa_1+\kappa_2)|\nu(\omega-\omega_{\mathrm{het}})|^2 |\chi_l(-(\omega-\omega_{\mathrm{het}}))|^2 |\chi_l(\omega-\omega_{\mathrm{het}})|^2 \left|\chi_m(\omega-\omega_{\mathrm{het}}) - \chi_m^*(-(\omega-\omega_{\mathrm{het}}))\right|^2 . \end{aligned} \tag{5.12}$$

If the drive detuning is either on resonance or far away from it, this simplifies to

$$S_{\Delta i \Delta i}(\omega) \approx 1 + \frac{g^2\kappa_1}{x_{\mathrm{zpf}}^2} |\chi_l(\omega - |\omega_{\mathrm{het}}|)|^2 S_{xx}(\omega - |\omega_{\mathrm{het}}|). \tag{5.13}$$

By suitably choosing ω_{het} such that all of the structure in S_{xx} is away from DC, we can measure both the Stokes and Anti-Stokes sidebands for thermometry. This will be used in Chapter 6.

To measure a specific quadrature, we set $\omega_{\mathrm{het}} = 0$ and lock the relative phase of the local oscillator to the signal. In this case, the homodyne of the cavity output gives

$$\begin{aligned} S_{\Delta i \Delta i}(\omega) \propto\ & |\kappa_1\chi_l(\omega)\nu(\omega) - 1|^2 + \kappa_1\kappa_2|\chi_l(\omega)|^2|\nu(\omega)|^2 \\ & - 4\cos\theta g^2\kappa_1(\kappa_1+\kappa_2)|\nu(\omega)|^2|\chi_l(\omega)|^2 \mathrm{Re}\left\{e^{-i\theta}\chi_l^*(-\omega)\left[\chi_m(\omega) - \chi_m^*(-\omega)\right]\right\} \\ & + 4\sin\theta g^2\kappa_1 \mathrm{Re}\left\{e^{-i(\theta-\pi/2)}\nu(\omega)\chi_l(\omega)\chi_l^*(-\omega)\left(\chi_m(\omega) - \chi_m^*(-\omega)\right)\right\} \\ & + g^2\kappa_1\gamma|\nu(\omega)|^2|\chi_l(\omega)e^{-i\theta} + \chi_l^*(-\omega)e^{i\theta}|^2 \left[|\chi_m(\omega)|^2(\bar{N}+1) + |\chi_m(-\omega)|^2\bar{N}\right] \\ & + 4\cos^2\theta g^4\kappa_1(\kappa_1+\kappa_2)|\nu(\omega)|^2|\chi_l(\omega)|^2|\chi_l(-\omega)|^2\left|\chi_m(\omega) - \chi_m^*(-\omega)\right|^2 \end{aligned} \tag{5.14}$$

which again simplifies greatly in the resonant case to

$$S_{\Delta i \Delta i}(\omega) \approx 1 + 4\cos^2\theta \frac{g^2\kappa_1}{x_{\text{zpf}}^2}|\chi_l(\omega)|^2 S_{xx}(\omega). \tag{5.15}$$

We can immediately see the effect averaging has on the signal to noise ratio in the heterodyne as the factor of 4 is not present. Additionally, we see that on resonance, the mechanics couple to the phase quadrature of the light as we would expect from the Hamiltonian we wrote initially. Compared to the heterodyne, the Stokes and Anti-Stokes sidebands are now degenerate in frequency but we can resolve the quadrature information[39]. This demonstrates the utility of the two different types of detection.

5.7 Conclusion and Outlook

As a result of the trailblazing history of this apparatus many aspects can be significantly improved using modern techniques and technology. Better cavities are available, including microcavities which boast mode volumes many orders of magnitude smaller than ours, could increase the optomechanical coupling rate significantly. Furthermore, contemporary loading techniques would can essentially eliminate difficulties reaching shot-noise dominated cooperativities. Finally, the switch from an aluminum cavity mount to more appropriate materials like Zerodur or Macor would improve lock stability.

---

[39] As a consequence of the $x-$motion being coupled to only the phase quadrature of the light, we can see that the detected cavity spectrum should become flat as $\theta \rightarrow 0$ as we would expect.

Part III

Coupling Regimes

Chapter 6

Coupling vs. Dissipation

Two basic elements of most quantum protocols are the preparation of a pure quantum state and the manipulation of this state faster than the decoherence rate of the system. In this chapter we will demonstrate how we can leverage the coupling between a mechanical oscillator and an optical cavity to satisfy these requirements.

Whether or not a system exchanges information slower or faster than decoherence greatly modifies its behaviour. When the coupling is weak compared to the dissipation, decoherence dominates the interaction and the eigenmodes of the system are simply given by the mechanical and optical modes. In this case the interaction can modify the properties of each subsystem but no coherent manipulation can be performed between the two. This weak coupling regime can however be leveraged for cooling as the high dissipation and low effective bath temperature of the optical mode can be used to siphon energy away from the mechanical oscillator. As the coupling increases, the system transitions to the strong coupling regime. Specifically, once $g > \kappa/4$, the optical and mechanical subsystems hybridize giving rise to new eigenmodes of the Hamiltonian. The new so-called normal modes are linear superpositions of the photonic and phononic modes. The relevant scales are illustrated in Figure 6.1, including those relating to the transition rates of the system which will be discussed in the next chapter. The ability to operate in both regimes is important for achieving full quantum control of the system.

In this chapter, we will exclusively consider the interaction to be generated via coherent scattering discussed in Section 4.3. In terms of the

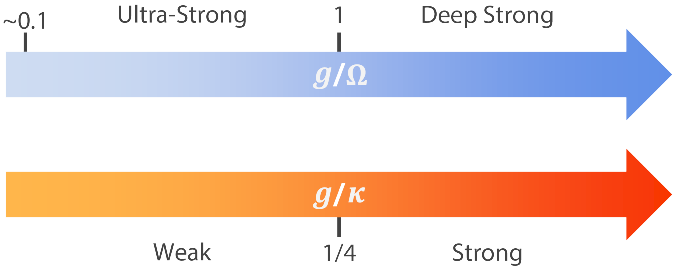

Figure 6.1: **The frequency scales for comparison with the coupling.** The coupling rate with respect to the dissipation sets the weak/strong scale governing mode hybridization. The transition rates of the system define the ultra/deep strong scale governing the perturbative nature of the interaction.

parameters which can be tuned in-situ,

$$g_x(\vec{x}_0) \propto P^{1/4} \sin\theta \sin(kx_0) e^{-\frac{y_0^2+z_0^2}{W_{\mathrm{cav}}^2}} \tag{6.1}$$

Additionally, for particles with $r << \lambda$, $g_x \sim r^{3/2}$. These parameters afford us considerable flexibility in tuning the coupling rate. We must also consider that in our system $\kappa >> \gamma$ for nominal background gas pressures. We therefore only consider the optical dissipation rate in the rest of our discussions.

A selection of the following results in the next two chapters can be found in our recent papers: ”Cooling of a levitated nanoparticle to the motional quantum ground state” [78] and ”Linear Ultrastrong Optomechanical Interaction” [79].

6.1 Weak Coupling

Let us consider the motional PSD $S_{xx}(\omega)$ given in Equation 4.7. Setting $g = 0$, we uncouple the systems and $\nu(\omega) = 1$ which allows us to recover the uncoupled mechanics we saw in Chapter 2 as we would expect. Then when $g < \kappa/4, \Omega_x/10$, we can cast this equation into the same form as our uncoupled oscillator[40] by reformulating our expression in terms of a bath with an effective occupation $\bar{N}_{\text{eff}}$ and coupling γ_{eff} resulting in

$$S_{xx}(\omega) = x_{zpf}^2 \left[\gamma_{\text{eff}}|\chi_m(\omega)|^2(\bar{N}_{\text{eff}}+1) + \gamma_{\text{eff}}|\chi_m(-\omega)|^2\bar{N}_{\text{eff}}\right] \tag{6.2}$$

where

$$\gamma_{\text{eff}} \approx \gamma + 4g^2\Omega_x\Delta\kappa|\chi_l(\Omega_x)|^2|\chi_l(-\Omega_x)|^2, \tag{6.3}$$

$$\Omega_{\text{eff}} \approx \Omega_x - 2g^2\Delta\left[\left(\frac{\kappa}{2}\right)^2 - \Omega_x^2 + \Delta^2\right]|\chi_l(\Omega_x)|^2|\chi_l(-\Omega_x)|^2, \tag{6.4}$$

$$N_{\text{eff}} \approx \frac{\gamma}{\gamma_{\text{eff}}}\bar{N}_{\text{therm}} + \bar{N}_{\text{shot}}, \tag{6.5}$$

$$\bar{N}_{\text{shot}} = \frac{1}{4}\frac{\Omega_x}{\Delta}\left[\eta^2 + \left(1 - \frac{\Delta}{\Omega_x}\right)^2\right] \tag{6.6}$$

and $\eta = (\kappa/2)/\Omega_x$ quantifies the sideband resolution. Equations 6.3 and 6.4 described the so-called optical damping and optical spring effects while Equation 6.5 demonstrates the effect that coupling the mechanical oscillator to the cavity has on the oscillator's energy. We can reach a minimum occupation of $n_{\text{min}} = \frac{1}{2}(\sqrt{1+\eta^2} - 1)$ at an optimal detuning of $\frac{\Delta}{\Omega} = \sqrt{1+\eta^2}$. For our system with $\kappa \approx \Omega_x$ we expect $n_{\text{min}} \approx 0.16$[41].

In the experiment, we can scan the detuning to map out the optical spring and dampings to reconstruct the coupling rate g as shown in Figure 6.2. One should note that the optical mode is not unaffected by this coupling and it also undergoes a frequency shift and modification of the damping. Since the modes do not hybridize there is no avoided crossing however, the two modes still repel one another as shown in Figure 6.3.

---

[40] This largely holds if we relax the constraint on $g < \Omega_x/10$ requiring the system to not be in the ultrastrong coupling regime. However as both of these constraints are generally satisfied simultaneously in our system, we will retain the more stringent condition.

[41] Note that we have ignored other heating effects in this simplified approximation. A thorough examination with other heating contributions included has been performed[36] and found only minor corrections to this prediction for the parameter regime available to our experiment.

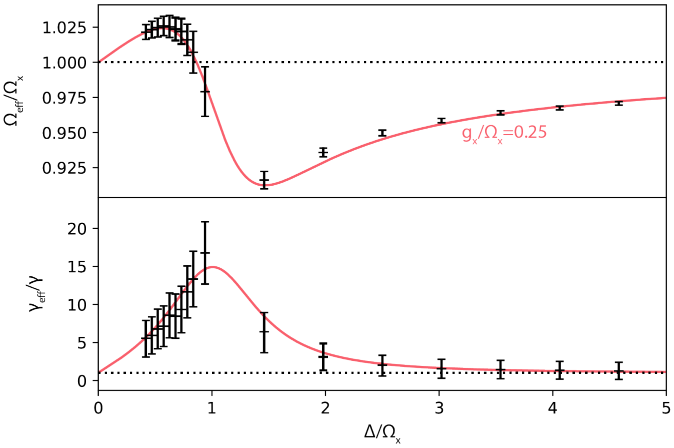

Figure 6.2: **An example of the modified spectral properties in the weak coupling regime.** While scanning the detuning we measure the mechanical spectrum and extract the resonance Ω_{eff} and linewidth γ_{eff}. The joint behaviour of these two properties is then fit and the coupling rate is extracted. This measurement was performed with a 73nm radius particle.

6.1.1 Ground State Cooling

In optomechanics we generally leverage dissipation for cooling a system with the eventual goal of preparing the mechanical oscillator in the ground state of motion, the more effective the cooling the purer the state. This was the subject of our paper ”Cooling of a levitated nanoparticle to the motional quantum ground state” [50] and some of the work presented in this subsection can also be found there.

As we saw, judicious choice of the detuning and reduction of γ through the evacuation of the background gas can lead to an expected minimum occupation of $n_{\text{min}} < 1$ indicating ground state cooling of the mechanical oscillator should be possible. Given the gas damping model from Subsection 2.3.1 and a room temperature environment, we can see we would require a background pressure of $P < 10^{-6}$mbar to reach a ground state occupation for a 73nm radius silica nanoparticle. As we demonstrated in Chapter 5, this is above the base pressure of the vacuum chamber and therefore an achievable goal.

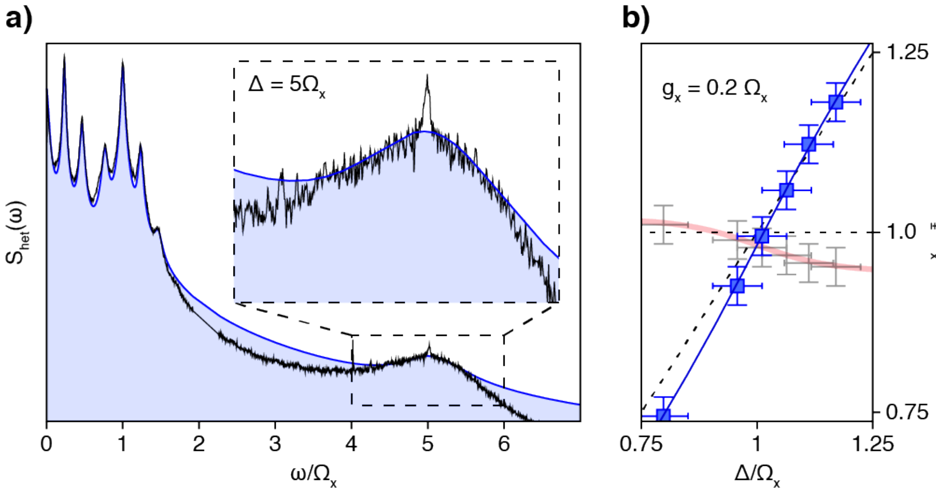

Figure 6.3: **The analogue of the optical spring for the cavity mode.** a) The heterodyne spectra contains both the mechanical modes but also the much broader optical mode (magnified). The full spectrum can be fit to provide a direct measurement of the detuning. b) The frequencies of the mechanical (faded crosses) and optical modes (blue squares) as a function of detuning. The dashed lines illustrate the uncoupled mode frequencies. Since the system is only weakly coupled, the modes do not hybridize and therefore do not exhibit normal mode splitting nor an avoided crossing. However, since the coupling is positive, they still repel each other before ultimately crossing at $\Delta = \Omega_x$.

For verification of the ground state we used Raman sideband thermometry. Since the tweezer detection has a SNR of ~ 30dB at a pressure of 4mbar and the signal amplitude is proportional to the damping, we would have a SNR ≈ −30dB when the ground state occurs which is clearly unfeasible. Instead we take advantage of the weak coupling to also provide diagnostics using the heterodyne detection of the coupled cavity mode. We can then use the full model from Subsection 5.6.2 to recover $S_{xx}(\omega)$ and therefore the occupation N_{eff}.

To resolve the ground state we collected all of the light from one side of the cavity[42] and mixed this with a strong local oscillator such that we operated just below saturation of the balanced detector[43]. To optimize the balancing of the detection and thus the rejection of common mode noise, we used a variable fiber beamsplitter[44]. This provided the additional benefit of ensuring the signal and local oscillator were perfectly mode matched. The signal was coupled into this fiber with $> 50\%$ coupling efficiency. To provide a flat noise background we used a heterodyne frequency of 10.2MHz and collected the data using an oscilloscope[45] with a sample interval of 16ns. We used a standard 1kHz resolution bandwidth when computing the PSDs and took enough data to average the spectra 10^6 times (roughly 1000s) to reduce the shot noise variance to the point where we could discern the cooled x-motion. The result is shown in Figure 6.4. We achieve a minimum occupation of $\bar{n}_x = 0.43 \pm 0.03$ resulting in the particle being in the ground state $70 \pm 2\%$ of the time[46]. The discrepancy between the achieved minimum occupation and theoretical minimum is largely due to the finite background pressure in the chamber. As shown in Figure 6.4c, further reduction of the pressure results in a much closer agreement at which point photon recoil, discussed in Subsection 2.3.4, becomes the dominant heating mechanism.

While this result opens up a new regime of macroscopic quantum free-fall experiments, the coherence time is still too short to perform significant

---

[42] We tried coherently combining the two cavity outputs by mixing them on a polarizing beamsplitter. Setting the two polarization of the two beams to maximize the output out of one of the beamsplitter ports and then giving them a slight ellipticity, we were able to use the small amount of rejected light to lock the beams together using a mirror mounted on a piezo in one of the beam paths. This was only marginally useful as it increased the SNR by 2.2dB but came at the cost of additional complexity and locking requirements.

[43] The local oscillator was set to $\sim 100\mu$W while the signal was $\sim 1\mu$W. We verified that the noise floor of the resulting spectrum was set by the shot noise of the laser and not the electronics. We additionally took background traces of both the shot noise and electronic noise to compensate for any fluctuations over our signal area.

[44] Newport F-CPL-1060-N-FA

[45] pico Technology PicoScope 5442B

[46] This also corresponds to a temperature of $12.2 \pm 0.5\mu$K

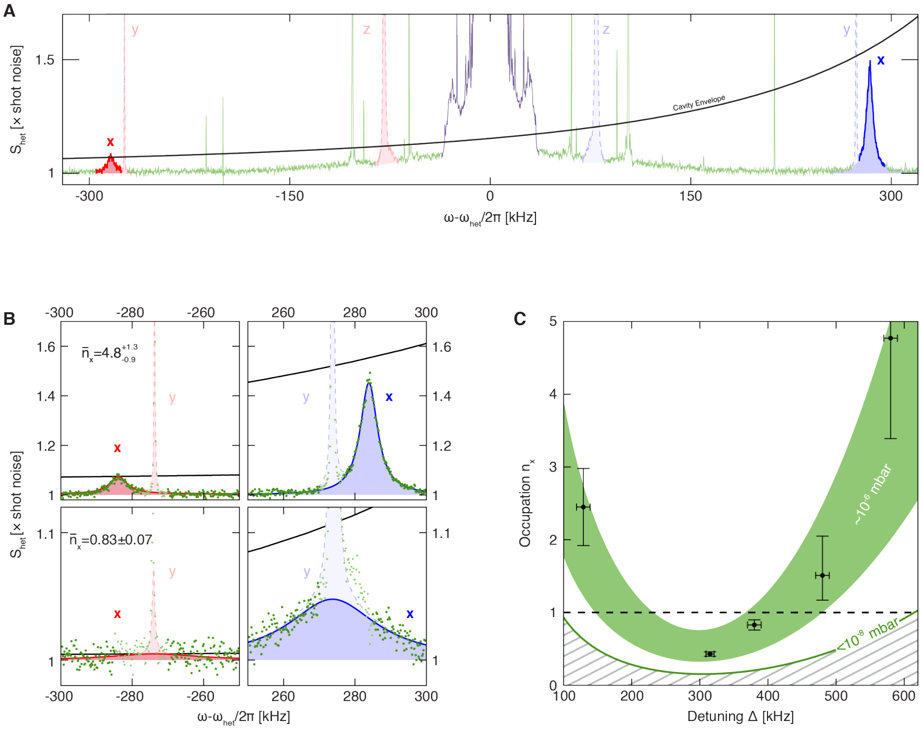

Figure 6.4: **Heterodyne spectrum of the cavity output and the resulting phononic occupations.** a) The negative frequency Stokes (red) and positive frequency anti-Stokes (blue) sidebands are mixed with a strong local oscillator in a heterodyne configuration. The resulting spectrum contains information about the motion of the mechanical oscillator in all 3 orthogonal directions. Only the x-mode is appreciably coupled to the optical mode and thus the z and y motion remain uncooled. The presence of phase noise from the carrier (purple) is negligible at the relevant mechanical frequencies. b) Magnified Stokes and anti-Stokes sidebands of the $x-$motion are shown for different occupations near the ground state associated with $\Delta/2\pi = 580 \pm 10$kHz (top row) and 380 ± 10kHz (bottom row). c) Phononic occupation as a function of detuning. At the optimal detuning for cooling we reach a minimum occupation of $\bar{n}_x = 0.43 \pm 0.03$. Errorbars include uncertainty in the detuning Δ and the cavity dissipation κ. The theoretical model, including the uncertainty in the background gas pressure, is depicted by the green band. Below the lower green line at 10^{-8}mbar, the impact of the background gas is negligible compared to other heating mechanisms.

wavepacket expansion[47]. This can be improved by making the previously discussed upgrades to the vacuum system. Additionally, switching from a room temperature environment to that of a cryostat would further improve the vacuum, decrease the bath temperature and reduce the effect of black body radiation. Unfortunately this comes at the cost of significant technological overhead. An alternative option using squeezing through the cavity interaction will be discussed in Chapter 7.

6.2 Strong Coupling

Once $g > \kappa/4$, the information exchange starts to beat decoherence, the modes hybridize, and the system transitions to the strong coupling regime. Our approximation of Equation 4.7 to Equation 6.2 begins to break down and we need to use the full theory. In this case, the normal modes are the solution to

$$|M(\Omega_\pm + i\gamma_\pm)| = 0 \tag{6.7}$$

where M is the coupling matrix from Equation 4.4, and $\Omega_\pm$ and $\gamma_\pm$ are the normal mode frequencies and dissipation rates respectively. The normal mode frequencies are shown in Figure 6.5 as the coupling is increased. For $\kappa/4 < g << \Omega$, we can write out a compact expression when $\Delta = \Omega$ in which case the normal mode frequencies are simply

$$\Omega_\pm \approx \Omega\left[1 \pm \sqrt{\left(\frac{g}{\Omega}\right)^2 - \left(\frac{\kappa}{4\Omega}\right)^2}\right] \xrightarrow[g>>\kappa]{} \Omega \pm g. \tag{6.8}$$

As we discussed, for $g < \kappa/4$ the eigenmodes of the system are just the degenerate optical and mechanical modes and at $g = \kappa/4$ the new normal modes arise and start to split. Note that the normal modes are said to not be

---

[47] With a background pressure of 10^{-6}mbar, we estimate the maximum coherence time in a freefall experiment to be only $\sim 1\mu$s which would expand the wave packet from $3 \rightarrow 10$pm[50]. In order to fully utilize the solid nature of the nanoparticle, we would need to expand the wavepacket beyond the size of the nanoparticle itself requiring a further increase of 3 orders of magnitude [35].

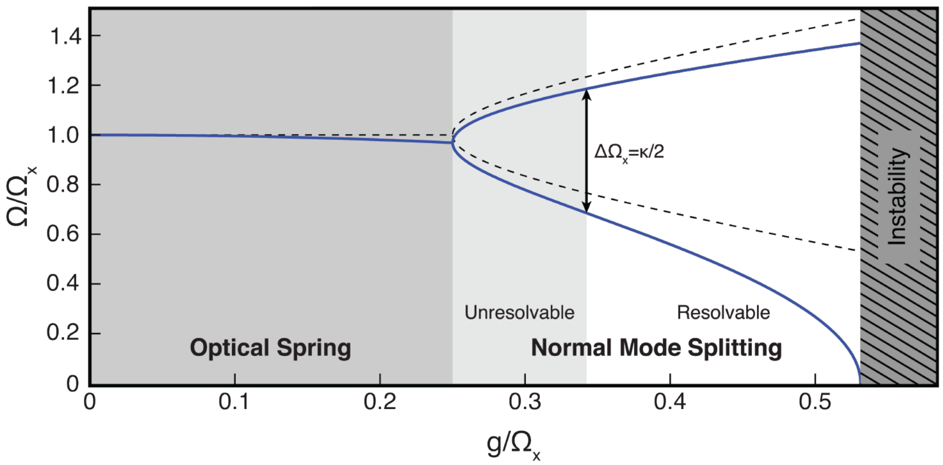

Figure 6.5: **The eigenfrequencies of the system as g is increased.** For this model $\Delta = \Omega_x = \kappa$. The dashed (solid) line is the strong coupling theory with (without) the rotating wave approximation. At $g = \kappa/4$ the degenerate eigenfrequencies split and only become resolvable later when the seperation is $\kappa/2$. As the coupling gets stronger, the lower eigenfrequency becomes 0 at which point the system becomes unstable. This will be elaborated upon in Chapter 7.

resolvable until $\Omega_+ - \Omega_- > \kappa/2$. To understand this, we look at the projection of the normal modes onto the mechanical basis. In this case, we can refer back to Equation 4.7. We can then plot the spectrum as g increases as in Figure 6.6. Even though at $g = \kappa/4$ the modes have hybridized, we can't immediately tell that there is any mode hybridization from the spectrum. It is only until higher couplings that the new normal modes are resolvable. At this point we can see the normal mode splitting and as g increases, the normal mode splitting converges to $2g$ and acts as an immediate verification of the coupling rate.

6.2.1 Observation of Normal Mode Splitting

The observation of normal mode splitting has previously been used to experimentally verify the system is operating in the strong coupling regime[80]. Since this is a sufficient condition, we perform a similar measurement by

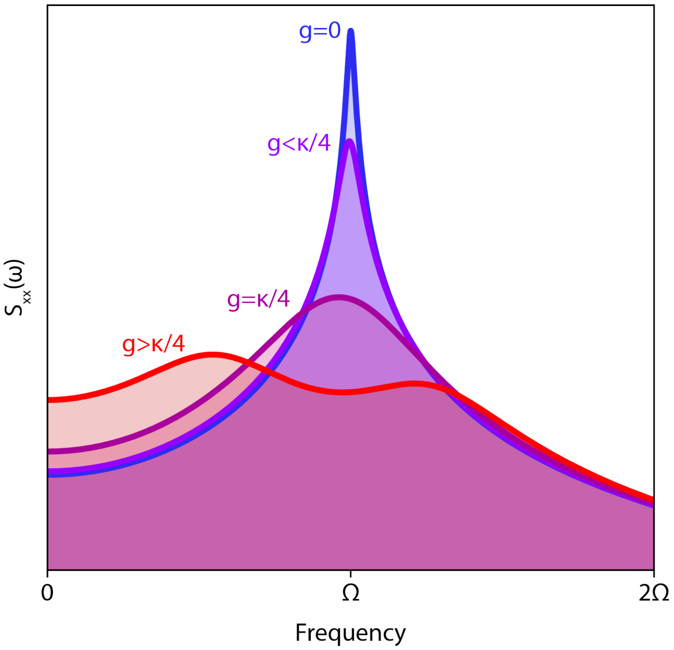

Figure 6.6: **Example spectra as the coupling rate g increases relative to the dissipation in the system κ.** Weak coupling causes the effective damping of the mechanical oscillations to increase and at $g = \kappa/4$ the system transitions from the weak to the strong coupling regime. In this case, the modes hybridize but are only resolvable at some larger coupling rate where the difference between the normal mode frequencies is larger than $\kappa/2$. The resolvable curve was made when $g = 0.4\kappa$.

simply measuring the projection of the normal modes onto either the mechanical or optical subsystem through the tweezer detection or cavity detection respectively. Since this effect is independent of the temperature of the oscillator, we can measure at high temperature where the SNR is large instead of being restricted to only the cavity detection[48].

---

[48] As previously discussed, the tweezer and cavity frames do not perfectly match and therefore all 3 motional degrees of freedom couple to the cavity in some capacity. This can make it challenging to clearly observe modifications to the spectral linewidth and fitting is necessary to make conclusive observations. In constrast to this, although the SNR of the tweezer detection is lower, it is easier to filter motional modes from one another. This is advantageous for produce clear demonstrations of the modification of spectral features.

To perform this measurement, we use a 104nm radius particle[49] and couple it to the optical cavity. For reasons discussed in the next chapter, we do not optimally couple the particle to the cavity but instead operate at some intermediate coupling. For this measurement, the tweezer power is set such that $\Omega_x = \kappa$ for simplicity.

We measure both the optical and mechanical subsystems simultaneously to provide a full picture of the system. We use the heterodyne detection for the optical mode, this time with sample interval of 32ns and 10^4 averages with a resolution bandwidth of 500kHz. To detect the particle motion, we use the tweezer detection with the same data acquisition parameters. We set the three tweezer detections such that one of the radial detections is optimized for the $x-$motion and suppresses the $y-$motion[50]. The power for this detection is set to almost saturate the detector to maximize the SNR. The other radial detection then uses the remaining tweezer light and is optimized for the detection of the $y-$motion and suppression of the $x-$motion.

Inevitably, some cross talk between the mechanical modes remains in the tweezer detection. To perform the analysis, we first take advantage of the poor SNR of the $y-$detection. The $x-$motion is heavily suppressed below the noise floor such that only the $y-$ and $z-$motions are still visible. These are then independently fit to extra the physical parameters $\Omega_{y,z}$ and $\gamma_{y,z}$. These parameters are then used for a full model of the $x-$detection from which we can then extract the coupling g_x. This process is detailed in Figure 6.7. We see great agreement between the model and the data in both detections. To further reduce the set of free parameters, we take a measurement at $\Delta >> \Omega_x$ such that the systems are effectively decoupled and we can fit the $x-$spectrum to recover Ω_x and γ_x. Then the detuning is set to $\Delta = \Omega_x$ and the spectrum is again measured. The only physical free parameter is the

---

[49] As we saw the 71nm particle gave a coupling close to $\kappa/4$ and through modifying the power we could in principle enter the strong coupling regime and resolve the normal mode splitting. However, increasing the particle size from 71nm to 104nm should increase the maximum coupling by ~ 1.5 times.

[50] The optimization of the detection is done once the particle is already in place inside of the cavity. Changing the particle position drastically changes the coupling to the photodiodes and therefore the balancing and SNR.

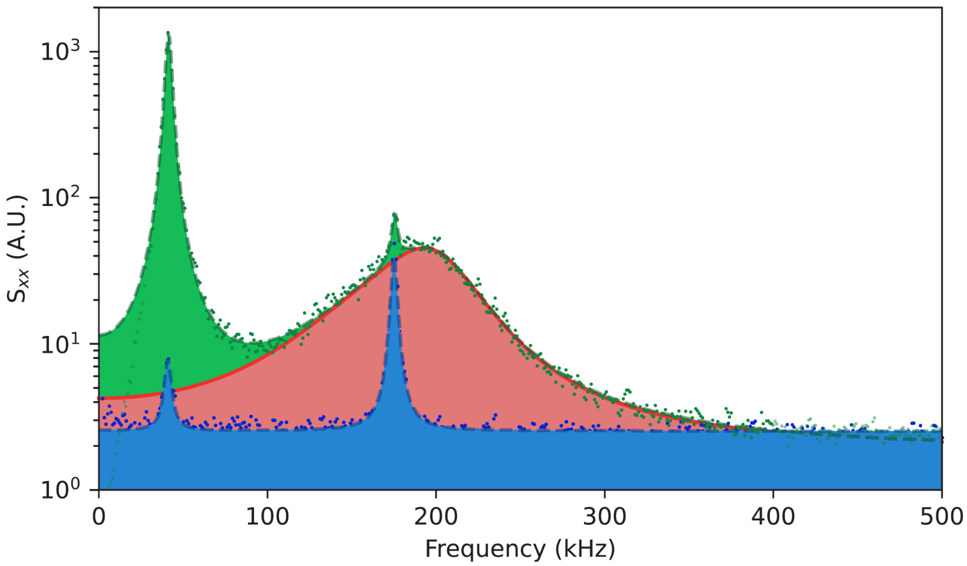

Figure 6.7: **Tweezer detection scheme for the reconstruction of the x−motion.** The y−detection (blue) is optimized such that no x−motion is visible. A fit is then applied to recover the frequencies and dampings of the y− and z−motion. This is then used as input into the fit of the x−detection (green) such that the only free physical parameters correspond to the x−motion. From the total fit, the x−contribution (red) is extracted.

coupling rate g, the rest are specifics of the detection[51]. The result of this measurement can be seen in Figure 6.8. We observe a clear signature of normal mode splitting and recover a coupling rate of $g = 0.3\kappa$ which is right at the onset of the resolvable criterion. This demonstrates the ability to beat decoherence in the manipulation of the quantum state of our system.

6.3 Conclusion and Outlook

Together, the demonstrated ability to prepare the optomechanical system in the ground state and manipulate it faster than decoherence form the basis for full coherent quantum control. A clear development on these results is to

---

[51] In particular, the coupling of each motion to the detection and the noise floor are free parameters. Everything else is already fixed by independent measurements. The detuning is measured through spectroscopy as has already been covered.

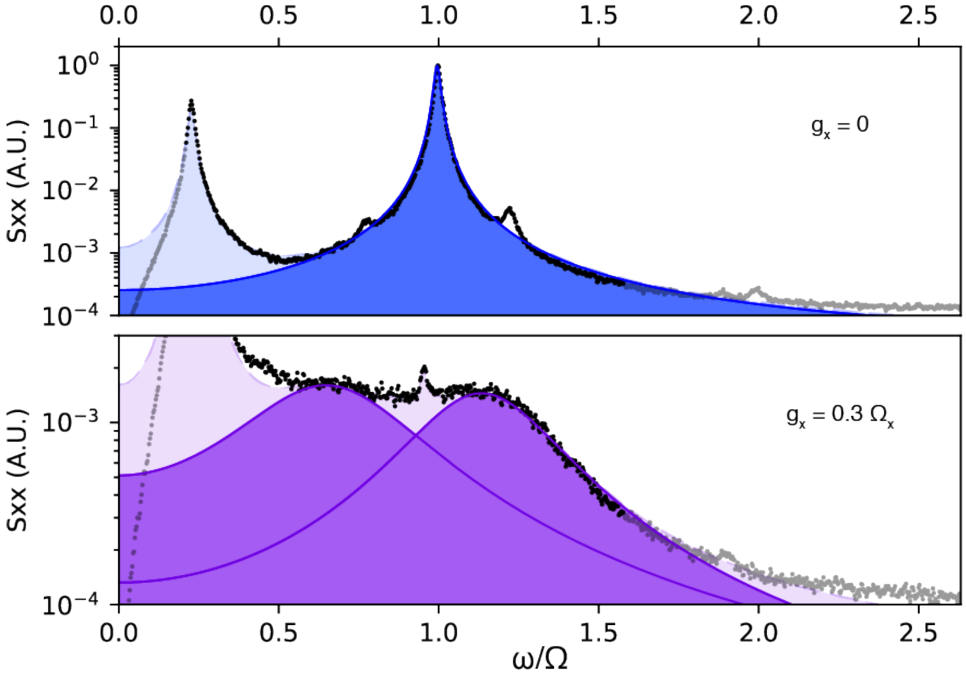

Figure 6.8: **Normal mode splitting in the strong coupling regime.** The parameters of the uncoupled $x-$motion are fixed when the system is effectively uncoupled (upper plot). The full fit (light blue shaded) is used to extract only the x parameters (dark blue shaded). Then the system is coupled and tuned such that $\Delta = \Omega_x$ (lower plot). Once again a fit is performed (light purple shaded) and the normal modes are found (dark purple shaded). We see an excellenet agreement between theory and experiment demonstrating a clear signature of normal mode splitting.

increase the cooperativity further by increasing the coupling and decreasing the decoherence. In addition, while the ability to quench the system by modifying the coupling through any of the parameters in Equation 6.1 is an interesting possibility, demonstration of both ground state cooling and strong coupling simultaneously would be an interesting next step. To do so would require $\frac{k_B T}{\hbar Q} << \kappa << \Omega_x$ which should be satisfied at reachable pressures so long as the tweezer power is increased to be well sideband resolved[81, 82].

Chapter 7

Coupling vs. Transition Energy

In addition to the previously demonstrated elements in our quantum control toolbox, it is of great interest to be able to entangle our subsystems. To do so requires we reintroduce the cross terms $\hat{a}\hat{b}$ and $\hat{a}^\dagger\hat{b}^\dagger$ that are neglected in the perturbative approach to our system and the rotating wave approximation. Of course these terms always play a role in the dynamics of the system[83] but the level at which they do so is governed by the relationship between the coupling rate g and the energy scale of our system Ω[52].

Due to historical precedent the system is said to enter the ultrastrong coupling (USC) regime when $g/\Omega > 0.1$[53] Beyond this point, the Jaynes-Cummings model breaks down and one should use the full quantum Rabi model. When $g/\Omega = 1$, the interaction strength is comparable to the bare energies of the system and this system enters the deep-strong coupling (DSC) regime[85]. At this point the interaction begins to dominate the dynamics of the system[54]. Historically, these regimes have been challenging to reach due to the large energy scales of experimental systems and have only been recently achieved in a handful of carefully engineered devices.

---

[52] Since the energy of the optical mode $\hbar\Delta$ is tunable and we want the optical and mechanical modes to interact according to their susceptibilities, the energy scale is set only by the mechanical frequency. This is in contrast to the weak-strong scale which is almost entirely dependent on the cavity parameters.

[53] This threshold has no physical significance since there is no critical point for ultrastrong phenomenon. Instead this was established following the initial observation of USC in a GaAs doped quantum well at $g/\Omega = 0.11$[84].

[54] For completeness, we will mention the very-strong coupling (VSC) regime in which the coupling becomes comparable to the spacing between excited states of a qubit[86, 87]. Given the harmonic oscillator nature of our system, we will ignore this regime in our discussion.

In this chapter, we will demonstrate how not only can the coherent-scattering interaction reach the USC regime but that it is straightforward to extend this to the DSC regime. Recall from Figure 6.1 that this is independent of the weak-strong coupling regimes, although in the current experimental realization both the USC and DSC regimes coincide with the strong coupling regime. This fact will be used to our benefit as we will see.

7.1 Ultrastrong Coupling

Only following the experimental realization of the strong coupling regime in 1983[8] did the world consider pursuing coupling regimes where perturbation theory breaksdown. The first observation of the USC regime occured just over a decade ago[4] and since then interest in larger couplings has flourished due to the ability of such a system to mix states with different occupations. The presence of non-negligible counter-rotating terms in the interaction Hamiltonian no longer conserves the number of excitations in the system. Consequently entanglement, superradiant phases and virtual excitations can emerge in USC systems. Furthermore, applications for enhancing quantum metrology exist based on the modification of strong coupling phenomena. With such a diverse set of applications, it is advantageous to investigate the USC regime in a similarly diverse set of systems.

Before the adaptation of coherent scattering to optomechanics, optomechanical systems have largely been confined to the strong coupling regime[55]. In our apparatus, the largest coupling previously reached through the dispersive interaction was $g/\Omega \approx 0.05$[50] and was limited by technical limitations on laser power. However, as the intracavity power increases, additional problems arise for investigating most interesting USC phenomena[56]. Comparing estimates for the coupling rates from dispersive and coherent scattering show an order of magnitude increase for the same drive power.

---

[55] Outside of the solid-state canon of optomechanics, single molecular vibrations have been used to reach couplings of up to $g/\Omega = 0.3$[88, 7]

[56] Since the dispersive interaction is maximized at the slope of the intensity profile of the standing wave, phase noise of the laser greatly impacts the coherence of the system.

To investigate it in our system, we can use the same Equation 6.7 for the eigenmodes of the system. For our system where $\kappa \approx \Omega_x$, we will consider the case where the system is both strongly and ultrastrongly coupled. Then we can write a modified form of Equation 6.8 for the normal mode frequencies

$$\Omega_{\pm} = \Omega\sqrt{1 - \left(\frac{\kappa}{4\Omega}\right)^2 \pm 2\sqrt{\left(\frac{g}{\Omega}\right)^2 - \left(\frac{\kappa}{4\Omega}\right)^2}}. \tag{7.1}$$

This modification is shown in Figure 6.5 alongside its strong coupling counterpart.

7.1.1 Dynamical Instability

Recall that the modification of the mode frequencies is on the scale of g and, as g approaches the transition frequencies, the lower transition frequency can reach zero[57]. Indeed, solutions of Equation 6.7 show the damping becomes negative at this point. The system therefore becomes dynamically unstable and, in the case of our levitated system, the particle is lost from the optical trap. It is well known that the source of this instability is a strong two-mode squeezing effect which amplifies the mechanical motion [89]. It has been shown [90] that this instability occurs at a coupling of

$$\left(\frac{g}{\Omega}\right)^2 > \frac{1}{4}\left(\frac{\Delta}{\Omega} + \frac{\left(\frac{\kappa}{2}\right)^2}{\Delta\Omega}\right). \tag{7.2}$$

While not present in non-linear systems, this instability was previously considered a detrimental feature of coupled harmonic oscillators. However, recently it has been demonstrated that it can be harnessed to greatly enhance the sensing capabilities of levitated optomechanical systems [91, 35, 92–95]. One can also take advantage of the squeezing in such a way as to overcome the short coherence time for freefall experiments and achieve wavepacket sizes on the order of the particle radius [96]. It is therefore of great interest to reach this instability point in our optomechanical system.

---

[57] This is only the case if the interaction does not have a diamagnetic or Hopfield term which would act to stabilize it.

In our system with $\Delta \approx \Omega_x \approx \kappa$, this occurs when $g_x/\Omega_x > 0.5$.

7.1.2 Avoided Crossing

With our experiment, initial attempts to measure normal mode splitting with 104nm particles in Subsection 6.2.1 resulted in immediate loss of the particle as we approached a detuning of $\Delta = \Omega_x$. This suggested the coupling could be large enough to reach instability. Therefore to characterize the coupling rate a different approach was taken.

Since the system is operating in the strong coupling regime, we can use the avoided crossing of the normal modes to reconstruct the coupling rate. This then uses the same scheme as detailed in Subsection 6.2.1 but, instead of measuring at $\Delta = \Omega_x$ where the system is unstable, we can record the spectra as we scan the detuning. Following Equation 7.2, we can ensure the detuning is large enough that we can avoid losing the particle from the tweezer.

Since we will not take measurements at $\Delta = \Omega_x$ where the normal mode splitting is most evident in both the optical and mechanical bases, it is important that we fit all of the spectra together with a global model. Once again, the only free physical parameter is the coupling and the results can be see in Figure 7.1. We observe a maximum coupling of $g_x/\Omega_x = 0.55$, well inside the USC regime. In addition to performing the measurement with the particle maximally coupled to the cavity, we displaced the particle away from the cavity axis using the triaxial nanopositioner to reduce the coupling according to Equation 6.1. In this way we can tune the system to any of the previously mentioned coupling regimes. We have therefore demonstrated the ability to reach the onset of instability.

7.2 Deep-Strong Coupling

Since the first demonstration of USC, researchers have sought to reach ever larger couplings. Few systems have reached the DSC regime [5, 3, 97] since it was first explored theoretically in 2010 [85]. It has since been shown that

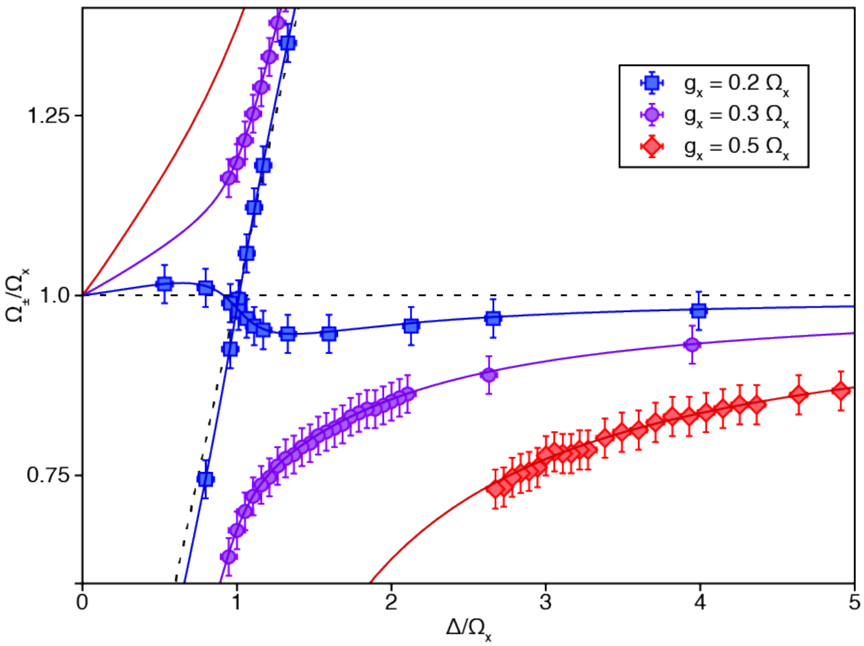

Figure 7.1: **Measured normal mode frequencies (markers) and fits (solid lines) as a function of detuning.** The decoupled mode frequencies are shown by the black dashed lines. For a weakly coupled system ($g < \kappa/4$) the modes repel one-another but still cross. This phenomenon still occurs at $g_x/\Omega_x = 0.2$ and the measured mode frequencies (blue squares) are in agreement with the theory. As the coupling increases the system enters the strong coupling regime for $g \geq \kappa/4$ at which point the mechanical and optical modes hybridize, giving rise to new normal modes of the coupled system. The normal modes, when the optics and mechanics are resonant with $\Delta = \Omega_x$, are split by approximately $2g$ and become resolvable when $\Omega_+ - \Omega_- > \kappa/2$. This occurs at $g_x/\Omega_x \approx 0.3$ (purple circles). As the coupling grows, the splitting increases and our system exhibits the predicted dynamical instability when $g_x/\Omega_x \approx 0.5$ (red diamonds).

exotic phenomena such as the breakdown of the Purcell effect [98] emerge in this regime. This new frontier of light-matter coupling is additionally relevant to the previously consider instability-based protocols and therefore

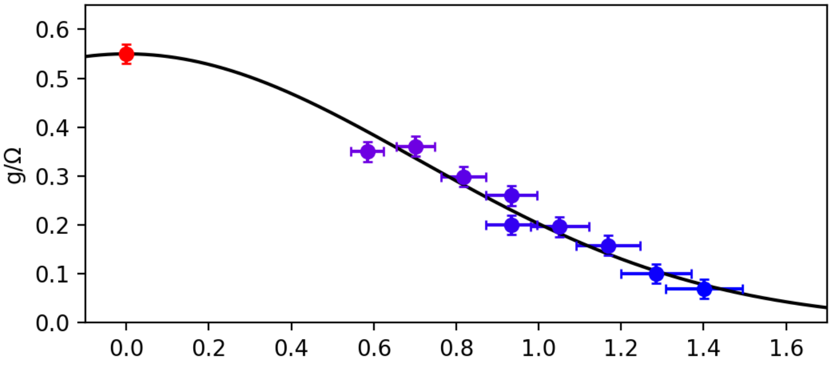

Figure 7.2: **Spatial dependence of coupling via coherent scattering.** As the nanoparticle is displaced away from the cavity axis, the overlap between the dipole scatter and the cavity mode should decrease following the cavity waist. Measured coupling rates (circles) as the particle is displaced away from the cavity axis. The cavity waist (solid line) is plotted for reference.

we aim to increase our coupling beyond the USC regime.

To do so we can consider the effect of particle size on the coupling rate. For small particles within the Rayleigh regime, the coupling will scale as $r^{3/2}$. This begins to breakdown at larger sizes due to two effects: the equilibrium trap position changes due to radiation pressure and the scattering profile diverges from the dipole profile we assumed previously. Both of these effects can be computed with numerical solutions of Maxwell's equations using the Mie solution for the scattering profile. This decreases the coupling rate as $g \propto 1/\sqrt{W_x(z_{\rm rad})W_y(z_{\rm rad})}$ where $W_{x,y}(z_{\rm rad})$ is the tweezer waist along the $x-$ and $y-$ directions at the modified equilibrium position $z_{\rm rad}$. Furthermore, our coherent scattering interaction assumes a dipole scattering profile. We can compare the full Mie solution to that of a dipole to compute the deviation. All of these effects are used to model the scaling of the coupling with particle size shown in Figure 7.3. We can see that for particles of $r \approx 140$nm we should enter the DSC regime. Such particles can be experimentally more challenging to work with due to their lower trap frequencies causing them to be more susceptible to low frequency noise sources, however we have previously been able to trap similarly sized particles.

7.2.1 Z-Coupling

Since the coupling scales with the zero-point fluctuations, we expect $g_z/\Omega_z \approx 8g_x/\Omega_x$ for a 105nm radius particle. This suggests that, when maximally coupled, the $z-$mode should already be deep within the DSC regime.

We therefore perform the same avoided crossing measurement as for the $x-$mode however we position the particle at an antinode of the cavity electric field such that the $z-$coupling is maximized. Furthermore, since the lower normal mode will be pushed towards DC where our technical noise is largest, we increase the tweezer power from 400mW to 900mW to give ourselves more leeway. We therefore expect a coupling of $g_z/\Omega_z \approx 3$. We perform the scan from $\Delta = 20\Omega_z$ down to $\Delta \approx 6\Omega_z$ at which point the $z-$mode already had appreciable overlap at zero frequency. The resulting spectra from this measurement can be seen in Figure 7.4. From the normal mode frequencies we find $g_z/\Omega_z = 1.2$.

While already in the DSC regime, this is far below the coupling we anticipated. We note that the increase in the $x-$frequency suggests that we populate the cavity with enough photons to build up an appreciable standing wave potential. This co-trapping of the particle by the cavity is generated by a quadratic term in the Hamiltonian which should take the same form as the previously discussed Hopfield term. In this case the measured normal mode frequency is higher than expected from the purely linear interaction, suggesting we are underestimating the coupling. Whether or not this additional quadratic potential is enough to stabilize the system is currently unknown and warrants further study.

To take advantage of the high $z-$coupling, we would also desire that the $z-$mode is strongly coupled to the cavity mode. Since $\Omega_z = 75$kHz we see that $g_z/\kappa > 0.46$ demonstrating it too operates in the SC regime. Furthermore, the splitting is given by $\Omega_+ - \Omega_- \approx 2g_z \geq 2 \times 1.2\Omega_z = 180\text{kHz} > \kappa/2$, the normal

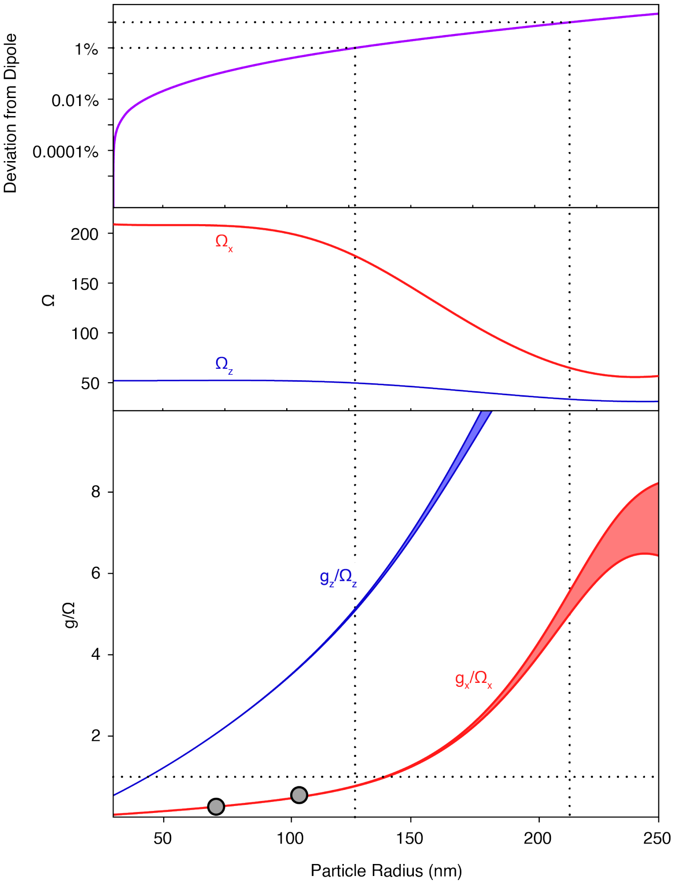

Figure 7.3: **Modeling of how the coherent scattering coupling scales with particle size.** We compute the deviation of the Mie solution from an ideal dipole (top). We see good agreement between the two solutions even up to particles with radii $r \approx 200$nm. We also model the effect of radiation pressure on the equilibrium trap frequencies mentioned in Subsection 2.1.3 for the $x-$ and $z-$modes (middle). This was done for the system tweezer parameters given in Subsection 5.3.3. Both of these effects give estimates for the scaling of the coupling with particle size (bottom). The $x-$mode should enter the DSC regime for particles of radius $r \approx 140$nm where the Mie solution deviates from the dipole approximation by a few percent. The effect of this deviation is given by the shaded region of the estimates as a full calculation of the higher order couplings would be required to more precisely predict the scaling.

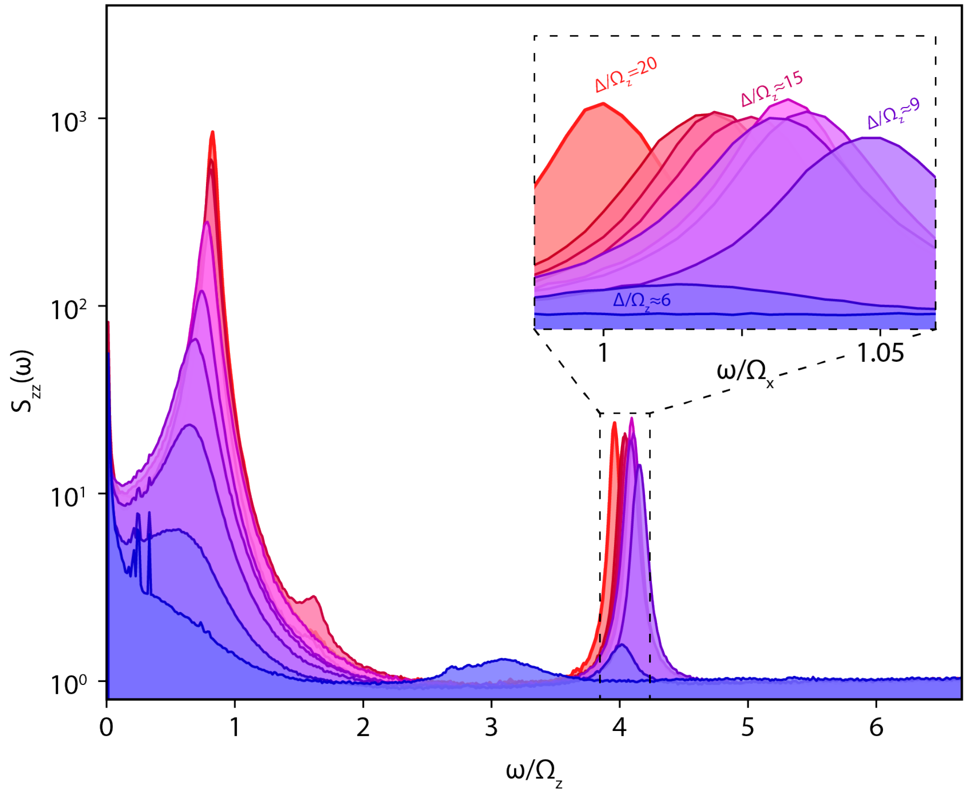

Figure 7.4: **Spectra from an avoided crossing measurement of the z−mode.** We scan the detuning from 2MHz down to 500kHz with Ω_z = 75kHz. From the trend of the lower normal mode frequency we estimate $g_z/\Omega_z = 1.2$. In the same spectra we see that for all but the closest detunings, the x−mode is shifted up in frequency. This is attributed to the buildup of the cavity mode population since the maximal coupling for z is away from the cavity field node.

mode splitting should be resolvable[58]. Unfortunately, due to the different coupling position along the standing wave, phase noise heating presents a large technical challenge for leveraging this interaction effectively.

---

[58] This is a technically challenging task since the mixing between the optical and mechanical modes is maximized at $\Delta = \Omega$ which is well below the instability threshold in this case.

7.3 Conclusion and Outlook

We have demonstrated that conventional optomechanical systems can reach both the USC and DSC regimes through the coherent scattering interaction. The parameters used in the apparatus to achieve the maximum observed coupling rates of $g_x/\Omega_x = 0.55$ and $g_z/\Omega_z = 1.2$ can easily be improved upon with contemporary technology.

An interesting avenue to explore would be the transition from a macroscopic cavity to a microcavity. Since $g \propto 1/\sqrt{V_{\text{cav}}}$ amd state-of-the-art microcavities boast mode volumes of $V_{\text{cav}} \sim 1 - 100\mu\text{m}^3$ compared to our cavity with $V_{\text{cav}} \approx 10^7\mu\text{m}^3$, we expect improvements by up to 4 orders of magnitude in the coupling. For these cavities, typical linewidths are $\sim 1{-}100$MHz which would require we greatly increase the trap frequencies to continue operating in the resolved sideband regime. This would be most easily done by using another cavity mode to trap the particle either through pumping the cavity or co-trapping through coherent scattering. This would have the added advantage of reducing differential shifts in the tweezer position relative to the cavity mode causing drifts in the coupling.

Besides building on these results for measuring squeezing of the mechanical motion, it has also been predicted that the system would automatically be entangled[99]. In this case, correlations between the mechanical and optical quadratures could be used as an entanglement witness without significant modifications of the experimental apparatus.

Appendices

Appendix A

Calculations & Derivations

A.1 Thermal Mechanical Oscilator in Classical Mechanics

A.1.1 Homogeneous Equation Ansatz

Our equation of motion is

$$\ddot{x}(t) + \gamma\dot{x}(t) + \Omega_x^2 x(t) = 0 \tag{A.1}$$

Our ansatz is

$$x(t) = x_0 e^{-\beta t}\cos(\alpha t) \tag{A.2}$$

for some constants α and β. Plugging this in, we get

$$0 = \left[(\beta^2 - \alpha^2)\cos(\alpha t) + 2\alpha\beta\sin(\alpha t)\right] x_0 e^{-\beta t} - \gamma\left[\beta\cos(\alpha t) + \alpha\sin(\alpha t)\right] x_0 e^{-\beta t} + \Omega_x^2 x_0 e^{-\beta t}\cos(\alpha t), \tag{A.3}$$

$$\implies 0 = (\beta^2 - \alpha^2 - \gamma\beta + \Omega_x^2)\cos(\alpha t) + (2\alpha\beta - \alpha\gamma)\sin(\alpha t). \tag{A.4}$$

From the sinusoidal terms, we can identify that $\beta = \gamma/2$ and then

$$0 = \beta^2 - \alpha^2 - \gamma\beta + \Omega_x^2, \tag{A.5}$$

$$= \left(\frac{\gamma}{2}\right)^2 - \alpha^2 - \gamma\frac{\gamma}{2} + \Omega_x^2, \tag{A.6}$$

$$\implies \alpha = \sqrt{\Omega_x^2 - \left(\frac{\gamma}{2}\right)^2}, \tag{A.7}$$

$$= \Omega_x\sqrt{1 - \frac{1}{(2Q)^2}} \tag{A.8}$$

where $Q = \Omega_x/\gamma$ is called the mechanical quality factor.

A.1.2 Inhomogeneous Equation Ansatz

Our equation of motion is

$$\ddot{x}(t) + \gamma\dot{x}(t) + \Omega_x^2 x(t) = \frac{1}{m}\sum_i F_i(t). \tag{A.9}$$

We can solve this second order ordinary differential equation by working in Fourier space. To do so, we note that

$$\begin{aligned}
\tilde{x}(\omega) &= \mathcal{F}\left[x(t)\right] && \text{(A.10)}\\
&= \int_{-\infty}^{\infty} x(t)e^{i\omega t}dt && \text{(A.11)}\\
x(t) &= \mathcal{F}^{-1}\left[\tilde{x}(\omega)\right] && \text{(A.12)}\\
&= \frac{1}{2\pi}\int_{-\infty}^{\infty}\tilde{x}(\omega)e^{-i\omega t}d\omega && \text{(A.13)}\\
\mathcal{F}\left[\dot{x}(t)\right] &= \mathcal{F}\left[\frac{\partial}{\partial t}\mathcal{F}^{-1}\left[\tilde{x}(\omega)\right]\right]\\
&= \mathcal{F}\left[\frac{\partial}{\partial t}\frac{1}{2\pi}\int_{-\infty}^{\infty}\tilde{x}(\omega)e^{-i\omega t}d\omega\right]\\
&= \mathcal{F}\left[\frac{1}{2\pi}\int_{-\infty}^{\infty}\tilde{x}(\omega)\frac{\partial}{\partial t}e^{-i\omega t}d\omega\right]\\
&= \mathcal{F}\left[\frac{1}{2\pi}\int_{-\infty}^{\infty}\tilde{x}(\omega)(-i\omega)e^{-i\omega t}d\omega\right]\\
&= -i\omega\tilde{x}(\omega) && \text{(A.14)}\\
\mathcal{F}\left[\ddot{x}(t)\right] &= -\omega^2\tilde{x}(\omega) && \text{(A.15)}\\
\tilde{F}_i(\omega) &= \mathcal{F}\left[F_i(t)\right] && \text{(A.16)}
\end{aligned}$$

The Fourier transform of the equation of motion is then

$$\left(-\omega^2 - i\gamma\omega + \Omega_x^2\right)\tilde{x}(\omega) = \frac{1}{m}\sum_i \tilde{F}_i(\omega). \tag{A.17}$$

We can introduce the mechanical susceptibility

$$\chi_m(\omega) = \frac{1}{\Omega_x^2 - \omega^2 - i\gamma\omega} \tag{A.18}$$

to write the equation of motion more succinctly

$$\tilde{x}(\omega) = \frac{\chi_m(\omega)}{m} \sum_i \tilde{F}_i(\omega). \tag{A.19}$$

A.1.3 PSD

The power spectral density of some signal $x(t)$ is defined as

$$S_{xx}(\omega) = \lim_{\tau\to\infty} \frac{1}{\tau} \left\langle \left| \int_{-\tau/2}^{\tau/2} x(t) e^{i\omega t} dt \right|^2 \right\rangle. \tag{A.20}$$

Put in terms of Fourier space, this becomes

$$\begin{aligned}
S_{xx} &= \lim_{\tau\to\infty} \frac{1}{\tau} \left\langle \left| \int_{-\tau/2}^{\tau/2} \frac{1}{2\pi} \int_{-\infty}^{\infty} \tilde{x}(\omega') e^{-i\omega' t} d\omega' e^{i\omega t} dt \right|^2 \right\rangle && \text{(A.21)} \\
&= \lim_{\tau\to\infty} \frac{1}{(2\pi)^2\tau} \left\langle \left| \int_{-\infty}^{\infty} \tilde{x}(\omega') \int_{-\tau}^{\tau/2} e^{i(\omega-\omega')t} dt d\omega \right|^2 \right\rangle && \text{(A.22)} \\
&= \lim_{\tau\to\infty} \frac{1}{(2\pi)^2\tau} \left\langle \left| \int_{-\infty}^{\infty} \tilde{x}(\omega') \int_{-\infty}^{\infty} h_\tau(t) e^{i(\omega-\omega')t} dt d\omega' \right|^2 \right\rangle && \text{(A.23)} \\
&= \lim_{\tau\to\infty} \frac{1}{(2\pi)^2\tau} \left\langle \left| \int_{-\infty}^{\infty} \tilde{x}(\omega') \tilde{h}_\tau(\omega-\omega') d\omega' \right|^2 \right\rangle && \text{(A.24)} \\
&= \lim_{\tau\to\infty} \frac{1}{(2\pi)^2\tau} \left\langle \left| (\tilde{x} * \tilde{h}_\tau)(\omega) \right|^2 \right\rangle && \text{(A.25)}
\end{aligned}$$

where

$$h_\tau(t) = \begin{cases} 1 & |t| < \tau/2 \\ 1/2 & |t| = \tau/2 \\ 0 & \text{otherwise} \end{cases} \tag{A.26}$$

$$\begin{aligned} \implies \tilde{h}_\tau(\omega) &= \mathcal{F}\left[h_\tau(t)\right] && \text{(A.27)} \\ &= \int_{-\infty}^{\infty} h_\tau(t) e^{i\omega t} dt && \text{(A.28)} \\ &= \int_{-\tau/2}^{\tau/2} e^{i\omega t} dt && \text{(A.29)} \\ &= \frac{1}{i\omega}\left(e^{i\omega\tau/2} - e^{-i\omega\tau/2}\right) && \text{(A.30)} \\ &= \tau \mathrm{sinc}(\omega\tau/2). && \text{(A.31)} \end{aligned}$$

If we now expand Equation A.24 we can see that

$$S_{xx} = \lim_{\tau\to\infty} \frac{1}{(2\pi)^2\tau} \left\langle \int_{-\infty}^{\infty} \int_{-\infty}^{\infty} \tilde{x}(\omega')\tilde{x}^*(\omega'')\tilde{h}_\tau(\omega-\omega')\tilde{h}_\tau^*(\omega-\omega'') d\omega' d\omega'' \right\rangle. \tag{A.32}$$

We can rewrite this expression with the force terms as follows

$$S_{xx} = \lim_{\tau\to\infty} \frac{1}{(2\pi)^2\tau} \left\langle \int_{-\infty}^{\infty} \int_{-\infty}^{\infty} \tilde{h}_\tau(\omega-\omega')\tilde{h}_\tau^*(\omega-\omega'') \frac{\chi_m(\omega')\chi_m^*(\omega'')}{m^2} \sum_{i,j} \tilde{F}_i(\omega')\tilde{F}_i^*(\omega'') d\omega' d\omega'' \right\rangle. \tag{A.33}$$

We will restrict our attention to the case where $F_i(t)$ is some white noise $N_i(t)$ with

$$\begin{aligned} \left\langle N_i(t) N_j(t') \right\rangle &= S_{N_i}\delta_{ij}\delta(t-t') && \text{(A.34)} \\ \implies \left\langle \tilde{N}_i(\omega)\tilde{N}_j(\omega') \right\rangle &= \int_{-\infty}^{\infty}\int_{-\infty}^{\infty} S_{N_i}\delta_{ij}\delta(t-t') e^{i\omega t} e^{i\omega' t'} dt dt' && \text{(A.35)} \\ &= S_{N_i}\delta_{ij} \int_{-\infty}^{\infty} e^{i\omega t} e^{i\omega' t} dt && \text{(A.36)} \\ &= 2\pi S_{N_i}\delta_{ij}\delta(\omega+\omega') && \text{(A.37)} \end{aligned}$$

where S_{N_i} is the Noise Power Spectrum Density. Furthermore, we should remember that $\tilde{N}_i^*(\omega) = \tilde{N}_i(-\omega)$. Then using this, we see that

$$S_{xx} = \lim_{\tau\to\infty} \frac{1}{(2\pi)^2 m^2 \tau} \int_{-\infty}^{\infty}\int_{-\infty}^{\infty} \tilde{h}_\tau(\omega-\omega')\tilde{h}_\tau^*(\omega-\omega'')\chi_m(\omega')\chi_m^*(\omega'')\sum_{i,j} 2\pi S_{N_i}\delta_{ij}\delta(\omega'-\omega'')d\omega' d\omega'' \tag{A.38}$$

$$= \lim_{\tau\to\infty} \frac{\sum_i S_{N_i}}{2\pi m^2 \tau} \int_{-\infty}^{\infty}\int_{-\infty}^{\infty} \tilde{h}_\tau(\omega-\omega')\tilde{h}_\tau^*(\omega-\omega'')\chi_m(\omega')\chi_m^*(\omega'')\delta(\omega'-\omega'')d\omega' d\omega'' \tag{A.39}$$

$$= \lim_{\tau\to\infty} \frac{\sum_i S_{N_i}}{2\pi m^2 \tau} \int_{-\infty}^{\infty} \tilde{h}_\tau(\omega-\omega')\tilde{h}_\tau^*(\omega-\omega')\chi_m(\omega')\left|\chi_m(\omega)\right|^2 d\omega' \tag{A.40}$$

$$= \lim_{\tau\to\infty} \frac{\sum_i S_{N_i}}{2\pi m^2 \tau} \int_{-\infty}^{\infty} \left[\tau \mathrm{sinc}\left(\frac{(\omega-\omega')\tau}{2}\right)\right]^2 \left|\chi_m(\omega)\right|^2 d\omega' \tag{A.41}$$

We can then use the fact that

$$\lim_{\tau\to\infty} \tau \mathrm{sinc}^2(\tau\omega/2) = 2\pi\delta(\omega) \tag{A.42}$$

to simplify this further

$$S_{xx} = \frac{\sum_i S_{N_i}}{2\pi m^2} \int_{-\infty}^{\infty} 2\pi\delta(\omega-\omega')\chi_m(\omega')\chi_m^*(\omega')d\omega' \tag{A.43}$$

$$= \frac{\left|\chi_m(\omega)\right|^2}{m^2}\sum_i S_{N_i}. \tag{A.44}$$

We can then consider the total power in the spectrum due to these noise terms. In this case

$$\int_{-\infty}^{\infty} S_{xx}(\omega)d\omega = \int_{-\infty}^{\infty} \frac{\left|\chi_m(\omega)\right|^2}{m^2}\sum_i S_{N_i} d\omega \tag{A.45}$$

$$= \frac{\sum_i S_{N_i}}{m^2}\int_{-\infty}^{\infty} \frac{1}{(\Omega_x^2-\omega^2)^2+\gamma^2\omega^2} d\omega \tag{A.46}$$

$$= \frac{\sum_i S_{N_i}}{m^2}\frac{\pi}{\gamma\Omega_x^2}. \tag{A.47}$$

Alternatively, we can show that

$$
\begin{aligned}
\int_{-\infty}^{\infty} S_{xx}(\omega)d\omega &= \int_{-\infty}^{\infty} \lim_{\tau\to\infty} \frac{1}{\tau}\left\langle \left| \int_{-\tau/2}^{\tau/2} x(t)e^{i\omega t}dt \right|^2 \right\rangle d\omega && \text{(A.48)}\\
&= \int_{-\infty}^{\infty} \lim_{\tau\to\infty} \frac{1}{\tau}\left\langle \int_{-\tau/2}^{\tau/2}\int_{-\tau/2}^{\tau/2} x(t)e^{i\omega t}x^*(t')e^{-i\omega t'}dtdt' \right\rangle d\omega && \text{(A.49)}\\
&= \lim_{\tau\to\infty} \frac{1}{\tau}\int_{-\tau/2}^{\tau/2}\int_{-\tau/2}^{\tau/2} \left\langle x(t)x(t')\right\rangle \int_{-\infty}^{\infty} e^{i\omega(t-t')}d\omega dtdt' && \text{(A.50)}\\
&= \lim_{\tau\to\infty} \frac{1}{\tau}\int_{-\tau/2}^{\tau/2}\int_{-\tau/2}^{\tau/2} \left\langle x(t)x(t')\right\rangle 2\pi\delta(t-t')dtdt' && \text{(A.51)}\\
&= \lim_{\tau\to\infty} \frac{2\pi}{\tau}\int_{-\tau/2}^{\tau/2} \left\langle x(t)^2\right\rangle dt. && \text{(A.52)}
\end{aligned}
$$

Then, if these noise terms obey the Fluctuation Dissipation Theorem, then we may use the Equipartition Theorem for a harmonic oscillator to write

$$
\frac{1}{2}k_BT = \frac{1}{2}m\Omega_x^2\left\langle x(t)^2\right\rangle \tag{A.53}
$$

and therefore we see that

$$
\begin{aligned}
\int_{-\infty}^{\infty} S_{xx}(\omega)d\omega &= \lim_{\tau\to\infty} \frac{2\pi}{\tau}\int_{-\tau/2}^{\tau/2} \frac{k_BT}{m\Omega_x^2}dt && \text{(A.54)}\\
&= 2\pi\frac{k_BT}{m\Omega_x^2}. && \text{(A.55)}
\end{aligned}
$$

We can then put Equation A.47 and Equation A.55 together which gives us

$$
\begin{aligned}
\frac{\sum_i S_{N_i}}{m^2}\frac{\pi}{\gamma\Omega_m^2} &= 2\pi\frac{k_BT}{m\Omega_x^2} && \text{(A.56)}\\
\implies \sum_i S_{N_i} &= 2\gamma m k_BT. && \text{(A.57)}
\end{aligned}
$$

A.2 Thermal Mechanical Oscilator in Quantum Mechanics

A.2.1 Caldeira-Leggett Equation of Motion

We can write our Hamiltonian as

$$\hat{H} = \frac{\hat{p}^2}{2m} + \frac{1}{2}m\Omega_x^2\hat{x}^2 + \sum_i \frac{\hat{p}_i^2}{2m_i} + \sum_i \frac{1}{2}\frac{C_i^2}{m_i\Omega_i^2}\left(\hat{x} - \frac{m_i\Omega_i^2}{C_i}\hat{x}_i\right)^2 \tag{A.58}$$

where $\hat{x}_i$, $\hat{p}_i$, C_i, m_i, and Ω_i,are the position, momenta, coupling constants, masses and oscillator frequencies of the bath operators. We can then derive the equations of motion for our operators

$$\frac{d\hat{x}}{dt} = \frac{i}{\hbar}\left[\hat{H},\hat{x}\right] = \frac{i}{2m\hbar}\left[\hat{p}^2,\hat{x}\right] = \frac{\hat{p}}{m}, \tag{A.59}$$

$$\frac{d\hat{p}}{dt} = \frac{i}{\hbar}\left[\hat{H},\hat{p}\right] = \frac{i}{2\hbar}m\Omega_x^2\left[\hat{x}^2,\hat{p}\right] + \frac{i}{2\hbar}\sum_i \frac{C_i^2}{m_i\Omega_i^2}\left[\left(\hat{x} - \frac{m_i\Omega_i^2}{C_i}\hat{x}_i\right)^2,\hat{p}\right] = -m\Omega_x^2\hat{x} - \sum_i \frac{C_i^2}{m_i\Omega_i^2}\left(\hat{x} - \frac{m_i\Omega_i^2}{C_i}\hat{x}_i\right), \tag{A.60}$$

$$\frac{d\hat{x}_i}{dt} = \frac{i}{\hbar}\left[\hat{H},\hat{x}_i\right] = \frac{\hat{p}_i}{m_i}, \tag{A.61}$$

$$\frac{d\hat{p}_i}{dt} = \frac{i}{\hbar}\left[\hat{H},\hat{p}_i\right] = \frac{i}{2\hbar}\frac{C_i^2}{m_i\Omega_i^2}\left[\left(\hat{x} - \frac{m_i\Omega_i^2}{C_i}\hat{x}_i\right)^2,\hat{p}_i\right] = C_i\left(\hat{x} - \frac{m_i\Omega_i^2}{C_i}\hat{x}_i\right). \tag{A.62}$$

We can put these together to get

$$0 = m\ddot{\hat{x}} + m\Omega_x^2\hat{x} + \sum_i \frac{C_i^2}{m_i\Omega_i^2}\hat{x} - C_i\hat{x}_i, \tag{A.63}$$

$$0 = m_i\ddot{\hat{x}}_i + m_i\Omega_i^2\hat{x}_i - C_i\hat{x}. \tag{A.64}$$

We can solve Equation A.64 in the Laplace domain. In which case, Equation A.64 becomes

$$
\begin{aligned}
0 &= m_i\mathcal{L}\left\{\ddot{\hat{x}}_i\right\}(\omega) + m_i\Omega_i^2\mathcal{L}\left\{\hat{x}_i\right\}(\omega) - C_i\mathcal{L}\left\{\hat{x}\right\}(\omega), \qquad \text{(A.65)}\\
&= m_i\left[\omega^2\tilde{\hat{x}}_i(\omega) - \omega\hat{x}_i(0) - \dot{\hat{x}}_i(0)\right] + m_i\Omega_i^2\tilde{\hat{x}}_i(\omega) - C_i\tilde{\hat{x}}(\omega), \qquad \text{(A.66)}\\
\implies \tilde{\hat{x}}_i(\omega) &= \frac{\omega}{\omega^2+\Omega_i^2}\hat{x}_i(0) + \frac{\Omega_i}{\omega^2+\Omega_i^2}\frac{\dot{\hat{x}}_i(0)}{\Omega_i} + \left(1 - \frac{\omega^2}{\omega^2+\Omega_i^2}\right)\tilde{\hat{x}}(\omega)\frac{C_i}{m_i\Omega_i^2}, \qquad \text{(A.67)}\\
\implies \hat{x}_i(t) &= \cos(\Omega_i t)\hat{x}_i(0) + \sin(\Omega_i t)\frac{\dot{\hat{x}}_i(0)}{\Omega_i} + \frac{C_i}{m_i\Omega_i^2}\left[\hat{x}(t) - \mathcal{L}^{-1}\left\{\frac{\omega^2}{\omega^2+\Omega_i^2}\tilde{\hat{x}}(\omega)\right\}\right], \qquad \text{(A.68)}\\
&= \hat{x}_i^{(0)}(t) + \frac{C_i}{m_i\Omega_i^2}\left[\hat{x}(t) - \frac{d}{dt}\mathcal{L}^{-1}\left\{\frac{\omega}{\omega^2+\Omega_i^2}\tilde{\hat{x}}(\omega)\right\}\right], \qquad \text{(A.69)}\\
&= \hat{x}_i^{(0)}(t) + \frac{C_i}{m_i\Omega_i^2}\left[\hat{x}(t) - \frac{d}{dt}\mathcal{L}^{-1}\left\{\mathcal{L}\left\{\cos(\Omega_i t)\right\}\tilde{\hat{x}}(\omega)\right\}\right], \qquad \text{(A.70)}\\
&= \hat{x}_i^{(0)}(t) + \frac{C_i}{m_i\Omega_i^2}\left[\hat{x}(t) - \frac{d}{dt}\int_0^t \cos(\Omega_i(t-t'))\hat{x}(t')dt'\right], \qquad \text{(A.71)}\\
&= \hat{x}_i^{(0)}(t) + \frac{C_i}{m_i\Omega_i^2}\left[\hat{x}(t) - \frac{d}{dt}\int_{-\infty}^t \cos(\Omega_i(t-t'))\hat{x}(t')dt'\right], \qquad \text{(A.72)}
\end{aligned}
$$

where we have introduced

$$\hat{x}_i^{(0)}(t) = \hat{x}_i(0)\cos(\Omega_i t) + \frac{\hat{p}_i(0)}{m_i\Omega_i}\sin(\Omega_i t) \tag{A.73}$$

for ease of use. Also note in the last step I extended the range of integration from $[0,t] \to (-\infty,t]$. As we will see later, this makes no difference in our treatment but does serve to unify different version of this calculation. If we plug $\hat{x}_i$ into Equation A.63, we get

$$0 = m\ddot{\hat{x}} + m\Omega_x^2\hat{x} - \sum_i C_i\hat{x}_i^{(0)}(t) + \frac{d}{dt}\int_{-\infty}^t \sum_i \frac{C_i^2}{m_i\Omega_i^2}\cos(\Omega_i(t-t'))\hat{x}(t')dt'. \tag{A.74}$$

We will now focus on the last term. Let us call $\mu(t) = \sum_i \frac{C_i^2}{m_i\Omega_i^2}\cos(\Omega_i t)$ our memory kernel.The memory kernel is labelled as such as it sets quantifies the influence of past bath interactions on the current particle motion and in this was sets the time scale over which the bath force decorrelates. If we call $k_i = C_i^2/m_i\Omega_i^2$, we can make the change from a discrete to a continuous representation of the memory kernel by introducing a density function $\rho(\Omega)$ in which case

$$\mu(t) = \sum_i k_i \cos(\Omega_i t) = \int_0^\infty d\Omega\rho(\Omega)k(\omega)\cos(\Omega t). \tag{A.75}$$

We will then shift the derivative inside the integral using the Leibniz integral rule in which case

$$\frac{d}{dt}\int_{-\infty}^{t}\mu(t-t')\hat{x}(t')dt' = \int_{-\infty}^{t}\frac{\partial}{\partial t}\left(\mu(t-t')\hat{x}(t')\right)dt' + \left.\left(\mu(t-t')\hat{x}(t')\frac{d}{dt}t\right)\right|_{t'=t}, \tag{A.76}$$

$$= \int_{-\infty}^{t}\frac{\partial}{\partial t}\left(\mu(t-t')\hat{x}(t')\right)dt' + \mu(0)\hat{x}(t). \tag{A.77}$$

To proceed, we'll make a change of variables to $u = t - t'$ in which case

$$\frac{d}{dt}\int_{-\infty}^{t}\mu(t-t')\hat{x}(t')dt' = \int_{\infty}^{0}\left(\frac{\partial u}{\partial t}\frac{\partial}{\partial u}\mu(u)\right)\hat{x}(t-u)\left(\frac{du}{dt'}\right)^{-1}du + \mu(0)\hat{x}(t), \tag{A.78}$$

$$= \int_{0}^{\infty}\left(\frac{\partial}{\partial u}\mu(u)\right)\hat{x}(t-u)du + \mu(0)\hat{x}(t), \tag{A.79}$$

$$= \mu(u)\hat{x}(t-u)|_{u=0}^{u=\infty} - \int_{0}^{\infty}\mu(u)\left(\frac{\partial}{\partial u}\hat{x}(t-u)\right)du + \mu(0)\hat{x}(t), \tag{A.80}$$

$$= \lim_{u\to\infty}\mu(u)\hat{x}(-u) - \int_{0}^{\infty}\mu(u)\left(\frac{\partial}{\partial u}\hat{x}(t-u)\right)du, \tag{A.81}$$

$$= -\int_{0}^{\infty}\mu(u)\left(\frac{\partial}{\partial u}\hat{x}(t-u)\right)du, \tag{A.82}$$

$$= -\int_{t}^{-\infty}\mu(t-t')\left(\frac{\partial t'}{\partial u}\frac{\partial}{\partial t'}\hat{x}(t')\right)\left(\frac{dt'}{du}\right)^{-1}dt', \tag{A.83}$$

$$= \int_{-\infty}^{t}\mu(t-t')\dot{\hat{x}}(t')dt'. \tag{A.84}$$

To proceed, we will work in the Fourier domain.

$$\begin{aligned}
\mathcal{F}\left\{\int_{-\infty}^{t}\mu(t-t')\dot{\hat{x}}(t')dt'\right\} &= \mathcal{F}\left\{\int_{-\infty}^{\infty}\Theta(t-t')\mu(t-t')\dot{\hat{x}}(t')dt'\right\}, \tag{A.85}\\
&= \mathcal{F}\left\{\left([\Theta\mu]*\dot{\hat{x}}\right)(t)\right\}, \tag{A.86}\\
&= \mathcal{F}\left\{\Theta\mu]\right\}\mathcal{F}\left\{\dot{\hat{x}}\right\}, \tag{A.87}\\
&= \left(\mathcal{F}\left\{\Theta\right\}*\mathcal{F}\left\{\mu\right\}\right)(\omega)\mathcal{F}\left\{\dot{\hat{x}}\right\}, \tag{A.88}\\
&= \int_0^\infty d\Omega\rho(\Omega)k(\Omega)\left(\mathcal{F}\left\{\Theta\right\}*\mathcal{F}\left\{\cos\Omega t\right\}\right)(\omega)(-i\omega\tilde{\hat{x}}(\omega)), \tag{A.89}\\
&= -i\omega\tilde{\hat{x}}\int_0^\infty d\Omega\rho(\Omega)k(\Omega)\int_{-\infty}^{\infty}d\omega'\left[\frac{\delta(\omega-\omega')}{2}+\frac{i}{\omega-\omega'}\right]\left[\frac{\delta(\omega'-\Omega)+\delta(\omega'+\Omega)}{2}\right], \tag{A.90}\\
&= \frac{-i}{2}\omega\tilde{\hat{x}}\int_0^\infty d\Omega\rho(\Omega)k(\Omega)\left(\frac{\delta(\omega-\Omega)}{2}+\frac{i}{\omega-\Omega}+\frac{\delta(\omega+\Omega)}{2}+\frac{i}{\omega+\Omega}\right), \tag{A.91}\\
&= \frac{-i}{2}\omega\tilde{\hat{x}}\left[\frac{\rho(\omega)k(\omega)}{2}+\int_0^\infty d\Omega\rho(\Omega)k(\Omega)\left(\frac{i}{\omega-\Omega}+\frac{i}{\omega+\Omega}\right)\right], \tag{A.92}\\
&= \frac{-i}{2}\omega\tilde{\hat{x}}\left[\frac{\rho(\omega)k(\omega)}{2}+\frac{2i}{\omega}\int_0^\infty d\Omega\rho(\Omega)k(\Omega)\frac{1}{1-(\Omega/\omega)^2}\right], \tag{A.93}\\
&\approx \left[-i\omega\frac{\rho(\omega)k(\omega)}{4}+\int_0^\infty d\Omega\rho(\Omega)k(\Omega)\right]\tilde{\hat{x}}(\omega), \tag{A.94}\\
&= \left[-im\omega\tilde{\gamma}(\omega)+k_{\text{bath}}\right]\tilde{\hat{x}}(\omega), \tag{A.95}
\end{aligned}$$

where we have just labelled $\tilde{\gamma}(\omega)=\rho(\omega)k(\omega)/4m$ and $k_{\text{bath}}=\int_0^\infty d\Omega\rho(\Omega)k(\Omega)$. In principle we should extend $k_{\text{bath}}\to k_{\text{bath}}(\omega)$ as well to account for all the terms in the integral but we usually consider the bath to fall off at some energy in which case our approximation stands for non-DC phenomena. We now invert this Fourier transform to arrive at

$$\frac{d}{dt}\int_{-\infty}^{t}\sum_i \frac{C_i^2}{m_i\Omega_i^2}\cos(\Omega_i(t-t'))\hat{x}(t')dt' \approx \mathcal{F}^{-1}\left\{\left[-im\omega\tilde{\gamma}(\omega)+k_{\text{bath}}\right]\tilde{\hat{x}}\right\}(t), \tag{A.96}$$

$$= k_{\text{bath}}\hat{x}(t) + (\gamma * \dot{\hat{x}})(t), \tag{A.97}$$

$$= k_{\text{bath}}\hat{x}(t) + \int_{-\infty}^{t}\gamma(t-t')\dot{\hat{x}}(t')dt', \tag{A.98}$$

where I have set the upper bound on the convolution to t so that future interactions don't backpropagate in time and break causality. We can then substitute this back into Equation A.74 and find that

$$F(t) = m\ddot{\hat{x}} + m{\Omega'_x}^2\hat{x} + k_{\text{bath}}\hat{x} + \int_{-\infty}^{t}\gamma(t-t')\dot{\hat{x}}(t')dt', \tag{A.99}$$

where I have defined $F(t) = \sum_i C_i\hat{x}_i^{(0)}(t)$ and ${\Omega'_x}^2 = \Omega_x^2 + k_{\text{bath}}/m$. We can now see that the effect of the memory kernel is to shift the oscillator frequency as well as damp its motion. If we make the first Markov approximation [42] $\gamma(t) = \gamma\delta(t)$, then we recover the classical form for the oscillator

$$F(t) = m\ddot{\hat{x}} + m{\Omega'_x}^2\hat{x} + \gamma\dot{\hat{x}}, \tag{A.100}$$

albeit with a shifted frequency. This approximation removes any memory in the bath which results in our white-noise process as expected.

Appendix B

Tight Focusing

Following [100], we find the field of an arbitrarily polarized guassian beam just after it passes through a microscope objective is

$$\vec{E}_\infty(\theta,\phi) = \left(\vec{E}_{\text{in}}(\theta,\phi)\cdot\begin{bmatrix}-\sin\phi\\ \cos\phi\\ 0\end{bmatrix}\right)\cdot\begin{bmatrix}-\sin\phi\\ \cos\phi\\ 0\end{bmatrix}\sqrt{\cos\theta} + \left(\vec{E}_{\text{in}}(\theta,\phi)\cdot\begin{bmatrix}\cos\phi\\ \sin\phi\\ 0\end{bmatrix}\right)\cdot\begin{bmatrix}\cos\phi\cos\theta\\ \sin\phi\cos\theta\\ -\sin\theta\end{bmatrix}\sqrt{\cos\theta}, \tag{B.1}$$

$$= |\vec{E}_{\text{in}}(\theta)|\sqrt{\cos\theta}\left(\begin{bmatrix}e_x\sin^2\phi - e_y\sin\phi\cos\phi\\ -e_x\sin\phi\cos\phi + e_y\cos^2\phi\\ 0\end{bmatrix} + \begin{bmatrix}(e_x\cos^2\phi + e_y\sin\phi\cos\phi)\cos\theta\\ (e_x\sin\phi\cos\phi + e_y\sin^2\phi)\cos\theta\\ -(e_x\cos\phi + e_y\sin\phi)\sin\theta\end{bmatrix}\right) \tag{B.2}$$

where we are working in spherical coordinates and $e_i = \hat{i}\cdot\frac{\vec{E}_{\text{in}}}{|\vec{E}_{\text{in}}|}$ is the component of the polarization along the i-th direction. Interestingly, we see that in principle, we can have a component along the propagation of the beam which is typically not present in paraxial optics. I have also removed the dependence of the incoming electric field on ϕ since we are dealing with a gaussian beam which is cylindrically symmetric. If we then propagate this field to the focal plane of the microscope objective, we can write out the electric field in cylindrical coordinates as

$$\vec{E}(\rho,\phi,z) = \frac{ikf}{2\pi}e^{-ikf}\int_0^{\theta_{\max}}\int_0^{2\pi} E_\infty(\theta',\phi')e^{ikz\cos\theta'}e^{ik\rho\sin\theta'\cos(\phi'-\phi)}\sin\theta' d\phi' d\theta', \tag{B.3}$$

where $\theta_{\max} = \sin^{-1}(\text{NA})$ relates the size of the lens to the maximal ray angle.

We can do this integral by noting that

$$\frac{1}{2\pi}\int_0^{2\pi}\cos n\phi e^{ix\cos(\phi'-\phi)}d\phi' = i^n J_n(x)\cos n\phi, \tag{B.4}$$

$$\frac{1}{2\pi}\int_0^{2\pi}\sin n\phi e^{ix\cos(\phi'-\phi)}d\phi' = i^n J_n(x)\sin n\phi \tag{B.5}$$

where J_n are Bessel functions of the first kind. Then

$$\vec{E}(\rho,\phi,z) = ikfe^{-ikf}\int_0^{\theta_{\max}} |\vec{E}_{\text{in}}(\theta')|\sqrt{\cos\theta'}e^{ikz\cos\theta'}\sin\theta'\vec{I}_\phi(\theta')d\theta', \tag{B.6}$$

$$\vec{I}_\phi(\theta) = \frac{1}{2\pi}\int_0^{2\pi}\begin{bmatrix} e_x\sin^2\phi' - e_y\sin\phi'\cos\phi' + (e_x\cos^2\phi' + e_y\sin\phi\cos\phi')\cos\theta \\ -e_x\sin\phi'\cos\phi' + e_y\cos^2\phi' + (e_x\sin\phi'\cos\phi' + e_y\sin^2\phi')\cos\theta \\ -(e_x\cos\phi' + e_y\sin\phi')\sin\theta \end{bmatrix} e^{ik\rho\sin\theta\cos(\phi'-\phi)}d\phi', \tag{B.7}$$

$$= \frac{1}{4\pi}\int_0^{2\pi}\begin{bmatrix} e_x(1-\cos2\phi') - e_y\sin2\phi' + (e_x(1+\cos2\phi') + e_y\sin2\phi')\cos\theta \\ -e_x\sin2\phi' + e_y(1+\cos2\phi') + (e_x\sin2\phi' + e_y(1-\cos2\phi'))\cos\theta \\ -2(e_x\cos\phi' + e_y\sin\phi')\sin\theta \end{bmatrix} e^{ik\rho\sin\theta\cos(\phi'-\phi)}d\phi', \tag{B.8}$$

$$= \frac{1}{4\pi}\int_0^{2\pi}\begin{bmatrix} e_x(1+\cos\theta) - e_x(1-\cos\theta)\cos2\phi' - e_y(1-\cos\theta)\sin2\phi' \\ e_y(1+\cos\theta) + e_y(1-\cos\theta)\cos2\phi' - e_x(1-\cos\theta)\sin2\phi' \\ -2e_x\sin\theta\cos\phi' - 2e_y\sin\theta\sin\phi' \end{bmatrix} e^{ik\rho\sin\theta\cos(\phi'-\phi)}d\phi', \tag{B.9}$$

$$= \frac{1}{2}\begin{bmatrix} e_x(1+\cos\theta)J_0(k\rho\sin\theta) + (e_x\cos2\phi + e_y\sin2\phi)(1-\cos\theta)J_2(k\rho\sin\theta) \\ e_y(1+\cos\theta)J_0(k\rho\sin\theta) + (e_x\sin2\phi - e_y\cos2\phi)(1-\cos\theta)J_2(k\rho\sin\theta) \\ -2i(e_x\sin\theta\cos\phi + e_y\sin\theta\sin\phi)J_1(k\rho\sin\theta) \end{bmatrix}, \tag{B.10}$$

$$\Longrightarrow \vec{E}(\rho,\phi,z) = \frac{ikf}{2}e^{-ikf}\begin{bmatrix} e_xI_0(\rho,z) + (e_x\cos2\phi + e_y\sin2\phi)I_2(\rho,z) \\ e_yI_0(\rho,z) + (e_x\sin2\phi - e_y\cos2\phi)I_2(\rho,z) \\ -2i(e_x\cos\phi + e_y\sin\phi)I_1(\rho,z) \end{bmatrix}, \tag{B.11}$$

$$I_0(\rho,z) = \int_0^{\theta_{\max}} |\vec{E}_{\text{in}}(\theta')|\sqrt{\cos\theta'}(1+\cos\theta')J_0(k\rho\sin\theta')e^{ikz\cos\theta'}\sin\theta'd\theta', \tag{B.12}$$

$$I_1(\rho,z) = \int_0^{\theta_{\max}} |\vec{E}_{\text{in}}(\theta')|\sqrt{\cos\theta'}J_1(k\rho\sin\theta')e^{ikz\cos\theta'}\sin^2\theta'd\theta', \tag{B.13}$$

$$I_2(\rho,z) = \int_0^{\theta_{\max}} |\vec{E}_{\text{in}}(\theta')|\sqrt{\cos\theta'}(1-\cos\theta')J_2(k\rho\sin\theta')e^{ikz\cos\theta'}\sin\theta'd\theta'. \tag{B.14}$$

To simplify things further, we can numerically integrate these terms. However, to get a more satisfying result, we will expand these integrals in powers of ρ and z. First, we will note that if we take a gaussian beam and overfill the aperture of the lens we can write the incoming field as

$$|\vec{E}_{\text{in}}(\theta)| = E_0 e^{-\frac{f^2}{w_0^2}\sin^2\theta} = E_0 e^{-\frac{1}{f_0^2}\frac{\sin^2\theta}{\sin^2\theta_{\max}}} = E_0 f_w(\theta) \tag{B.15}$$

where $f_0 = \frac{w_0}{f\sin\theta_{\max}}$ is the filling factor of the lens with $\theta_{\max} = \sin^{-1}\text{NA}$ and $f_w(\theta)$ is called the apodization function. We can then expand the bessel functions in powers of ρ as

$$J_\alpha(x) = \sum_{\beta=0}^{\infty} \frac{(-1)^\beta}{\beta!(\alpha+\beta)!}\left(\frac{x}{2}\right)^{\alpha+2\beta}, \tag{B.16}$$

$$\implies J_0(x) \approx 1 - \left(\frac{x}{2}\right)^2, \tag{B.17}$$

$$\implies J_1(x) \approx \frac{x}{2}, \tag{B.18}$$

$$\implies J_2(x) \approx \frac{1}{2}\left(\frac{x}{2}\right)^2. \tag{B.19}$$

Lastly, we can expand the exponentials in powers of z to get

$$I_0(\rho,z) \approx E_0 \int_0^{\theta_{\max}} f_w(\theta)\sqrt{\cos\theta'}(1+\cos\theta')\left[1-\left(\frac{k\rho\sin\theta'}{2}\right)^2\right]\left[1+ikz\cos\theta'-\frac{k^2z^2}{2}\cos^2\theta'\right]\sin\theta' d\theta', \tag{B.20}$$

$$\approx E_0\left[i_0+i_1k^2\rho^2+i_2kz+i_3k^2z^2\right], \tag{B.21}$$

$$I_1(\rho,z) \approx E_0 \int_0^{\theta_{\max}} f_w(\theta)\sqrt{\cos\theta'}\left[\frac{k\rho\sin\theta'}{2}\right]\left[1+ikz\cos\theta'-\frac{k^2z^2}{2}\cos^2\theta'\right]\sin^2\theta' d\theta', \tag{B.22}$$

$$\approx E_0\left[i_4k\rho+i_5k^2\rho z\right], \tag{B.23}$$

$$I_2(\rho,z) \approx E_0 \int_0^{\theta_{\max}} f_w(\theta)\sqrt{\cos\theta'}(1-\cos\theta')\left[\frac{1}{2}\left(\frac{k\rho\sin\theta'}{2}\right)^2\right]\left[1+ikz\cos\theta'-\frac{k^2z^2}{2}\cos^2\theta'\right]\sin\theta' d\theta', \tag{B.24}$$

$$\approx E_0\left[i_6k^2\rho^2\right], \tag{B.25}$$

$$\tag{B.26}$$

where

$$i_0 = \int_0^{\theta_{\max}} f_w(\theta)\sqrt{\cos\theta'}(1+\cos\theta')\sin\theta' d\theta', \tag{B.27}$$

$$i_1 = -\frac{1}{4}\int_0^{\theta_{\max}} f_w(\theta)\sqrt{\cos\theta'}(1+\cos\theta')\sin^3\theta' d\theta', \tag{B.28}$$

$$i_2 = i\int_0^{\theta_{\max}} f_w(\theta)\sqrt{\cos\theta'}(1+\cos\theta')\cos\theta'\sin\theta' d\theta', \tag{B.29}$$

$$i_3 = -\frac{1}{2}\int_0^{\theta_{\max}} f_w(\theta)\sqrt{\cos\theta'}(1+\cos\theta')\cos^2\theta'\sin\theta' d\theta', \tag{B.30}$$

$$i_4 = \frac{1}{2}\int_0^{\theta_{\max}} f_w(\theta)\sqrt{\cos\theta'}\sin^3\theta' d\theta', \tag{B.31}$$

$$i_5 = \frac{i}{2}\int_0^{\theta_{\max}} f_w(\theta)\sqrt{\cos\theta'}\cos\theta'\sin^3\theta' d\theta', \tag{B.32}$$

$$i_6 = \frac{1}{8}\int_0^{\theta_{\max}} f_w(\theta)\sqrt{\cos\theta'}(1-\cos\theta')\sin^3\theta' d\theta'. \tag{B.33}$$

Putting this all together, we get that

$$\vec{E}(\rho,\phi,z) = \frac{ikf}{2}E_0 e^{-ikf}\begin{bmatrix} e_x i_0 + \left[e_x(i_1 + i_6\cos 2\phi) + e_y i_6 \sin 2\phi\right]k^2\rho^2 + e_x i_2 kz + e_x i_3 k^2 z^2 \\ e_y i_0 + \left[e_y(i_1 - i_6\cos 2\phi) + e_x i_6 \sin 2\phi\right]k^2\rho^2 + e_y i_2 kz + e_y i_3 k^2 z^2 \\ -2i(e_x\cos\phi + e_y\sin\phi)(i_4 k\rho + i_5 k^2\rho z) \end{bmatrix}. \tag{B.34}$$

Using Equation 2.4 we can write out the potential up to the quadratic terms to get

$$\begin{aligned} U(\rho,z) &= -\frac{1}{2}\alpha|\vec{E}(\rho,\phi,z)|^2 \qquad \text{(B.35)} \\ &\approx -\frac{1}{2}\alpha\frac{k^2f^2}{4}E_0^2\left[i_0^2 + (2i_0i_3 + |i_2|^2)k^2z^2\right. \\ &+ \left(2i_0i_1 + 2(|e_x|^2 - |e_y|^2)i_0i_6\cos 2\phi + 2(e_xe_y^* + e_x^*e_y)i_0i_6\sin 2\phi\right)k^2\rho^2 \\ &\left.+4(|e_x|^2 i_4^2\cos^2\phi + |e_y|^2 i_4^2 \sin^2\phi + (e_xe_y^* + e_x^*e_y)i_4^2\cos\phi\sin\phi)k^2\rho^2\right]. \qquad \text{(B.36)} \end{aligned}$$

We can switch to cartesian coordinates with $x = \rho\cos\phi$ and $y = \rho\sin\phi$ which gives

$$\begin{aligned} U(x,y,z) &\approx -\frac{1}{2}\alpha\frac{k^2f^2}{4}E_0^2\left[i_0^2 + (2i_0i_3 + |i_2|^2)k^2z^2 + 2i_0i_1k^2(x^2+y^2)\right. \\ &+ 2(|e_x|^2 - |e_y|^2)i_0i_6k^2(x^2-y^2) + 4(e_xe_y^* + e_x^*e_y)i_0i_6k^2xy \\ &\left.+4|e_x|^2i_4^2k^2x^2 + 4|e_y|^2i_4^2k^2y^2 + 4(e_xe_y^* + e_x^*e_y)i_4^2k^2xy\right], \qquad \text{(B.37)} \\ &= -\frac{1}{2}\alpha\frac{k^2f^2}{4}E_0^2\left[i_0^2 + (2i_0i_3 + |i_2|^2)k^2z^2 + 4(e_xe_y^* + e_x^*e_y)(i_0i_6 + i_4^2)k^2xy\right. \\ &+ 2(i_0i_1 + (|e_x|^2 - |e_y|^2)i_0i_6 + 2|e_x|^2i_4^2)k^2x^2 \\ &\left.+2(i_0i_1 + (|e_y|^2 - |e_x|^2)i_0i_6 + 2|e_y|^2i_4^2)k^2y^2\right]. \qquad \text{(B.38)} \end{aligned}$$

We can then identify our mechanical frequencies as

$$\omega_x = \sqrt{\frac{\alpha P_0}{mnc\epsilon_0}\frac{k^2 f^2}{\pi w_0^2}((|e_y|^2 - |e_x|^2)i_0 i_6 - i_0 i_1 - 2|e_x|^2 i_4^2)k}, \tag{B.39}$$

$$= \sqrt{\frac{\alpha P_0}{m\pi nc\epsilon_0}(|e_y|^2 - |e_x|^2)i_0 i_6 - i_0 i_1 - 2|e_x|^2 i_4^2)}\frac{k^2}{f_0 \mathrm{NA}}, \tag{B.40}$$

$$\omega_y = \sqrt{\frac{\alpha P_0}{m\pi nc\epsilon_0}(|e_x|^2 - |e_y|^2)i_0 i_6 - i_0 i_1 - 2|e_y|^2 i_4^2)}\frac{k^2}{f_0 \mathrm{NA}}, \tag{B.41}$$

$$\omega_z = \sqrt{\frac{\alpha P_0}{m\pi nc\epsilon_0}\frac{1}{2}(-2i_0 i_3 - |i_2|^2)}\frac{k^2}{f_0 \mathrm{NA}}. \tag{B.42}$$

Note how the degeneracy of ω_x and ω_y is now broken depending on the polarization of the incoming light field. This has important consequences later as we try to selectively interact with a single mechanical mode.

Appendix C

Linear Coupling Solution

Let us assume the Hamiltonians governing the mechanics and optics to be that of Equations 2.21 and 3.10. Let us then assume they are linearly coupled through the Hamiltonian

$$\hat{H}_{\text{linear}} \approx \hbar g \left(\hat{b} + \hat{b}^{\dagger}\right)\left(\hat{a} + \hat{a}^{\dagger}\right). \tag{C.1}$$

The equations of motion for our system operators become

$$\dot{\hat{a}} \approx -\left(\frac{\kappa}{2} + i\Delta'\right)\hat{a} + \sqrt{\kappa}\hat{a}_{\text{In}} - ig\left(\hat{b} + \hat{b}^{\dagger}\right) \tag{C.2}$$

$$\dot{\hat{b}} \approx -\left(\frac{\gamma}{2} + i\Omega_x'\right)\hat{b} + \sqrt{\gamma}\hat{b}_{\text{In}} - ig\left(\hat{a} + \hat{a}^{\dagger}\right) \tag{C.3}$$

where I have switched to an input-output formalism for the mechanics after we showed the dynamics to be the same. We can easily solve these coupled Langevin equations in the Fourier domain whereby we can encode this system of equations into the linear form

$$\begin{pmatrix} \sqrt{\kappa}\chi_l(\omega)\tilde{a}_{\text{In}}(\omega) \\ \sqrt{\kappa}\chi_l^*(-\omega)\tilde{a}_{\text{In}}^{\dagger}(\omega) \\ \sqrt{\gamma}\chi_m(\omega)\tilde{b}_{\text{In}}(\omega) \\ \sqrt{\gamma}\chi_m^*(-\omega)\tilde{b}_{\text{In}}^{\dagger}(\omega) \end{pmatrix} = \begin{pmatrix} 1 & 0 & ig\chi_l(\omega) & ig\chi_l(\omega) \\ 0 & 1 & -ig\chi_l^*(-\omega) & -ig\chi_l^*(-\omega) \\ ig\chi_m(\omega) & ig\chi_m(\omega) & 1 & 0 \\ -ig\chi_m^*(-\omega) & -ig\chi_m^*(-\omega) & 0 & 1 \end{pmatrix} \begin{pmatrix} \tilde{a}(\omega) \\ \tilde{a}^{\dagger}(\omega) \\ \tilde{b}(\omega) \\ \tilde{b}^{\dagger}(\omega) \end{pmatrix}. \tag{C.4}$$

and inverting this gives

$$\begin{aligned}
\frac{\tilde{a}(\omega)}{\nu(\omega)} &= \chi_l(\omega)\sqrt{\kappa}\tilde{a}_{\mathrm{In}}(\omega) \\
&\quad - ig\chi_l(\omega)\sqrt{\gamma}\left[\chi_m(\omega)\tilde{b}_{\mathrm{In}}(\omega) + \chi_m^*(-\omega)\tilde{b}_{\mathrm{In}}^\dagger(\omega)\right] \\
&\quad - g^2\chi_l(\omega)\chi_l^*(-\omega)\left[\chi_m(\omega) - \chi_m^*(-\omega)\right]\sqrt{\kappa}\left[\tilde{a}_{\mathrm{In}}(\omega) + \tilde{a}_{\mathrm{In}}^\dagger(\omega)\right] \\
\frac{\tilde{a}^\dagger(\omega)}{\nu(\omega)} &= \chi_l^*(-\omega)\sqrt{\kappa}\tilde{a}_{\mathrm{In}}^\dagger(\omega) \\
&\quad + ig\chi_l^*(-\omega)\sqrt{\gamma}\left[\chi_m(\omega)\tilde{b}_{\mathrm{In}}(\omega) + \chi_m^*(-\omega)\tilde{b}_{\mathrm{In}}^\dagger(\omega)\right] \\
&\quad + g^2\chi_l(\omega)\chi_l^*(-\omega)\left[\chi_m(\omega) - \chi_m^*(-\omega)\right]\sqrt{\kappa}\left[\tilde{a}_{\mathrm{In}}(\omega) + \tilde{a}_{\mathrm{In}}^\dagger(\omega)\right] \\
\frac{\tilde{b}(\omega)}{\nu(\omega)} &= \chi_m(\omega)\sqrt{\gamma}\tilde{b}_{\mathrm{In}}(\omega) \\
&\quad - ig\chi_m(\omega)\sqrt{\kappa}\left[\chi_l(\omega)\tilde{a}_{\mathrm{In}}(\omega) + \chi_l^*(-\omega)\tilde{a}_{\mathrm{In}}^\dagger(\omega)\right] \\
&\quad - g^2\chi_m(\omega)\chi_m^*(-\omega)\left[\chi_l(\omega) - \chi_l^*(-\omega)\right]\sqrt{\gamma}\left[\tilde{b}_{\mathrm{In}}(\omega) + \tilde{b}_{\mathrm{In}}^\dagger(\omega)\right] \\
\frac{\tilde{b}^\dagger(\omega)}{\nu(\omega)} &= \chi_m^*(-\omega)\sqrt{\gamma}\tilde{b}_{\mathrm{In}}^\dagger(\omega) \\
&\quad + ig\chi_m^*(-\omega)\sqrt{\kappa}\left[\chi_l(\omega)\tilde{a}_{\mathrm{In}}(\omega) + \chi_l^*(-\omega)\tilde{a}_{\mathrm{In}}^\dagger(\omega)\right] \\
&\quad + g^2\chi_m(\omega)\chi_m^*(-\omega)\left[\chi_l(\omega) - \chi_l^*(-\omega)\right]\sqrt{\gamma}\left[\tilde{b}_{\mathrm{In}}(\omega) + \tilde{b}_{\mathrm{In}}^\dagger(\omega)\right]
\end{aligned} \tag{C.5}$$

where $\nu(\omega) = \frac{1}{1+g^2(\chi_l(\omega)-\chi_l^*(-\omega))(\chi_m(\omega)-\chi_m^*(-\omega))}$. Note that $\nu(\omega) = \nu^*(-\omega)$. We compute all of the correlation terms.

$$\left\langle \tilde{a}(\omega)\tilde{a}_{\mathrm{In}}(\omega') \right\rangle = 0 \tag{C.6}$$

$$\left\langle \tilde{a}^\dagger(\omega)\tilde{a}_{\mathrm{In}}(\omega') \right\rangle = 0 \tag{C.7}$$

$$\left\langle \tilde{a}_{\mathrm{In}}^\dagger(\omega)\tilde{a}(\omega') \right\rangle = 0 \tag{C.8}$$

$$\left\langle \tilde{a}_{\mathrm{In}}^\dagger(\omega)\tilde{a}^\dagger(\omega') \right\rangle = 0 \tag{C.9}$$

$$\left\langle \tilde{a}_{\mathrm{In}}(\omega)\tilde{a}(\omega')\right\rangle = g^2\chi_l^*(\omega)\chi_l(-\omega)\left[\chi_m^*(\omega)-\chi_m(-\omega)\right]\nu^*(\omega)\sqrt{\kappa}\delta(\omega+\omega') \tag{C.10}$$

$$\left\langle \tilde{a}^\dagger(\omega)\tilde{a}^\dagger_{\mathrm{In}}(\omega')\right\rangle = g^2\chi_l(\omega)\chi_l^*(-\omega)\left[\chi_m(\omega)-\chi_m^*(-\omega)\right]\nu(\omega)\sqrt{\kappa}\delta(\omega+\omega') \tag{C.11}$$

$$\left\langle \tilde{a}(\omega)\tilde{a}^\dagger_{\mathrm{In}}(\omega')\right\rangle = \left[\chi_l(\omega)-g^2\chi_l(\omega)\chi_l^*(-\omega)\left(\chi_m(\omega)-\chi_m^*(-\omega)\right)\right]\nu(\omega)\sqrt{\kappa}\delta(\omega+\omega') \tag{C.12}$$

$$\left\langle \tilde{a}_{\mathrm{In}}(\omega)\tilde{a}^\dagger(\omega')\right\rangle = \left[\chi_l^*(\omega)-g^2\chi_l^*(\omega)\chi_l(-\omega)\left(\chi_m^*(\omega)-\chi_m(-\omega)\right)\right]\nu^*(\omega)\sqrt{\kappa}\delta(\omega+\omega') \tag{C.13}$$

$$\begin{aligned}\left\langle \tilde{a}(\omega)\tilde{a}(\omega')\right\rangle = {} & g^2|\chi_l(\omega)|^2\chi_l(-\omega)\left[\chi_m^*(\omega)-\chi_m(-\omega)\right]|\nu(\omega)|^2\kappa\delta(\omega+\omega') \\ & - g^4|\chi_l(\omega)|^2|\chi_l(-\omega)|^2\left|\chi_m(\omega)-\chi_m^*(-\omega)\right|^2|\nu(\omega)|^2\kappa\delta(\omega+\omega') \\ & - g^2\chi_l(\omega)\chi_l(-\omega)\left[|\chi_m(\omega)|^2(\bar{N}+1)+|\chi_m(-\omega)|^2\bar{N}\right]|\nu(\omega)|^2\gamma\delta(\omega+\omega')\end{aligned} \tag{C.14}$$

$$\begin{aligned}\left\langle \tilde{a}^\dagger(\omega)\tilde{a}^\dagger(\omega')\right\rangle = {} & g^2|\chi_l(\omega)|^2\chi_l^*(-\omega)\left[\chi_m(\omega)-\chi_m^*(-\omega)\right]|\nu(\omega)|^2\kappa\delta(\omega+\omega') \\ & - g^4|\chi_l(\omega)|^2|\chi_l(-\omega)|^2\left|\chi_m(\omega)-\chi_m^*(-\omega)\right|^2|\nu(\omega)|^2\kappa\delta(\omega+\omega') \\ & - g^2\chi_l^*(\omega)\chi_l^*(-\omega)\left[|\chi_m(\omega)|^2(\bar{N}+1)+|\chi_m(-\omega)|^2\bar{N}\right]|\nu(\omega)|^2\gamma\delta(\omega+\omega')\end{aligned} \tag{C.15}$$

$$\tag{C.16}$$

$$\begin{aligned}\left\langle \tilde{a}(\omega)\tilde{a}^\dagger(\omega')\right\rangle = {} & |\nu(\omega)|^2|\chi_l(\omega)|^2\left[\kappa\right. \\ & - g^2\chi_l(-\omega)\left[\chi_m^*(\omega)-\chi_m(-\omega)\right]\kappa \\ & - g^2\chi_l^*(-\omega)\left[\chi_m(\omega)-\chi_m^*(-\omega)\right]\kappa \\ & + g^4|\chi_l(-\omega)|^2\left|\chi_m(\omega)-\chi_m^*(-\omega)\right|^2\kappa \\ & \left. + \; g^2\gamma\left[|\chi_m(\omega)|^2(\bar{N}+1)+|\chi_m(-\omega)|^2\bar{N}\right]\right]\delta(\omega+\omega')\end{aligned} \tag{C.17}$$

$$\begin{aligned}\left\langle\tilde{a}^{\dagger}(\omega)\tilde{a}(\omega')\right\rangle = |\nu(\omega)|^2|\chi_l(-\omega)|^2\Big[&g^4|\chi_l(\omega)|^2\left|\chi_m(\omega)-\chi_m^*(-\omega)\right|^2\kappa\\ &+g^2\gamma\left[|\chi_m(\omega)|^2(\bar{N}+1)+|\chi_m(-\omega)|^2\bar{N}\right]\Big]\delta(\omega+\omega')\end{aligned} \tag{C.18}$$

$$\begin{aligned}\left\langle\tilde{b}(\omega)\tilde{b}(\omega')\right\rangle &= g^2\gamma|\chi_m(\omega)|^2\chi_m(-\omega)\left[\chi_l^*(\omega)-\chi_l(-\omega)\right](\bar{N}+1)|\nu(\omega)|^2\delta(\omega+\omega')\\ &-g^2\gamma|\chi_m(-\omega)|^2\chi_m(\omega)\left[\chi_l(\omega)-\chi_l^*(-\omega)\right]\bar{N}|\nu(\omega)|^2\delta(\omega+\omega')\\ &-g^2\kappa\chi_m(\omega)\chi_m(-\omega)|\chi_l(\omega)|^2|\nu(\omega)|^2\delta(\omega+\omega')\\ &-g^4\gamma|\chi_m(\omega)|^2|\chi_m(-\omega)|^2\left|\chi_l(\omega)-\chi_l^*(-\omega)\right|^2(2\bar{N}+1)|\nu(\omega)|^2\delta(\omega+\omega')\end{aligned} \tag{C.19}$$

$$\begin{aligned}\left\langle\tilde{b}^{\dagger}(\omega)\tilde{b}^{\dagger}(\omega')\right\rangle &= g^2\gamma|\chi_m(\omega)|^2\chi_m^*(-\omega)\left[\chi_l(\omega)-\chi_l^*(-\omega)\right](\bar{N}+1)|\nu(\omega)|^2\delta(\omega+\omega')\\ &-g^2\gamma|\chi_m(-\omega)|^2\chi_m^*(\omega)\left[\chi_l^*(\omega)-\chi_l(-\omega)\right]\bar{N}|\nu(\omega)|^2\delta(\omega+\omega')\\ &-g^2\kappa\chi_m^*(\omega)\chi_m^*(-\omega)|\chi_l(\omega)|^2|\nu(\omega)|^2\delta(\omega+\omega')\\ &-g^4\gamma|\chi_m(\omega)|^2|\chi_m(-\omega)|^2\left|\chi_l(\omega)-\chi_l^*(-\omega)\right|^2(2\bar{N}+1)|\nu(\omega)|^2\delta(\omega+\omega')\end{aligned} \tag{C.20}$$

$$\begin{aligned}\left\langle\tilde{b}(\omega)\tilde{b}^{\dagger}(\omega')\right\rangle &= \gamma|\chi_m(\omega)|^2(\bar{N}+1)|\nu(\omega)|^2\delta(\omega+\omega')\\ &-g^2\gamma|\chi_m(\omega)|^2\chi_m(-\omega)\left[\chi_l^*(\omega)-\chi_l(-\omega)\right](\bar{N}+1)|\nu(\omega)|^2\delta(\omega+\omega')\\ &-g^2\gamma|\chi_m(\omega)|^2\chi_m^*(-\omega)\left[\chi_l(\omega)-\chi_l^*(-\omega)\right](\bar{N}+1)|\nu(\omega)|^2\delta(\omega+\omega')\\ &+g^2\kappa|\chi_m(\omega)|^2|\chi_l(\omega)|^2|\nu(\omega)|^2\delta(\omega+\omega')\\ &+g^4\gamma|\chi_m(\omega)|^2|\chi_m(-\omega)|^2\left|\chi_l(\omega)-\chi_l^*(-\omega)\right|^2(2\bar{N}+1)|\nu(\omega)|^2\delta(\omega+\omega')\end{aligned} \tag{C.21}$$

$$\begin{aligned}\left\langle\tilde{b}^\dagger(\omega)\tilde{b}(\omega')\right\rangle = {} & \gamma|\chi_m(-\omega)|^2\bar{N}|\nu(\omega)|^2\delta(\omega+\omega') \\ & + g^2\gamma\chi_m^*(\omega)|\chi_m(-\omega)|^2\left[\chi_l^*(\omega)-\chi_l(-\omega)\right]\bar{N}|\nu(\omega)|^2\delta(\omega+\omega') \\ & + g^2\gamma\chi_m(\omega)|\chi_m(-\omega)|^2\left[\chi_l(\omega)-\chi_l^*(-\omega)\right]\bar{N}|\nu(\omega)|^2\delta(\omega+\omega') \\ & + g^2\kappa|\chi_m(-\omega)|^2|\chi_l(\omega)|^2|\nu(\omega)|^2\delta(\omega+\omega') \\ & + g^4\gamma|\chi_m(\omega)|^2|\chi_m(-\omega)|^2\left|\chi_l(\omega)-\chi_l^*(-\omega)\right|^2(2\bar{N}+1)|\nu(\omega)|^2\delta(\omega+\omega')\end{aligned} \tag{C.22}$$

$$\left\langle\tilde{x}(\omega)\tilde{x}(\omega')\right\rangle = x_{zpf}^2\left(\left\langle\tilde{b}(\omega)\tilde{b}(\omega')\right\rangle+\left\langle\tilde{b}(\omega)\tilde{b}^\dagger(\omega')\right\rangle+\left\langle\tilde{b}^\dagger(\omega)\tilde{b}(\omega')\right\rangle+\left\langle\tilde{b}^\dagger(\omega)\tilde{b}^\dagger(\omega')\right\rangle\right) \tag{C.23}$$

$$\begin{aligned}& = x_{zpf}^2\delta(\omega+\omega')|\nu(\omega)|^2\left[\gamma|\chi_m(\omega)|^2(\bar{N}+1)+\gamma|\chi_m(-\omega)|^2\bar{N}\right. \\ & \left.+g^2\kappa|\chi_m(\omega)-\chi_m^*(-\omega)|^2|\chi_l(\omega)|^2\right]\end{aligned} \tag{C.24}$$

If we then consider we are detecting the light from the output mode of the cavity then we need to look at the correlators

$$\left\langle\tilde{a}_{\text{sig}}(\omega)\tilde{a}_{\text{sig}}^\dagger(\omega')\right\rangle = \kappa_1\left\langle\tilde{a}(\omega)\tilde{a}^\dagger(\omega')\right\rangle-\sqrt{\kappa_1}\left\langle\tilde{a}_{\text{In},1}(\omega)\tilde{a}^\dagger(\omega')\right\rangle-\sqrt{\kappa_1}\left\langle\tilde{a}(\omega)\tilde{a}_{\text{In},1}^\dagger(\omega')\right\rangle+\left\langle\tilde{a}_{\text{In},1}(\omega)\tilde{a}_{\text{In},1}^\dagger(\omega')\right\rangle \tag{C.25}$$

$$\begin{aligned}& = \delta(\omega+\omega')\left\{|\kappa_1\chi_l(\omega)\nu(\omega)-1|^2+\kappa_1\kappa_2|\chi_l(\omega)|^2|\nu(\omega)|^2\right. \\ & - g^2\kappa_1(\kappa_1+\kappa_2)|\nu(\omega)|^2|\chi_l(\omega)|^2\chi_l^*(-\omega)\left[\chi_m(\omega)-\chi_m^*(-\omega)\right] \\ & - g^2\kappa_1(\kappa_1+\kappa_2)|\nu(\omega)|^2|\chi_l(\omega)|^2\chi_l(-\omega)\left[\chi_m^*(\omega)-\chi_m(-\omega)\right] \\ & + g^2\kappa_1\nu(\omega)\chi_l(\omega)\chi_l^*(-\omega)\left(\chi_m(\omega)-\chi_m^*(-\omega)\right) \\ & + g^2\kappa_1\nu^*(\omega)\chi_l^*(\omega)\chi_l(-\omega)\left(\chi_m^*(\omega)-\chi_m(-\omega)\right) \\ & + g^2\kappa_1\gamma|\nu(\omega)|^2|\chi_l(\omega)|^2\left[|\chi_m(\omega)|^2(\bar{N}+1)+|\chi_m(-\omega)|^2\bar{N}\right] \\ & \left.+g^4\kappa_1(\kappa_1+\kappa_2)|\nu(\omega)|^2|\chi_l(\omega)|^2|\chi_l(-\omega)|^2\left|\chi_m(\omega)-\chi_m^*(-\omega)\right|^2\right\}\end{aligned} \tag{C.26}$$

$$\left\langle \tilde{a}^{\dagger}_{\mathrm{sig}}(\omega)\tilde{a}_{\mathrm{sig}}(\omega')\right\rangle = \kappa_1 \left\langle \tilde{a}^{\dagger}(\omega)\tilde{a}(\omega')\right\rangle - \sqrt{\kappa_1}\cancelto{0}{\left\langle \tilde{a}^{\dagger}_{\mathrm{In},1}(\omega)\tilde{a}(\omega')\right\rangle} - \sqrt{\kappa_1}\cancelto{0}{\left\langle \tilde{a}^{\dagger}(\omega)\tilde{a}_{\mathrm{In},1}(\omega')\right\rangle} + \cancelto{0}{\left\langle \tilde{a}^{\dagger}_{\mathrm{In},1}(\omega)\tilde{a}_{\mathrm{In},1}(\omega')\right\rangle} \tag{C.27}$$

$$\begin{aligned} &= \delta(\omega+\omega')\left\{ g^2\kappa_1\gamma|\nu(\omega)|^2|\chi_l(-\omega)|^2\left[|\chi_m(\omega)|^2(\bar{N}+1) + |\chi_m(-\omega)|^2\bar{N}\right]\right. \\ &\left. + \ g^4\kappa_1(\kappa_1+\kappa_2)|\nu(\omega)|^2|\chi_l(-\omega)|^2|\chi_l(\omega)|^2\left|\chi_m(\omega) - \chi^*_m(-\omega)\right|^2\right\} \end{aligned} \tag{C.28}$$

$$\left\langle \tilde{a}_{\mathrm{sig}}(\omega)\tilde{a}_{\mathrm{sig}}(\omega')\right\rangle = \kappa_1 \left\langle \tilde{a}(\omega)\tilde{a}(\omega')\right\rangle - \sqrt{\kappa_1}\left\langle \tilde{a}_{\mathrm{In},1}(\omega)\tilde{a}(\omega')\right\rangle - \sqrt{\kappa_1}\cancelto{0}{\left\langle \tilde{a}(\omega)\tilde{a}_{\mathrm{In},1}(\omega')\right\rangle} + \cancelto{0}{\left\langle \tilde{a}_{\mathrm{In},1}(\omega)\tilde{a}_{\mathrm{In},1}(\omega')\right\rangle} \tag{C.29}$$

$$\begin{aligned} &= \delta(\omega+\omega')\left\{ g^2\kappa_1(\kappa_1+\kappa_2)|\nu(\omega)|^2|\chi_l(\omega)|^2\chi_l(-\omega)\left[\chi^*_m(\omega) - \chi_m(-\omega)\right]\right. \\ &+ g^2\kappa_1\nu^*(\omega)\chi^*_l(\omega)\chi_l(-\omega)\left[\chi^*_m(\omega) - \chi_m(-\omega)\right] \\ &- g^2\kappa_1\gamma|\nu(\omega)|^2\chi^*_l(\omega)\chi^*_l(-\omega)\left[|\chi_m(\omega)|^2(\bar{N}+1) + |\chi_m(-\omega)|^2\bar{N}\right] \\ &\left. - \ g^4\kappa_1(\kappa_1+\kappa_2)|\nu(\omega)|^2|\chi_l(\omega)|^2|\chi_l(-\omega)|^2\left|\chi_m(\omega) - \chi^*_m(-\omega)\right|^2\right\} \end{aligned} \tag{C.30}$$

$$\left\langle \tilde{a}^{\dagger}_{\mathrm{sig}}(\omega)\tilde{a}^{\dagger}_{\mathrm{sig}}(\omega')\right\rangle = \kappa_1 \left\langle \tilde{a}^{\dagger}(\omega)\tilde{a}^{\dagger}(\omega')\right\rangle - \sqrt{\kappa_1}\cancelto{0}{\left\langle \tilde{a}^{\dagger}_{\mathrm{In},1}(\omega)\tilde{a}^{\dagger}(\omega')\right\rangle} - \sqrt{\kappa_1}\left\langle \tilde{a}^{\dagger}(\omega)\tilde{a}^{\dagger}_{\mathrm{In},1}(\omega')\right\rangle + \cancelto{0}{\left\langle \tilde{a}^{\dagger}_{\mathrm{In},1}(\omega)\tilde{a}^{\dagger}_{\mathrm{In},1}(\omega')\right\rangle} \tag{C.31}$$

$$\begin{aligned} &= \delta(\omega+\omega')\left\{ g^2\kappa_1(\kappa_1+\kappa_2)|\nu(\omega)|^2|\chi_l(\omega)|^2\chi^*_l(-\omega)\left[\chi_m(\omega) - \chi^*_m(-\omega)\right]\right. \\ &+ g^2\kappa_1\nu(\omega)\chi_l(\omega)\chi^*_l(-\omega)\left[\chi_m(\omega) - \chi^*_m(-\omega)\right] \\ &- g^2\kappa_1\gamma|\nu(\omega)|^2\chi_l(\omega)\chi_l(-\omega)\left[|\chi_m(\omega)|^2(\bar{N}+1) + |\chi_m(-\omega)|^2\bar{N}\right] \\ &\left. - \ g^4\kappa_1(\kappa_1+\kappa_2)|\nu(\omega)|^2|\chi_l(\omega)|^2|\chi_l(-\omega)|^2\left|\chi_m(\omega) - \chi^*_m(-\omega)\right|^2\right\} \end{aligned} \tag{C.32}$$

Since all of our correlators include a $\delta(\omega+\omega')$ term, we can express our PSD as

$$
\begin{aligned}
S_{\Delta i \Delta i}(\omega) &= \lim_{\tau\to\infty} \frac{1}{\tau} \left\langle \left| \int_{-\tau/2}^{\tau/2} dt e^{i\omega t} \Delta i(t) \right|^2 \right\rangle && \text{(C.33)} \\
&= \lim_{\tau\to\infty} \frac{1}{\tau} \int_{-\tau/2}^{\tau/2} \int_{-\tau/2}^{\tau/2} dt dt' e^{i\omega(t-t')} \left\langle \Delta i(t) \Delta i(t') \right\rangle && \text{(C.34)} \\
&\propto \lim_{\tau\to\infty} \frac{1}{\tau} \int_{-\frac{\tau}{2}}^{\frac{\tau}{2}} \int_{-\frac{\tau}{2}}^{\frac{\tau}{2}} dt dt' \Big[\left\langle \hat{a}_{\mathrm{sig}}(t) \hat{a}^{\dagger}_{\mathrm{sig}}(t') \right\rangle e^{i(\omega+\Delta_{\mathrm{LO}})(t-t')} + \left\langle \hat{a}^{\dagger}_{\mathrm{sig}}(t) \hat{a}_{\mathrm{sig}}(t') \right\rangle e^{i(\omega-\Delta_{\mathrm{LO}})(t-t')} \\
&- \left\langle \hat{a}_{\mathrm{sig}}(t) \hat{a}_{\mathrm{sig}}(t') \right\rangle e^{i(\omega+\Delta_{\mathrm{LO}})t} e^{-i(\omega-\Delta_{\mathrm{LO}})t'} e^{2i\theta} - \left\langle \hat{a}^{\dagger}_{\mathrm{sig}}(t) \hat{a}^{\dagger}_{\mathrm{sig}}(t') \right\rangle e^{i(\omega-\Delta_{\mathrm{LO}})t} e^{-i(\omega+\Delta_{\mathrm{LO}})t'} e^{-2i\theta} \Big] \\
& && \text{(C.35)} \\
&= \lim_{\tau\to\infty} \frac{\tau}{2\pi} \int \int d\omega' d\omega'' \Big[\left\langle \hat{a}_{\mathrm{sig}}(\omega') \hat{a}^{\dagger}_{\mathrm{sig}}(\omega'') \right\rangle \mathrm{sinc}^2 \left[(\omega - \omega' + \Delta_{\mathrm{LO}}) \frac{\tau}{2} \right] \\
&+ \left\langle \hat{a}^{\dagger}_{\mathrm{sig}}(\omega') \hat{a}_{\mathrm{sig}}(\omega'') \right\rangle \mathrm{sinc}^2 \left[(\omega - \omega' - \Delta_{\mathrm{LO}}) \frac{\tau}{2} \right] \\
&- e^{2i\theta} \left\langle \hat{a}_{\mathrm{sig}}(\omega') \hat{a}_{\mathrm{sig}}(\omega'') \right\rangle \mathrm{sinc} \left[(\omega - \omega' + \Delta_{\mathrm{LO}}) \frac{\tau}{2} \right] \mathrm{sinc} \left[(\omega - \omega' - \Delta_{\mathrm{LO}}) \frac{\tau}{2} \right] \\
&- e^{-2i\theta} \left\langle \hat{a}^{\dagger}_{\mathrm{sig}}(\omega') \hat{a}^{\dagger}_{\mathrm{sig}}(\omega'') \right\rangle \mathrm{sinc} \left[(\omega - \omega' + \Delta_{\mathrm{LO}}) \frac{\tau}{2} \right] \mathrm{sinc} \left[(\omega - \omega' - \Delta_{\mathrm{LO}}) \frac{\tau}{2} \right] \Big] \\
& && \text{(C.36)}
\end{aligned}
$$

Note that $\lim_{\tau\to\infty} \tau \mathrm{sinc}^2(x\tau) = \pi\delta(x)$ so we can simplify the first two terms. We will then consider two cases, homodyne where $\Delta_{\mathrm{LO}} = 0$ and a heterodyne of sufficient length τ such that the overlap of the sinc functions in the last two terms is 0. In the homodyne case we have

$$
\begin{aligned}
S_{\Delta i \Delta i}(\omega) &= \int d\omega' \Big[\left\langle \hat{a}_{\mathrm{sig}}(\omega) \hat{a}^{\dagger}_{\mathrm{sig}}(\omega') \right\rangle + \left\langle \hat{a}^{\dagger}_{\mathrm{sig}}(\omega) \hat{a}_{\mathrm{sig}}(\omega') \right\rangle \\
&- e^{2i\theta} \left\langle \hat{a}_{\mathrm{sig}}(\omega) \hat{a}_{\mathrm{sig}}(\omega') \right\rangle - e^{-2i\theta} \left\langle \hat{a}^{\dagger}_{\mathrm{sig}}(\omega) \hat{a}^{\dagger}_{\mathrm{sig}}(\omega') \right\rangle \Big] && \text{(C.37)} \\
&= |\kappa_1 \chi_l(\omega) \nu(\omega) - 1|^2 + \kappa_1 \kappa_2 |\chi_l(\omega)|^2 |\nu(\omega)|^2 \\
&- 4\cos\theta g^2 \kappa_1 (\kappa_1 + \kappa_2) |\nu(\omega)|^2 |\chi_l(\omega)|^2 \mathrm{Re} \left\{ e^{-i\theta} \chi_l^*(-\omega) \left[\chi_m(\omega) - \chi_m^*(-\omega) \right] \right\} \\
&+ 4\sin\theta g^2 \kappa_1 \mathrm{Re} \left\{ e^{-i(\theta-\pi/2)} \nu(\omega) \chi_l(\omega) \chi_l^*(-\omega) \left(\chi_m(\omega) - \chi_m^*(-\omega) \right) \right\} \\
&+ g^2 \kappa_1 \gamma |\nu(\omega)|^2 |\chi_l(\omega) e^{-i\theta} + \chi_l^*(-\omega) e^{i\theta}|^2 \left[|\chi_m(\omega)|^2 (\bar{N} + 1) + |\chi_m(-\omega)|^2 \bar{N} \right] \\
&+ 4\cos^2\theta g^4 \kappa_1 (\kappa_1 + \kappa_2) |\nu(\omega)|^2 |\chi_l(\omega)|^2 |\chi_l(-\omega)|^2 \left| \chi_m(\omega) - \chi_m^*(-\omega) \right|^2 \\
& && \text{(C.38)}
\end{aligned}
$$

In the heterodyne case we have

$$S_{\Delta i\Delta i}(\omega) = \int d\omega' \left\langle \hat{a}_{\mathrm{sig}}(\omega+\Delta_{\mathrm{LO}})\hat{a}^{\dagger}_{\mathrm{sig}}(\omega')\right\rangle + \left\langle \hat{a}^{\dagger}_{\mathrm{sig}}(\omega-\Delta_{\mathrm{LO}})\hat{a}_{\mathrm{sig}}(\omega')\right\rangle \tag{C.39}$$

$$\begin{aligned}
&= |\kappa_1\chi_l(\omega+\Delta_{\mathrm{LO}})\nu(\omega+\Delta_{\mathrm{LO}})-1|^2 + \kappa_1\kappa_2|\chi_l(\omega+\Delta_{\mathrm{LO}})|^2|\nu(\omega+\Delta_{\mathrm{LO}})|^2 \\
&- 2g^2\kappa_1(\kappa_1+\kappa_2)|\nu(\omega+\Delta_{\mathrm{LO}})|^2|\chi_l(\omega+\Delta_{\mathrm{LO}})|^2\mathrm{Re}\left\{\chi_l^*(-(\omega+\Delta_{\mathrm{LO}}))\left[\chi_m(\omega+\Delta_{\mathrm{LO}})-\chi_m^*(-(\omega+\Delta_{\mathrm{LO}}))\right]\right\} \\
&+ 2g^2\kappa_1\mathrm{Re}\left\{\nu(\omega+\Delta_{\mathrm{LO}})\chi_l(\omega+\Delta_{\mathrm{LO}})\chi_l^*(-(\omega+\Delta_{\mathrm{LO}}))\left(\chi_m(\omega+\Delta_{\mathrm{LO}})-\chi_m^*(-(\omega+\Delta_{\mathrm{LO}}))\right)\right\} \\
&+ g^2\kappa_1\gamma|\nu(\omega+\Delta_{\mathrm{LO}})|^2|\chi_l(\omega+\Delta_{\mathrm{LO}})|^2\left[|\chi_m(\omega+\Delta_{\mathrm{LO}})|^2(\bar{N}+1)+|\chi_m(-(\omega+\Delta_{\mathrm{LO}}))|^2\bar{N}\right] \\
&+ g^2\kappa_1\gamma|\nu(\omega-\Delta_{\mathrm{LO}})|^2|\chi_l(-(\omega-\Delta_{\mathrm{LO}}))|^2\left[|\chi_m(\omega-\Delta_{\mathrm{LO}})|^2(\bar{N}+1)+|\chi_m(-(\omega-\Delta_{\mathrm{LO}}))|^2\bar{N}\right] \\
&+ g^4\kappa_1(\kappa_1+\kappa_2)|\nu(\omega+\Delta_{\mathrm{LO}})|^2|\chi_l(\omega+\Delta_{\mathrm{LO}})|^2|\chi_l(-(\omega+\Delta_{\mathrm{LO}}))|^2\left|\chi_m(\omega+\Delta_{\mathrm{LO}})-\chi_m^*(-(\omega+\Delta_{\mathrm{LO}}))\right|^2 \\
&+ g^4\kappa_1(\kappa_1+\kappa_2)|\nu(\omega-\Delta_{\mathrm{LO}})|^2|\chi_l(-(\omega-\Delta_{\mathrm{LO}}))|^2|\chi_l(\omega-\Delta_{\mathrm{LO}})|^2\left|\chi_m(\omega-\Delta_{\mathrm{LO}})-\chi_m^*(-(\omega-\Delta_{\mathrm{LO}}))\right|^2
\end{aligned} \tag{C.40}$$

Bibliography

[1] E. M. Purcell. Spontaneous emission probabilities at radio frequencies. *Phys. Rev.*, 69:681, Jun 1946. doi:10.1103/PhysRev.69.674.2.

[2] A. Frisk Kockum, A. Miranowicz, S. De Liberato, S. Savasta, and F. Nori. Ultrastrong coupling between light and matter. *Nature Reviews Physics*, 1(1):19–40, Jan 2019. doi:10.1038/s42254-018-0006-2.

[3] A. Bayer, M. Pozimski, S. Schambeck, D. Schuh, R. Huber, D. Bougeard, and C. Lange. Terahertz light–matter interaction beyond unity coupling strength. *Nano Letters*, 17(10):6340–6344, Oct 2017. doi:10.1021/acs.nanolett.7b03103.

[4] G. Günter, A. A. Anappara, J. Hees, A. Sell, G. Biasiol, L. Sorba, S. De Liberato, C. Ciuti, A. Tredicucci, A. Leitenstorfer, and R. Huber. Sub-cycle switch-on of ultrastrong light–matter interaction. *Nature*, 458(7235):178–181, Mar 2009. doi:10.1038/nature07838.

[5] F. Yoshihara, T. Fuse, S. Ashhab, K. Kakuyanagi, S. Saito, and K. Semba. Superconducting qubit–oscillator circuit beyond the ultrastrong-coupling regime. *Nature Physics*, 13(1):44–47, Jan 2017. doi:10.1038/nphys3906.

[6] S. Gambino, M. Mazzeo, A. Genco, O. Di Stefano, S. Savasta, S. Patanè, D. Ballarini, F. Mangione, G. Lerario, D. Sanvitto, and G. Gigli. Exploring light–matter interaction phenomena under ultrastrong coupling regime. *ACS Photonics*, 1(10):1042–1048, Oct 2014. doi:10.1021/ph500266d.

[7] F. Benz, M. K. Schmidt, A. Dreismann, R. Chikkaraddy, Y. Zhang, A. Demetriadou, C. Carnegie, H. Ohadi, B. de Nijs, R. Esteban, J. Aizpurua, and J. J. Baumberg. Single-molecule optomechanics in picocavities. *Science*, 354(6313):726–729, 2016. doi:10.1126/science.aah5243.

[8] Y. Kaluzny, P. Goy, M. Gross, J. M. Raimond, and S. Haroche. Observation of self-induced rabi oscillations in two-level atoms excited inside a resonant cavity: The ringing regime of superradiance. *Phys. Rev. Lett.*, 51:1175–1178, Sep 1983. doi:10.1103/PhysRevLett.51.1175.

[9] A. Kuhn, M. Hennrich, and G. Rempe. Deterministic single-photon source for distributed quantum networking. *Phys. Rev. Lett.*, 89:067901, Jul 2002. doi:10.1103/PhysRevLett.89.067901.

[10] E. Hagley, X. Maître, G. Nogues, C. Wunderlich, M. Brune, J. M. Raimond, and S. Haroche. Generation of einstein-podolsky-rosen pairs of atoms. *Phys. Rev. Lett.*, 79:1–5, Jul 1997. doi:10.1103/PhysRevLett.79.1.

[11] X. Maître, E. Hagley, G. Nogues, C. Wunderlich, P. Goy, M. Brune, J. M. Raimond, and S. Haroche. Quantum memory with a single photon in a cavity. *Phys. Rev. Lett.*, 79:769–772, Jul 1997. doi:10.1103/PhysRevLett.79.769.

[12] A. Rauschenbeutel, G. Nogues, S. Osnaghi, P. Bertet, M. Brune, J.-M. Raimond, and S. Haroche. Step-by-step engineered multiparticle entanglement. *Science*, 288(5473):2024–2028, 2000. doi:10.1126/science.288.5473.2024.

[13] J. M. Raimond, M. Brune, and S. Haroche. Manipulating quantum entanglement with atoms and photons in a cavity. *Rev. Mod. Phys.*, 73:565–582, Aug 2001. doi:10.1103/RevModPhys.73.565.

[14] B.-G. Englert and H. Walther. Preparing a ghz state, or an epr state, with the one-atom maser. *Optics Communications*, 179(1):283–288, 2000. doi:10.1016/S0030-4018(99)00728-2.

[15] M. Löffler, B. G. Englert, and H. Walther. Testing a bell-type inequality with a micromaser. *Applied Physics B*, 63(5):511–516, Nov 1996. doi:10.1007/BF01828949.

[16] U. Delić, M. Reisenbauer, D. Grass, N. Kiesel, V. Vuletić, and M. Aspelmeyer. Cavity cooling of a levitated nanosphere by coherent scattering. *Phys. Rev. Lett.*, 122:123602, Mar 2019. doi:10.1103/PhysRevLett.122.123602.

[17] D. Windey, C. Gonzalez-Ballestero, P. Maurer, L. Novotny, O. Romero-Isart, and R. Reimann. Cavity-based 3d cooling of a levitated nanoparticle via coherent scattering. *Phys. Rev. Lett.*, 122:123601, Mar 2019. doi:10.1103/PhysRevLett.122.123601.

[18] V. Vuletić and S. Chu. Laser cooling of atoms, ions, or molecules by coherent scattering. *Phys. Rev. Lett.*, 84:3787–3790, Apr 2000. doi:10.1103/PhysRevLett.84.3787.

[19] D. E. Chang, C. A. Regal, S. B. Papp, D. J. Wilson, J. Ye, O. Painter, H. J. Kimble, and P. Zoller. Cavity opto-mechanics using an optically levitated nanosphere. *Proceedings of the National Academy of Sciences*, 107(3):1005–1010, 2010. doi:10.1073/pnas.0912969107.

[20] O. Romero-Isart, A. C. Pflanzer, F. Blaser, R. Kaltenbaek, N. Kiesel, M. Aspelmeyer, and J. I. Cirac. Large quantum superpositions and interference of massive nanometer-sized objects. *Phys. Rev. Lett.*, 107:020405, Jul 2011. doi:10.1103/PhysRevLett.107.020405.

[21] A. Ashkin. Acceleration and trapping of particles by radiation pressure. *Phys. Rev. Lett.*, 24:156–159, Jan 1970. doi:10.1103/PhysRevLett.24.156.

[22] R. Grimm, M. Weidemüller, and Y. B. Ovchinnikov. Optical dipole traps for neutral atoms. volume 42 of *Advances In Atomic, Molecular, and Optical Physics*, pages 95 – 170. Academic Press, 2000. doi:10.1016/S1049-250X(08)60186-X.

[23] H. Son, J. J. Park, Y.-K. Lu, A. O. Jamison, T. Karman, and W. Ketterle. Control of reactive collisions by quantum interference. *Science*, 375(6584):1006–1010, 2022. doi:10.1126/science.abl7257.

[24] C. J. Bustamante, Y. R. Chemla, S. Liu, and M. D. Wang. Optical tweezers in single-molecule biophysics. *Nature Reviews Methods Primers*, 1(1):25, Mar 2021. doi:10.1038/s43586-021-00021-6.

[25] M. Rossi, D. Mason, J. Chen, Y. Tsaturyan, and A. Schliesser. Measurement-based quantum control of mechanical motion. *Nature*, 563(7729):53–58, Nov 2018. doi:10.1038/s41586-018-0643-8.

[26] Y. Harada and T. Asakura. Radiation forces on a dielectric sphere in the rayleigh scattering regime. *Optics Communications*, 124(5):529 – 541, 1996. doi:10.1016/0030-4018(95)00753-9.

[27] K. Visscher and G. Brakenhoff. Theoretical study of optically induced forces on spherical particles in a single beam trap. i: Rayleight scatterers. *Optik*, 89:174–180, 1992.

[28] N. Davidson, H. Jin Lee, C. S. Adams, M. Kasevich, and S. Chu. Long atomic coherence times in an optical dipole trap. *Phys. Rev. Lett.*, 74:1311–1314, Feb 1995. doi:10.1103/PhysRevLett.74.1311.

[29] H. J. Lee, C. S. Adams, M. Kasevich, and S. Chu. Raman cooling of atoms in an optical dipole trap. *Phys. Rev. Lett.*, 76:2658–2661, Apr 1996. doi:10.1103/PhysRevLett.76.2658.

[30] R. J. Cook and R. K. Hill. An electromagnetic mirror for neutral atoms. *Optics Communications*, 43(4):258 – 260, 1982. doi:10.1016/0030-4018(82)90392-3.

[31] J. P. Dowling and J. Gea-Banacloche. Evanescent light-wave atom mirrors, resonators, waveguides, and traps. volume 37 of *Advances In Atomic, Molecular, and Optical Physics*, pages 1 – 94. Academic Press, 1996. doi:10.1016/S1049-250X(08)60098-1.

[32] T. Müller-Seydlitz, M. Hartl, B. Brezger, H. Hänsel, C. Keller, A. Schnetz, R. J. C. Spreeuw, T. Pfau, and J. Mlynek. Atoms in the lowest motional band of a three-dimensional optical lattice. *Phys. Rev. Lett.*, 78:1038–1041, Feb 1997. doi:10.1103/PhysRevLett.78.1038.

[33] R. Ozeri, L. Khaykovich, and N. Davidson. Long spin relaxation times in a single-beam blue-detuned optical trap. *Phys. Rev. A*, 59:R1750–R1753, Mar 1999. doi:10.1103/PhysRevA.59.R1750.

[34] E. Hebestreit, R. Reimann, M. Frimmer, and L. Novotny. Measuring the internal temperature of a levitated nanoparticle in high vacuum. *Phys. Rev. A*, 97:043803, Apr 2018. doi:10.1103/PhysRevA.97.043803.

[35] T. Weiss, M. Roda-Llordes, E. Torrontegui, M. Aspelmeyer, and O. Romero-Isart. Large quantum delocalization of a levitated nanoparticle using optimal control: Applications for force sensing and entangling via weak forces. *Phys. Rev. Lett.*, 127:023601, Jul 2021. doi:10.1103/PhysRevLett.127.023601.

[36] U. Delić. *Cavity cooling by coherent scattering of a levitated nanosphere in vacuum.* PhD thesis, Universität Wien, 2019.

[37] D. Barredo, V. Lienhard, S. de Léséleuc, T. Lahaye, and A. Browaeys. Synthetic three-dimensional atomic structures assembled atom by atom. *Nature*, 561(7721):79–82, Sep 2018. doi:10.1038/s41586-018-0450-2.

[38] R. Roy, A. Green, R. Bowler, and S. Gupta. Rapid cooling to quantum degeneracy in dynamically shaped atom traps. *Phys. Rev. A*, 93:043403, Apr 2016. doi:10.1103/PhysRevA.93.043403.

[39] F. K. Fatemi, M. Bashkansky, and Z. Dutton. Dynamic high-speed spatial manipulation of cold atoms using acousto-optic and spatial light modulation. *Opt. Express*, 15(6):3589–3596, Mar 2007. doi:10.1364/OE.15.003589.

[40] K. Henderson, C. Ryu, C. MacCormick, and M. G. Boshier. Experimental demonstration of painting arbitrary and dynamic potentials for bose–einstein condensates. *New Journal of Physics*, 11(4):043030, apr 2009. doi:10.1088/1367-2630/11/4/043030.

[41] A. O. Caldeira and A. J. Leggett. Influence of dissipation on quantum tunneling in macroscopic systems. *Phys. Rev. Lett.*, 46:211–214, Jan 1981. doi:10.1103/PhysRevLett.46.211.

[42] C. W. Gardiner and M. J. Collett. Input and output in damped quantum systems: Quantum stochastic differential equations and the master equation. *Phys. Rev. A*, 31:3761–3774, Jun 1985. doi:10.1103/PhysRevA.31.3761.

[43] G. W. Ford, J. T. Lewis, and R. F. O'Connell. Quantum langevin equation. *Phys. Rev. A*, 37:4419–4428, Jun 1988. doi:10.1103/PhysRevA.37.4419.

[44] V. Giovannetti and D. Vitali. Phase-noise measurement in a cavity with a movable mirror undergoing quantum brownian motion. *Phys. Rev. A*, 63:023812, Jan 2001. doi:10.1103/PhysRevA.63.023812.

[45] B. Hauer, J. Maciejko, and J. Davis. Nonlinear power spectral densities for the harmonic oscillator. *Annals of Physics*, 361:148–183, 2015. doi:10.1016/j.aop.2015.05.031.

[46] A. H. Safavi-Naeini, J. Chan, J. T. Hill, S. Gröblacher, H. Miao, Y. Chen, M. Aspelmeyer, and O. Painter. Laser noise in cavity-optomechanical cooling and thermometry. *New Journal of Physics*, 15(3):035007, mar 2013. doi:10.1088/1367-2630/15/3/035007.

[47] W. Bowen and G. Milburn. *Quantum Optomechanics*. CRC Press, 2015. doi:10.1007/978-3-540-28574-8.

[48] A. A. Clerk, M. H. Devoret, S. M. Girvin, F. Marquardt, and R. J. Schoelkopf. Introduction to quantum noise, measurement,

and amplification. *Rev. Mod. Phys.*, 82:1155–1208, Apr 2010. doi:10.1103/RevModPhys.82.1155.

[49] J. F. O'Hanlon. *A User's Guide to Vacuum Technology.* John Wiley & Sons, Ltd, 2003. doi:10.1002/0471467162.

[50] U. Delić, D. Grass, M. Reisenbauer, T. Damm, M. Weitz, N. Kiesel, and M. Aspelmeyer. Levitated cavity optomechanics in high vacuum. *Quantum Science and Technology*, 5(2):025006, mar 2020. doi:10.1088/2058-9565/ab7989.

[51] M. E. Gehm, K. M. O'Hara, T. A. Savard, and J. E. Thomas. Dynamics of noise-induced heating in atom traps. *Phys. Rev. A*, 58:3914–3921, Nov 1998. doi:10.1103/PhysRevA.58.3914.

[52] C. Gonzalez-Ballestero, P. Maurer, D. Windey, L. Novotny, R. Reimann, and O. Romero-Isart. Theory for cavity cooling of levitated nanoparticles via coherent scattering: Master equation approach. *Phys. Rev. A*, 100:013805, Jul 2019. doi:10.1103/PhysRevA.100.013805.

[53] O. Romero-Isart. Quantum superposition of massive objects and collapse models. *Phys. Rev. A*, 84:052121, Nov 2011. doi:10.1103/PhysRevA.84.052121.

[54] C. Wuttke and A. Rauschenbeutel. Thermalization via heat radiation of an individual object thinner than the thermal wavelength. *Phys. Rev. Lett.*, 111:024301, Jul 2013. doi:10.1103/PhysRevLett.111.024301.

[55] C. W. Gardiner and M. J. Collett. Input and output in damped quantum systems: Quantum stochastic differential equations and the master equation. *Phys. Rev. A*, 31:3761–3774, Jun 1985. doi:10.1103/PhysRevA.31.3761.

[56] S. Nimmrichter, K. Hammerer, P. Asenbaum, H. Ritsch, and M. Arndt. Master equation for the motion of a polarizable parti-

cle in a multimode cavity. *New Journal of Physics*, 12(8):083003, aug 2010. doi:10.1088/1367-2630/12/8/083003.

[57] V. Vuletić, H. W. Chan, and A. T. Black. Three-dimensional cavity doppler cooling and cavity sideband cooling by coherent scattering. *Phys. Rev. A*, 64:033405, Aug 2001. doi:10.1103/PhysRevA.64.033405.

[58] M. Hosseini, Y. Duan, K. M. Beck, Y.-T. Chen, and V. Vuletić. Cavity cooling of many atoms. *Phys. Rev. Lett.*, 118:183601, May 2017. doi:10.1103/PhysRevLett.118.183601.

[59] E. Kochkina. *Stigmatic and Astigmatic Gaussian Beams in Fundamental Mode.* PhD thesis, Leibniz University Hannover, 2013. URL `https://s3.cern.ch/inspire-prod-files-f/fd149f5c80b07118f03732f683bd7ee5`.

[60] P. Rabl, C. Genes, K. Hammerer, and M. Aspelmeyer. Phase-noise induced limitations on cooling and coherent evolution in optomechanical systems. *Phys. Rev. A*, 80:063819, Dec 2009. doi:10.1103/PhysRevA.80.063819.

[61] M. Summers, D. Burnham, and D. McGloin. Trapping solid aerosols with optical tweezers: A comparison between gas and liquid phase optical traps. *Optics Express*, 16(11):7739–7747, May 2008. doi:10.1364/OE.16.007739.

[62] A. Khodaee, K. Dare, A. Johnson, U. Delić, and M. Aspelmeyer. Dry launching of silica nanoparticles in vacuum. *AIP Advances*, 12(12):125023, 12 2022. doi:10.1063/5.0124029.

[63] P. Asenbaum, S. Kuhn, S. Nimmrichter, U. Sezer, and M. Arndt. Cavity cooling of free silicon nanoparticles in high vacuum. *Nature Communications*, 4(1):2743, Nov 2013. doi:10.1038/ncomms3743.

[64] D. S. Bykov, P. Mestres, L. Dania, L. Schmöger, and T. E. Northup. Direct loading of nanoparticles under high vacuum into a Paul trap for

levitodynamical experiments. *Applied Physics Letters*, 115(3):034101, 07 2019. doi:10.1063/1.5109645.

[65] M. Nikkhou, Y. Hu, J. A. Sabin, and J. Millen. Direct and clean loading of nanoparticles into optical traps at millibar pressures. *Photonics*, 8(11), 2021. doi:10.3390/photonics8110458.

[66] S. Dutta, J. Lorenz, A. Altaf, D. S. Elliott, and Y. P. Chen. Photoassociation of ultracold lirb* molecules: Observation of high efficiency and unitarity-limited rate saturation. *Phys. Rev. A*, 89:020702, Feb 2014. doi:10.1103/PhysRevA.89.020702.

[67] T. Miya, Y. Terunuma, T. Hosaka, and T. Miyashita. Ultimate low-loss single-mode fibre at 1.55 µm. *Electronics Letters*, 15:106–108(2), February 1979. doi:10.1049/el:19790077.

[68] R. Kitamura, L. Pilon, and M. Jonasz. Optical constants of silica glass from extreme ultraviolet to far infrared at near room temperature. *Appl. Opt.*, 46(33):8118–8133, Nov 2007. doi:10.1364/AO.46.008118.

[69] M. A. Green. Self-consistent optical parameters of intrinsic silicon at 300k including temperature coefficients. *Solar Energy Materials and Solar Cells*, 92(11):1305–1310, 2008. doi:10.1016/j.solmat.2008.06.009.

[70] S. Lindner, P. Juschitz, J. Rieser, Y. Y. Fein, M. Debiossac, M. A. Ciampini, M. Aspelmeyer, and N. Kiesel. Hollow-core fiber loading of nanoparticles into ultra-high vacuum. *Applied Physics Letters*, 124(14):143501, 04 2024, https://pubs.aip.org/aip/apl/article-pdf/doi/10.1063/5.0190658/19862224/143501_1_5.0190658.pdf. doi:10.1063/5.0190658.

[71] S. Lindner, P. Juschitz, J. Rieser, Y. Y. Fein, M. Ciampini, M. Aspelmeyer, and N. Kiesel. Hollow-core fiber loading of nanoparticles into ultra-high vacuum, 2023. doi:10.48550/arXiv.2311.13920.

[72] D. Grass. *Levitated optomechanics in vacuum using hollow core photonic crystal fibers and optical cavities.* PhD thesis, Universität Wien, 2018.

[73] R. J. Glauber. The quantum theory of optical coherence. *Phys. Rev.*, 130:2529–2539, Jun 1963. doi:10.1103/PhysRev.130.2529.

[74] J. Gieseler, B. Deutsch, R. Quidant, and L. Novotny. Subkelvin parametric feedback cooling of a laser-trapped nanoparticle. *Phys. Rev. Lett.*, 109:103603, Sep 2012. doi:10.1103/PhysRevLett.109.103603.

[75] F. Tebbenjohanns, M. Frimmer, and L. Novotny. Optimal position detection of a dipolar scatterer in a focused field. *Phys. Rev. A*, 100:043821, Oct 2019. doi:10.1103/PhysRevA.100.043821.

[76] L. Magrini, P. Rosenzweig, C. Bach, A. Deutschmann-Olek, S. G. Hofer, S. Hong, N. Kiesel, A. Kugi, and M. Aspelmeyer. Real-time optimal quantum control of mechanical motion at room temperature. *Nature*, 595(7867):373–377, Jul 2021. doi:10.1038/s41586-021-03602-3.

[77] F. Tebbenjohanns, M. L. Mattana, M. Rossi, M. Frimmer, and L. Novotny. Quantum control of a nanoparticle optically levitated in cryogenic free space. *Nature*, 595(7867):378–382, Jul 2021. doi:10.1038/s41586-021-03617-w.

[78] U. Delić, M. Reisenbauer, K. Dare, D. Grass, V. Vuletić, N. Kiesel, and M. Aspelmeyer. Cooling of a levitated nanoparticle to the motional quantum ground state. *Science*, 367(6480):892–895, 2020. doi:10.1126/science.aba3993.

[79] K. Dare, J. J. Hansen, I. Coroli, A. Johnson, M. Aspelmeyer, and U. Delić. Linear ultrastrong optomechanical interaction, 2023, 2305.16226.

[80] S. Gröblacher, K. Hammerer, M. R. Vanner, and M. Aspelmeyer. Observation of strong coupling between a micromechanical resonator

and an optical cavity field. *Nature*, 460(7256):724–727, Aug 2009. doi:10.1038/nature08171.

[81] I. Wilson-Rae, N. Nooshi, J. Dobrindt, T. J. Kippenberg, and W. Zwerger. Cavity-assisted backaction cooling of mechanical resonators. *New Journal of Physics*, 10(9):095007, sep 2008. doi:10.1088/1367-2630/10/9/095007.

[82] J. M. Dobrindt, I. Wilson-Rae, and T. J. Kippenberg. Parametric normal-mode splitting in cavity optomechanics. *Phys. Rev. Lett.*, 101:263602, Dec 2008. doi:10.1103/PhysRevLett.101.263602.

[83] C. Gut, K. Winkler, J. Hoelscher-Obermaier, S. G. Hofer, R. M. Nia, N. Walk, A. Steffens, J. Eisert, W. Wieczorek, J. A. Slater, M. Aspelmeyer, and K. Hammerer. Stationary optomechanical entanglement between a mechanical oscillator and its measurement apparatus. *Phys. Rev. Research*, 2:033244, Aug 2020. doi:10.1103/PhysRevResearch.2.033244.

[84] A. A. Anappara, S. De Liberato, A. Tredicucci, C. Ciuti, G. Biasiol, L. Sorba, and F. Beltram. Signatures of the ultrastrong light-matter coupling regime. *Phys. Rev. B*, 79:201303, May 2009. doi:10.1103/PhysRevB.79.201303.

[85] J. Casanova, G. Romero, I. Lizuain, J. J. García-Ripoll, and E. Solano. Deep strong coupling regime of the jaynes-cummings model. *Phys. Rev. Lett.*, 105:263603, Dec 2010. doi:10.1103/PhysRevLett.105.263603.

[86] J. Khurgin. Excitonic radius in the cavity polariton in the regime of very strong coupling. *Solid State Communications*, 117(5):307–310, 2001. doi:10.1016/S0038-1098(00)00469-5.

[87] S. Brodbeck, S. De Liberato, M. Amthor, M. Klaas, M. Kamp, L. Worschech, C. Schneider, and S. Höfling. Experimental verification of the very strong coupling regime in a gaas quan-

tum well microcavity. *Phys. Rev. Lett.*, 119:027401, Jul 2017. doi:10.1103/PhysRevLett.119.027401.

[88] J. George, T. Chervy, A. Shalabney, E. Devaux, H. Hiura, C. Genet, and T. W. Ebbesen. Multiple rabi splittings under ultrastrong vibrational coupling. *Phys. Rev. Lett.*, 117:153601, Oct 2016. doi:10.1103/PhysRevLett.117.153601.

[89] V. Sudhir, M. G. Genoni, J. Lee, and M. S. Kim. Critical behavior in ultrastrong-coupled oscillators. *Phys. Rev. A*, 86:012316, Jul 2012. doi:10.1103/PhysRevA.86.012316.

[90] G. A. Peterson, S. Kotler, F. Lecocq, K. Cicak, X. Y. Jin, R. W. Simmonds, J. Aumentado, and J. D. Teufel. Ultrastrong parametric coupling between a superconducting cavity and a mechanical resonator. *Phys. Rev. Lett.*, 123:247701, Dec 2019. doi:10.1103/PhysRevLett.123.247701.

[91] F. Cosco, J. S. Pedernales, and M. B. Plenio. Enhanced force sensitivity and entanglement in periodically driven optomechanics. *Phys. Rev. A*, 103:L061501, Jun 2021. doi:10.1103/PhysRevA.103.L061501.

[92] T. Ilias, D. Yang, S. F. Huelga, and M. B. Plenio. Criticality-enhanced quantum sensing via continuous measurement. *PRX Quantum*, 3:010354, Mar 2022. doi:10.1103/PRXQuantum.3.010354.

[93] K. Gietka, L. Ruks, and T. Busch. Understanding and Improving Critical Metrology. Quenching Superradiant Light-Matter Systems Beyond the Critical Point. *Quantum*, 6:700, Apr. 2022. doi:10.22331/q-2022-04-27-700.

[94] L. Garbe, O. Abah, S. Felicetti, and R. Puebla. Critical quantum metrology with fully-connected models: from heisenberg to kibble–zurek scaling. *Quantum Science and Technology*, 7(3):035010, may 2022. doi:10.1088/2058-9565/ac6ca5.

[95] L. Garbe, O. Abah, S. Felicetti, and R. Puebla. Exponential time-scaling of estimation precision by reaching a quantum critical point. *Phys. Rev. Res.*, 4:043061, Oct 2022. doi:10.1103/PhysRevResearch.4.043061.

[96] K. Kustura, C. Gonzalez-Ballestero, A. d. l. R. Sommer, N. Meyer, R. Quidant, and O. Romero-Isart. Mechanical squeezing via unstable dynamics in a microcavity. *Phys. Rev. Lett.*, 128:143601, Apr 2022. doi:10.1103/PhysRevLett.128.143601.

[97] N. S. Mueller, Y. Okamura, B. G. M. Vieira, S. Juergensen, H. Lange, E. B. Barros, F. Schulz, and S. Reich. Deep strong light–matter coupling in plasmonic nanoparticle crystals. *Nature*, 583(7818):780–784, Jul 2020. doi:10.1038/s41586-020-2508-1.

[98] S. De Liberato. Light-matter decoupling in the deep strong coupling regime: The breakdown of the purcell effect. *Phys. Rev. Lett.*, 112:016401, Jan 2014. doi:10.1103/PhysRevLett.112.016401.

[99] S. G. Hofer and K. Hammerer. Entanglement-enhanced time-continuous quantum control in optomechanics. *Phys. Rev. A*, 91:033822, Mar 2015. doi:10.1103/PhysRevA.91.033822.

[100] L. Novotny and B. Hecht. *Principles of Nano-Optics*. Cambridge University Press, 2006. doi:10.1017/CBO9780511813535.

List of Figures

List of Tables